Position/Speed Sensor-Less Control of Wind Energy Conversion Systems Based on Rotor-Tied Doubly-Fed Induction Generator Systems

by

Mwana Wa Kalaga Mbukani

Research assignment presented in partial fulfilment of the requirements for the degree of Philosophy Doctor (Electrical) in the Faculty of Engineering at Stellenbosch University

Supervisor: Dr. Nkosinathi Gule

December 2019

Stellenbosch University https://scholar.sun.ac.za

Declaration

By submitting this research assignment electronically, I declare that the entirety of the work contained therein is my own, original work, that I am the sole author thereof (save to the extent explicitly otherwise stated), that reproduction and publication thereof by Stellenbosch University will not infringe any third party rights and that I have not previously in its entirety or in part submitted it for obtaining any qualification.

Date: 2019/08/30

Copyright © 2019 Stellenbosch University
All rights reserved.

Stellenbosch University https://scholar.sun.ac.za

Abstract

The doubly-fed induction generator (DFIG) is amongst the most popular wind turbine generator in South Africa. This is partly due to the fact that its back-to-back power converters are partially rated. More precisely, they are rated at 30% of the generator rated power. A new DFIG topology has been proposed recently. That is the rotor-tied doubly-fed induction generator (RDFIG). In this topology, the rotor side is connected to the grid while the stator side is connected to the power converter. It has been shown that this topology holds the advantage of higher efficiency compared to the standard DFIG topology.

High accuracy in all the measurements is required for the optimum operations of wind energy conversion systems (WECSs). The measurement of the rotor position/speed is amongst the most important measurements when it comes to implement any control system for the WECS. The conventional method of measuring the rotor position/speed is to use an electronic/mechanical sensor (encoder or resolver). This measurement involves the use of long cables and in a harsh environment, this can lead to faulty operations of the WECS.

In this thesis, several slip speed estimators for sensor-less control of RDFIG-based WECSs are developed and implemented. The proposed slip speed estimators are based on the association of different sliding mode observers and the PLL estimator. The association of the PLL estimator improves the estimation performance by reducing the noise created by the sliding control control functions. Also, the proposed PLL estimator helps in avoiding a phase shift of π in super-synchronous operating conditions. In addition, in this thesis, several sliding mode observers were developed in order to improve the estimation performance. The proposed sliding mode observers were satisfactory for all the operating conditions of the RDFIG-based WECSs.

The robustness of the proposed slip speed estimators is validated experimentally under various operating conditions. A 5.5-kW custom-designed grid-connected RDFIG test-bench based on a National Instrument (NI) PXIe-8115 controller is used. The proposed slip speed estimators solve the problem linked to the failure of the electromechanical sensors. The overall sensor-less control strategy provides an alternative to the sensor-based control of the RDFIGs. Also, the proposed sensor-less vector control strategy can be used as a back-up in case the electromechanical sensor fails.

Stellenbosch University https://scholar.sun.ac.za

Opsomming

Die dubbelgevoerde induksiegenerator (DFIG) is een van die gewildste windturbinegenerators in Suid-Afrika. Dit is deels as gevolg van die laer kapasiteit omsetters wat die DFIG benodig. 'n Nuwe DFIG-topologie is onlangs voorgestel: Die rotorgebonde DFIG (RDFIG). In dié topologie word die masjien se rotor aan die netwerk gekoppel en die stator aan laer kapasiteit omsetters. Dit is bewys dat hierdie topologie 'n hoër masjieneffektiwiteit het in vergelyking met die standaard-DFIG.

Hoë akkuraatheid van metings word vereis vir die optimale beheer van windenergie-omsettingstelsels (WECS). Die meting van die rotorposisie en -spoed is van die belangrikste metings wanneer dit kom by die beheerstelsel van 'n WECS. Die konvensionele metode van rotorposisie- en rotorspoedmeting is deur middel van 'n kodeerder. Dié meting behels die gebruik van lang kabels in 'n fel omgewing, wat kan lei tot die foutiewe werking van die stelsel.

In hierdie verhandeling word verskeie glipspoedafskatters vir die sensorlose beheer van 'n RDFIG-gebaseerde WECS ontwikkel en geïmplimenteer. Die voorgestelde glipspoedafskatter is gebaseer op die assosiasie van verskillende glymodus-observeerders en 'n PLL-afskatter. Die assosiasie van die PPL-afskatter verbeter die afskattingprestasie deur die geruis van die glymodusbeheerstelsels te verminder. Die voorgestelde PPL-afskatter help ook om 'n faseskuif van π te vermy tydens super-sinchroonoperasie. In hierdie verhandeling word verskeie glymodusobserveerders ontwikkel om die afskattingsprestasie te verbeter. Die voorgestelde glymode-observeerders presteer bevredigend vir alle toestande van die RDFIC-gebaseerde WECS.

Die kragtigheid van die voorgestelde glipspoedafskatters se geldigheid word onder verskeie toestande eksperimenteel getoets en bewys. 'n 5.5 kW netwerkgekoppelde RDFIG toetsbank gebaseer op 'n National Instrument PXIe-8115-beheerder word gebruik. Die probleem van gefaalde elektromeganiese sensors word deur die voorgestelde glipspoedafskatters opgelos. Die sensorlose beheerstrategie gee ook 'n alternatief vir tradisionele sensor-gebaseerde beheer van die RDFIG's.

Stellenbosch University https://scholar.sun.ac.za

Acknowledgements

I would like to express my sincere gratitude to the following people:

- My supervisor Dr Nkosinathi Gule, for his unwavering guidance, encouragement, and continuous support for all of the technical and personal aspects of my research project.
- The NRF for funding this research project, I am very appreciative.
- My parents, Mr Mbukani Katebwa and Mrs Hemedi Tasumini, and my family members, for their unconditional support throughout my studies, their prayers and advice. God bless you.
- Mr. Ore Olubamiwa, for designing the RDFIG that has been used for experimental tests.
- Mr. Pietro Petzer, Andre Swart, Murry Juman, Kenan Cloetie, J.p Du Plooy and Mr J. Arendse for all the invaluable help and guidance in the laboratory.
- My wife, Miriam Mukonkole, and my two children, Mika Mbukani, and Byeka Mbukani, for their unconditional love and invaluable support towards me. They gave me additional motivation and determination during my PhD studies.

Stellenbosch University https://scholar.sun.ac.za

List of conference proceedings and publications

Some of the results presented in this thesis have been published in the following publications.

International conferences

1. **M. W. Kalaga Mbukani** and N. Gule, "Experimental Implementation of The Stator-Side Control of a Grid-Connected Rotor-Tied DFIG-Based WECS," *in the 2018 International Symposium of Power Electronics, Electrical Drives, Automation and Motion (SPEEDAM)*, Amalfi, Italy, pp. 895–900, 2018.

2. **M. W. Kalaga Mbukani** and N. Gule, "Performance analysis of a PLL-Based sensor-less control of rotor-tied DFIG systems," *in the 9th IEEE International Symposium on Sensor-less Motion Control and Electrical Drives (SLED 2018)*, Helsinki, Finland, pp. 48–53, 2018.

Journal papers

1. **M. W. Kalaga Mbukani** and N. Gule, "Evaluation of an STSMO-based estimator for power control of rotor-tied DFIG systems," *in print IET Electric Power Applications*, vol. PP, no. PP, pp. 1 - 1, 2019.

2. **M. W. Kalaga Mbukani** and N. Gule, "PLL-based Sliding Mode Observer Estimators for Sensor-less Control of Rotor-tied DFIG Systems," *in print IEEE Transactions on Industry Applications*, vol. PP, no. PP, pp. 1 - 1, 2019.

3. **M. W. Kalaga Mbukani** and N. Gule, "Comparison of High-order and Second-order Sliding Mode-observer-based Estimators for Speed Sensor-less Control of Rotor-tied DFIG Systems," *in print IET Power Electronics*, vol. PP, no. PP, pp. 1 - 1, 2019.

Stellenbosch University https://scholar.sun.ac.za

Contents

Declaration i

Abstract ii

Opsomming iii

Acknowledgements iv

List of conference proceedings and publications v

Contents vi

List of Figures ix

List of Tables xiv

Nomenclature xv

1 Introduction 1
- 1.1 Introduction . . . 1
- 1.2 Problem statement . . . 3
- 1.3 Aim and objectives . . . 4
- 1.4 Unique contributions . . . 4
- 1.5 Outline of the thesis . . . 5

2 Review of rotor speed/position estimators for the sensor-less control of DFIG systems 7
- 2.1 Introduction . . . 7
- 2.2 Classification of speed/postion estimation methods . . . 7
- 2.3 Model-based estimation methods . . . 8
- 2.4 Saliency-based estimation methods . . . 19
- 2.5 Other methods . . . 20
- 2.6 Summary . . . 20

3 Background 22
- 3.1 Introduction . . . 22

Stellenbosch University https://scholar.sun.ac.za

3.2 Overview of the RDFIG-based WECS . . . 22
3.3 Wind turbine model . . . 22
3.4 Operation principle of the RDFIG system . . . 24
3.5 Power flow in RDFIG systems . . . 26
3.6 Modelling of the RDFIG . . . 29
3.7 L filter model . . . 37
3.8 DC-link model . . . 38
3.9 RDFIG vector control . . . 40
3.10 Speed/position estimation . . . 41
3.11 Summary . . . 45

4 Sensor-less vector control of the RDIFG-based WECS 46
4.1 Introduction . . . 46
4.2 Proposed sensor-less control strategy . . . 46
4.3 Design of the stator side control strategy . . . 49
4.4 Design of the grid side control strategy . . . 56
4.5 Grid voltage angle calculation . . . 59
4.6 Summary . . . 61

5 Slip speed estimators for sensor-less control of RDFIGs 62
5.1 Introduction . . . 62
5.2 Second order sliding mode observer . . . 62
5.3 Adaptive sliding mode observer . . . 65
5.4 Super-twisting sliding mode observer . . . 69
5.5 High order sliding mode observer . . . 73
5.6 Phase locked loop . . . 75
5.7 Summary . . . 78

6 Experimental results and discussions 79
6.1 Introduction . . . 79
6.2 Experimental set-up . . . 79
6.3 Start-up of the RDFIG system . . . 80
6.4 PLL-based sliding mode observer for the sensor-less control of RDFIG systems . . . 82
6.5 PLL-based adaptive sliding mode observer estimator for the sensor-less control of RDFIG systems . . . 91
6.6 PLL-based super-twisting sliding mode observer estimator for the sensor-less control of RDFIG systems . . . 97
6.7 PLL-based high order sliding observer estimator for sensor-less control of RDFIG systems . . . 105
6.8 Comparative study of the proposed slip speed/angle estimators . 115
6.9 Summary . . . 116

7 Conclusions and recommendations on future works 117

Stellenbosch University https://scholar.sun.ac.za

7.1 Introduction 117
7.2 Conclusions 117
7.3 Recommendations for future works 119

References **120**

Appendices **133**

A Data and Experimental setup **134**
A.1 Experimental setup 134
A.2 Data of the RDFIG 135
A.3 Commercially-modified SEW power converter 136
A.4 Data of the L filter 136
A.5 Back-to-back power converter model 137
A.6 Continuous space vector modulation implementation 139

Stellenbosch University https://scholar.sun.ac.za

List of Figures

1.1 Schematics of DFIG systems. 3

2.1 Classification of position/speed estimation methods. 8
2.2 Illustration of a sliding mode observer. 10
2.3 Classification of SMO-based rotor speed estimation methods. 11
2.4 Schematic of a MRAS-based rotor speed estimation. 14
2.5 Classification of MRAS-based rotor speed/position estimation methods. 14
2.6 Schematic of a PLL-based rotor speed estimation. 18

3.1 Schematic of the RDFIG-based WECS. 23
3.2 Tip-speed ratio(ς) versus power coefficient(C_p). 24
3.3 The DFIGs and RDFIGs operations. 25
3.4 The RDFIG's sub-synchronous power flow scheme. 27
3.5 The RDFIG's synchronous power flow scheme. 28
3.6 The RDFIG's super-synchronous power flow scheme. 28
3.7 RDIFG schematics: 29
3.8 Schematic of the reference frames. 31
3.9 RDFIG equivalent circuit in the synchronous reference frame. . . . 34
3.10 Vector diagram of the rotor current space vector. 35
3.11 Schematic of the single-phase L filter. 38
3.12 Schematic of the per-phase L filter at high frequency. 38
3.13 Schematic of the DC-link. 39
3.14 Schematic of a vector control of RDFIG system. 40
3.15 Schematic of the per-phase grid-connected VSC. 41
3.16 Schematic of the PLL estimator [1]. 45

4.1 Schematic of the proposed sensor-less control strategy. 47
4.2 VOC scheme. 49
4.3 Block diagram of the inner stator current loop. 52
4.4 Mechanical power versus wind speed. 53
4.5 Block diagram of the outer power control loop. 54
4.6 Block diagram of the outer speed loop. 56
4.7 Block diagram of the inner converter current control loop. 57

Stellenbosch University https://scholar.sun.ac.za

4.8 Block diagram of the DC-link voltage control loop. 58
4.9 Phasor diagram of the grid voltage space vector. 59
4.10 Block diagram of the SRF-PLL control loop. 60
4.11 Schematic of the SRF-PLL. 61

5.1 Schematic of the proposed SMO and the PLL estimator. 64
5.2 The diagram of the adaptive sliding mode observer. 66
5.3 The PLL-based STSMO estimator. 71
5.4 Proposed PLL-based HOSMO estimator scheme. 74
5.5 A detailed schematic of the proposed PLL estimator. 76

6.1 An image of the test-bench set-up. 80
6.2 Measurement of the grid voltage and the grid angle 81
6.3 Measurement of the grid-side converter 82
(a) 82
(b) 82
(c) 82
6.4 Experimental results during sub-synchronous operating conditions . . . 84
6.5 Experimental results during sub-synchronous operating conditions . . . 84
6.6 Experimental results during synchronous operating conditions 85
6.7 Experimental results during synchronous operating conditions 85
6.8 Experimental results during change in rotor speed from sub-synchronous to super-synchronous operating conditions 86
6.9 Experimental results during change in rotor speed from super-synchronous to sub-synchronous operating conditions 87
6.10 Experimental results during changes in stator current magnitude 88
6.11 Experimental results during changes in stator current magnitude 89
6.12 Experimental results during change in rotor speed from synchronous to sub-synchronous to synchronous operating conditions with inaccurate stator inductance $1.3L_s$ 89
6.13 Experimental results during change in rotor speed from synchronous to sub-synchronous to synchronous operating conditions with inaccurate stator inductance $1.3L_s$ and stator resistance $1.3R_s$. 90
6.14 Experimental results during change in rotor speed from super-synchronous to sub-synchronous operating conditions. 91
6.15 The performance of the ASMO during sub-synchronous operating conditions. 92
(a) 92
(b) 92
(c) 92
(d) 92
6.16 The performance of the ASMO during super-synchronous operating conditions 93
(a) 93

Stellenbosch University https://scholar.sun.ac.za

(b) . . . 93
(c) . . . 93
(d) . . . 93
6.17 The transient performance of the proposed control strategy during speed transition. . . . 94
(a) . . . 94
(b) . . . 94
6.18 The transient performance during change in speed with inaccurate machine parameters ($1.3L_s$ and $1.3R_s$) . . . 94
(a) . . . 94
(b) . . . 94
6.19 The transient performance during change in stator current magnitude 95
(a) . . . 95
(b) . . . 95
(c) . . . 95
(d) . . . 95
6.20 The performance during change from super-synchronous to sub-synchronous operating conditions . . . 96
(a) . . . 96
(b) . . . 96
(c) . . . 96
6.21 Experimental results during sub-synchronous operating conditions (ω_r =-248.8 rad/s) . . . 98
6.22 Experimental results during sub-synchronous operating conditions (ω_r =-248.8 rad/s) . . . 98
6.23 Experimental results during super-synchronous operating conditions (ω_r =-345.4 rad/s) . . . 99
6.24 Experimental results during super-synchronous operating conditions (ω_r =-345.4 rad/s) . . . 99
6.25 Experimental results during variation in rotor speed from super-synchronous synchronous to sub-synchronous operating conditions (from -350 rad/s to -219.8 rad/s) . . . 100
6.26 Experimental results during variation in rotor speed from sub-synchronous synchronous to super-synchronous operating conditions (from -219.8 rad/s to -350 rad/s) . . . 101
6.27 Experimental results during changes in the stator current magnitude from 1.7 A to 4.1 A to -1.7 A (with the rotor rotating at -1214 rpm) . . . 102
6.28 Experimental results during a change in rotor speed with inaccurate stator inductance $1.3L_s$ . . . 103
(a) . . . 103
(b) . . . 103
6.29 The experimental results during change in rotor speed with inaccurate stator inductance at $1.3L_s$ and inaccurate stator resistance $1.3R_s$ . . . 103
(a) . . . 103

Stellenbosch University https://scholar.sun.ac.za

(b) . . . 103
6.30 The transient performance during change in speed from super-synchronous to sub-synchronous operating conditions . . . 104
(a) . . . 104
(b) . . . 104
6.31 The transient performance of the overall control strategy recorded during change in the active rotor power output . . . 105
6.32 The transient performance of the PLL-based HOSMO estimator . . . 106
(a) . . . 106
(b) . . . 106
(c) . . . 106
(d) . . . 106
6.33 The steady-state performance of the PLL-based SMO estimator during super-synchronous operating conditions . . . 107
(a) . . . 107
(b) . . . 107
(c) . . . 107
(d) . . . 107
6.34 Experimmental Illustration of the estimated and actual slip angle estimated using the PLL-based HOSMO estimator during sub-synchronous operating conditions . . . 108
6.35 Experimental Illustration of the estimated and actual slip angle estimated using the PLL-based HOSMO estimator during super-synchronous operating conditions . . . 108
6.36 Experimental performance the PLL-based SMO observer during change in stator current magnitude from 1.5 A to 4.2 A to 1.5 A . . . 109
(a) . . . 109
(b) . . . 109
(c) . . . 109
6.37 Experimental performance of the PLL-based HOSMO observer during change in stator current magnitude from 1.5 A to 4.2 A to 1.5 A . . . 111
(a) . . . 111
(b) . . . 111
(c) . . . 111
6.38 Experimental performance of the PLL-based SMO estimator during change in speed . . . 112
(a) . . . 112
(b) . . . 112
6.39 Experimental performance of the PLL-based HOSMO estimator during change in speed . . . 112
(a) . . . 112
(b) . . . 112

Stellenbosch University https://scholar.sun.ac.za

6.40 The transient performance of the proposed sensor-less control strategy based on PLL-based HOSMO estimator during change in speed from sub-synchronous to super-synchronous operating conditions 113
(a) 113
(b) 113
6.41 The transient performance of the proposed sensor-less control strategy based on PLL-based HOSMO estimator during change in speed from sub-synchronous to super-synchronous operating conditions 113
(a) 113
(b) 113
6.42 The transient performance of the sensor-less control strategy during change in speed from super-synchronous operating conditions to sub-synchronous operating conditions 114
(a) 114
(b) 114
(c) 114

A.1 Laboratory setup. 135
A.2 Built Filter 137
A.3 Power circuit of a VSC 137
A.4 Space vector schemes for SVPWM. 140
A.5 Symmetrical SVPWM waveforms. 142

Stellenbosch University https://scholar.sun.ac.za

List of Tables

3.1 Generated Power and electromagnetic torque signs 27

6.1 Comparative performance of the proposed slip speed estimators . . 115

A.1 Nominal values of the RDFIG 135
A.2 Nominal values of the RDFIG 136
A.3 Nominal inputs of the SEW power converter 136
A.4 Nominal outputs of the SEW power converter 136
A.5 Nominal outputs of the SEW power converter 136
A.6 Switching states 138
A.7 predefined converter voltage space vectors based on the switching states 139
A.8 Swiching segments according to each sector. 141

Stellenbosch University https://scholar.sun.ac.za

Nomenclature

Acronyms

2S	Two-stage
3S	Three-stage
AC	Alternative current
ASMO	Adaptive sliding mode observer
BDFIG	Brush-less doubly-fed induction generator
DC	Direct current
DFIG	Doubly-fed induction generator
DFIM	Doubly-fed induction machine
DVC	Direct voltage control
EKF	Extended Kalman filter
EMF	Electromotive force
FOC	Field-oriented control
FPGA	Field programmable gate array
GSC	Grid-side converter
GTO	Gate turn-off thyristor
HOSMO	High-order sliding mode observer
IGBT	Insulated-gate bipolar transistor
IG	Induction generator
IM	Induction machine
LPF	Low pass filter
MOSFET	Metal-oxide semiconductor field effect transistor
MPPT	Maximum power point tracking
MRAS	Model reference adaptive system
NI	National Instrument
PCC	Point of common coupling
PLL	Phase locked loop
PMSM	Permanent Magnet synchronous machine
RSC	Rotor-side converter

Stellenbosch University https://scholar.sun.ac.za

SRF-PLL	Synchronous reference frame phase locked loop
SG	Synchronous generator
SMO	Sliding mode observer
STSMO	Super-twisting sliding mode observer
STA	Super-twisting algorithm
SSC	Stator side converter
SV-PWM	Space vector pulse width modulation
THD	Total harmonic distortion
VI	Virtual instrument
VOC	Voltage-oriented control
VSC	Voltage-source converter
WECS	Wind energy conversion system

Symbols

v	Voltage	[V]
e	Back-EMF	[V]
i	Current	[A]
λ	Flux linkage	[V/s]
P	Active power	[W]
Q	Reactive power	[Var]
R	Resistance	[Ohms]
L	Inductance	[H]
θ	Position/angle	[rad]
V_{dc}	DC-link voltage	[V]
V_{wind}	Wind speed	[m/s]
V_{tip}	Turbine blades tip speed	[m/s]
r	Turbine propeller radius	[m]
ρ_{air}	Air density	[Kg/m^3]
τ_{em}	Electromagnetic torque	[Nm]
τ_m	Mechanical torque	[Nm]
ω_g	Grid angular speed	[rad/s]
ω_r	Rotor angular speed	[rad/s]
Ω_m	Mechanical angular speed	[rad/s]
Ω_t	Angular speed of the turbine blades	[rad/s]
ω_s	Slip angular speed	[rad/s]
T_s	Sampling period	[s]
f_s	Sampling frequency	[Hz]

Stellenbosch University https://scholar.sun.ac.za

t	Time	[s]
p	Laplace operator	
V	Lyapunov function	
x	State variable	
ς	Tip speed ratio	
s	Slip	
$C_p(\varsigma, \beta)$	Power coefficient	

Subscripts

d	Real axis of the synchronous $dq0$-reference frame
g	Grid
m	Magnetising
q	Imaginary axis of the synchronous $dq0$-reference frame
r	With reference to the rotor
s	With reference to the stator
σ	Leakage
α	Real axis of the stationary $\alpha\beta0$-reference frame
β	Imaginary axis of the stationary $\alpha\beta0$-reference frame

Superscripts

s	With reference to the synchronous reference frame
sl	With reference to the slip reference frame
$\bar{}$	Conjugate value
$\tilde{}$	Error value
$\vec{}$	Vector value
$\hat{}$	Estimated value

Stellenbosch University https://scholar.sun.ac.za

Chapter 1

Introduction

1.1 Introduction

In the last few decades, there has been a considerable growth and interest in wind energy generation worldwide. The doubly-fed induction generator (DFIG) is the most popular wind turbine generator in wind energy conversion systems (WECSs) partly due to its use of the back-to-back converters which is rated at 30 % of the generator power [2–4]. In order to improve the reliability of DFIG-based WECSs, intensive research has been conducted on encoder-less control of the DFIG systems in the literature [5]. Basically, there are two types of the sensor-less control strategies for the conventional DFIG systems. These are the saliency-based estimation methods and the model-based estimation methods. The saliency-based estimation methods are mainly based on signal injection as presented in [6–8]. However, this technique is susceptible to being sensitive to the grid impedance.

The model-based estimation methods for the conventional DFIG systems make use of several observers such as; the model-based reference adaptive system (MRAS), flux observers, extended Kalman filters (EKF), disturbance observers and sliding mode observers (SMOs) [9–14].

SMOs-based rotor speed/angle estimation techniques for the sensor-less control of DFIG systems are discussed in [15–18]. In [15], a high order SMO for the sensor-less operation of conventional DFIG systems is proposed and proved to be robust to parameter variations. The performance of the proposed high-order SMO is validated through simulations. In [16], A SMO based sensor-less control of the conventional DFIG system is presented. The proposed SMO uses the back-electromotive force (EMF) and the stator current as state variables. The robustness of the proposed SMO is validated through simulations and experiments. A SMO-based direct power sensor-less control technique for conventional DFIG systems is proposed in [17]. The proposed rotor speed/position estimation technique consists of the SMO which uses the stator flux linkage as state variable. A stator flux estimation method for DFIGs is proposed in [18].

Stellenbosch University https://scholar.sun.ac.za

The proposed observer aims at estimating the system state of the DFIG. The performance of the proposed observer is validated through simulations. The use of the SMO allows for the immunity against parameter variation and the robustness to load change [19]. However, the use of the SMO in the estimation process leads to high chattering effects on the estimated rotor speed/position. Generally, a low pass filter (LPF) is used to reduce the chattering effects. However, the use of a LPF leads to a high response time.

In [20, 21], Shen *et al.* introduced the slip frequency phase locked loop (PLL) for sensor-less operation of the conventional DFIG systems. The PLL is used for the extraction of the speed/position of the rotor. The proposed technique utilizes the information contained in the three-phase stator current, the three-phase rotor currents and the three-phase rotor voltage. This information is referred to an arbitrary reference frame in order to estimate the slip speed. During the process of estimating the slip speed, a central frequency is added, which leads to a slow dynamic response. Furthermore, the proposed PLL estimator is based on balanced operating conditions. A PLL estimator for a DFIG system under unbalanced operating conditions is proposed in [22]. The drawback of this estimation technique is that it depends on the magnetizing inductance. In [23, 24], the SMO associated with PLL estimators sensor-less control algorithms are for systems equipped with the permanent magnet synchronous machines (PMSMs) and the interior permanent magnet synchronous machines (IPMSMs).

In [25, 26], the rotor-tied doubly-fed induction generator (RDFIG) is first proposed as an alternative to the conventional DFIG system. The schematics of a standard DFIG system and a RDFIG are shown in Figure 1.1. From Figure 1.1(a), it can be seen that the rotor windings of the DFIG are directly connected to the grid/load through a transformer while the stator windings are connected to the grid through the back-to-back converter and the transformer. In the RDFIG topology, the stator-side converter is used to control the RDFIG while the grid-side converter (GSC) is used to maintain a DC-link voltage constant, as shown in Figure 1.1(b). In [25], it was concluded that, compared to the conventional DFIG at the same power rating, the RDFIG is smaller in size, thus utilizes less material and therefore it is cheaper. Furthermore, the RDFIG was shown to have better efficiency when compared to a similar conventional DFIG [27, 28]. In [29], the design process of the RDFIG is presented. The proposed design process consists of the calculation of the machine parameters and dimensions, and the use of finite element analysis (FEA). In addition, the optimisation process of the initial design is presented. The performance of the DFIG topologies (the RDFIG and the conventional DFIG) based on the design parameters is investigated in [30]. It was shown, in terms of power density, that there is not much of a difference between the RDFIG and the conventional DFIG. The improvement of the reactive power generation is demonstrated analytically using a wide range of machines in [31].

Stellenbosch University https://scholar.sun.ac.za

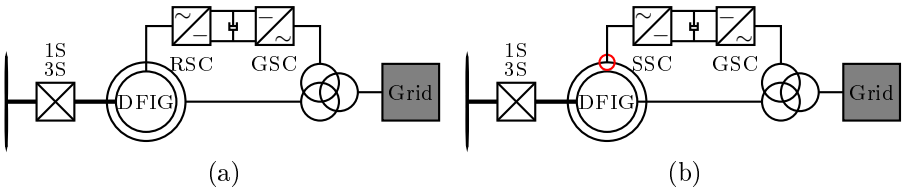

Figure 1.1: Schematics of DFIG systems: (a) Schematic of the conventional DFIG system; and, (b) Schematic of the RDFIG system.

In [28, 32], a sensor-based control strategy of a custom designed rotor-tied DFIG is proposed. The control strategy aims at the regulation of the electromagnetic torque. It is obvious that sensor-less control of the RDFIG could be beneficial in improving its reliability when realized.

In [1], a PLL-based SMO for rotor-tied DFIG systems is proposed. The proposed SMO uses the stator current and the back EMF as state variables, while the PLL estimator includes a judgment function. The judgment function is used to eliminate the phase shift of π introduced in super-synchronous operating conditions (when the slip speed is negative) [1]. However, in this technique a large slip angle error is observed especially at the transition from synchronous to super-synchronous operating conditions.

1.2 Problem statement

The knowledge of the rotor position/speed is necessary for the high performance of any control system in RDFIG-based WECSs. Inaccurate information on rotor speed/position or even failure of the position/speed sensor degrades the performance of the control system. Further, it can cause the failure of other components in the RDFIG-based WECSs or even cause instability of the whole system. In addition, the use of the rotor position sensors increases the cost, size and hardware wire complexity of the RDFIG-based WECSs, as noted for DFIG-based WECS in [33–35]. In harsh environments such as rural areas or off-shore areas, the position/speed sensor (encoder) can be subject to a high failure rate [36].

Although encoder-/sensor-less control of DFIGs has been under investigation for a while, there are still some key issues that still needs to be resolved for the sensor-less operations of the RDFIG-based WECSs. These issues include the robustness of the control scheme, the dynamic performance and the efficiency of the sensor-less operation of the RDFIG system. In addition, The PLL estimator using the *sine* function to track the real angle can be inaccurate with a phase shift of π in reverse operating conditions or when sign of the real angle to be tracked is negative [23, 24].

As previously mentioned, the speed estimation techniques based on SMO

Stellenbosch University https://scholar.sun.ac.za

are immune to parameter variations whilst being robust to load change [19]. However, the use of the SMO in the estimation process leads to high chattering effects on the estimated rotor speed/position. Generally, a low pass filter (LPF) is used to reduce the chattering effects. However, the use of a LPF leads to a higher response time.

1.3 Aim and objectives

The main aim of this research project is to develop and evaluate several slip speed estimators for sensor-less control of the RDFIG-based WECSs. The performance of the developed sensor-less control algorithms for RDFIG-based WECSs are evaluated through experiments under various operating conditions. The aim of this thesis can be broken down into the the following objectives:

- Develop, implement and evaluate a slip speed/position estimation technique for the sensor-less control of the grid-connected RDFIG-based WECS. The slip speed estimator is based on the association of the SMO and the PLL estimator.
- Develop, implement and investigate an adaptive sliding mode observer (ASMO)-based estimator for sensor-less control of the grid-connected RDFIG-based WECS. The slip speed/position is extracted using a PLL estimator.
- Develop, implement and investigate a super-twisting sliding mode observer (STSMO) associated with the PLL estimator for the sensor-less vector control of grid-connected RDFIG-based WECSs.
- Develop, implement and investigate a sensor-less vector control strategy of grid-connected RDFIG-based WECSs in grid-connected mode that includes a slip speed/angle estimator based on the high-order sliding mode observer (HOSMO) associated with the PLL estimator.
- Compare the performance of the proposed slip speed estimators.

1.4 Unique contributions

The results in this thesis have been published in two conference proceedings and three journal articles. The proposed slip speed estimators are based on the association of the PLL estimator and the different sliding mode observers. This association improves the performance of the slip speed estimators by reducing the noise created by the sliding mode control function. The contributions of this thesis can be stated as follows;

Stellenbosch University https://scholar.sun.ac.za

- A slip speed/position estimator that is based on the association of the PLL estimator and an SMO is proposed. It aims to enhance the estimation performance. It yields an improvement on signal quality of the estimation and the robustness of the slip speed estimator. Usually, in standard PLL estimators, the phase detector is based on the *sine* function. Given that the *sign* of the slip angle could change depending on the operating conditions (sub-synchronous or super-synchronous), there could be an introduction of a phase shift of π during the estimation process [1]. The proposed PLL estimator solves this problem, and thus, compared to the standard PLL estimator, the proposed PLL estimator operates with accuracy in all operating conditions. The proposed slip speed/angle estimator provides acceptable performance under rotor speed variations and it is shown to be immune to parameter variations [37].

- An ASMO-based rotor speed estimator for sensor-less of RDFIG system is proposed and experimentally investigated. A PLL estimator is used in order to track the slip/speed angle.

- The proposition of a PLL-based super-twisting sliding mode observer estimator for the sensor-less control of the RDFIG systems. The use of the super-twisting algorithm (STA) improves the performance. Furthermore, the STSMO gains are designed such that the Lyapunov stability criterion is satisfied and high dynamic performance is achieved [38].

- A high order sliding mode observer (HOSMO)-based estimator for the sensor-less control of the RDFIG systems is proposed. The PLL estimator is used for the estimation of the slip speed/angle. The proposed HOSMO takes into account the dynamics of the back-EMF space vector which enhances the estimation performance [39].

- A comparative study of the proposed slip speed estimators is presented.

1.5 Outline of the thesis

The outline and contributions of this thesis are given as follows.

- **Chapter 2 – Review on speed/position sensor-less control strategies for DFIG systems** In this chapter, an overview of important work published in the literature that is related to the work in the thesis is presented. A classification of rotor speed estimation methods for sensor-less operation of the RDFIG/DFIG systems is presented.

- **Chapter 3 – Background** In this chapter, the theoretical background for the development of the sensor-less control for RDFIG-based WECSs is presented.

Stellenbosch University https://scholar.sun.ac.za

- **Chapter 4 – Sensor-less vector control of the RDFIG-based WECS** In this chapter, the proposed sensor-less control strategy for the RDFIG systems is presented.
- **Chapter 5 – Slip speed estimators for sensor-less control of RDFIGs** In this chapter, the slip speed estimators for sensor-less control of RDFIG systems are presented.
- **Chapter 6 – Experimental results and discussions** In this chapter, the experimental results on the proposed sensor-less control strategies are presented.
- **Chapter 7 – Conclusions and recommendations on future works** In Chapter 7, the conclusions drawn from the experimental results discussed in chapter 6 and the recommendation on future works are presented.

Stellenbosch University https://scholar.sun.ac.za

Chapter 2

Review of rotor speed/position estimators for the sensor-less control of DFIG systems

2.1 Introduction

In this chapter, a review on the rotor speed/position estimation techniques for the sensor-less control of the DFIG and RDFIG systems is presented.

2.2 Classification of speed/postion estimation methods

In the last few decades, intensive research on encoderless control strategies, of electrical machines has been conducted in order to increase the reliability of the control systems during the failure of the rotor/position sensor. A comprehensive review of position/speed sensor-less control of DFIG systems is discussed in [5]. Also, a review of position sensor-less control strategies for permanent magnet synchronous motor (PMSM)-based WECSs is discussed in [40]. In this chapter, a thorough and updated literature review on rotor position/speed estimation methods for sensor-less control of DFIG systems is presented. The estimation methods are applicable to both conventional DFIG and RDFIG systems.

One can distinguish two major approaches of rotor position/speed estimation methods in the sensor-less control of DFIG systems. These approaches are the model-based estimation methods and the saliency-based estimation methods. A classification of the speed/position estimation methods proposed in the literature is shown in Figure 2.1. The following section provide a literature review on the sensor-less control of the DFIG systems. In this case, the rotor of the DFIG is connected to the grid through the back-to-back converter

Stellenbosch University https://scholar.sun.ac.za

whilst the stator is directly connected to the grid. These estimation methods can be applicable to the RDFIG systems.

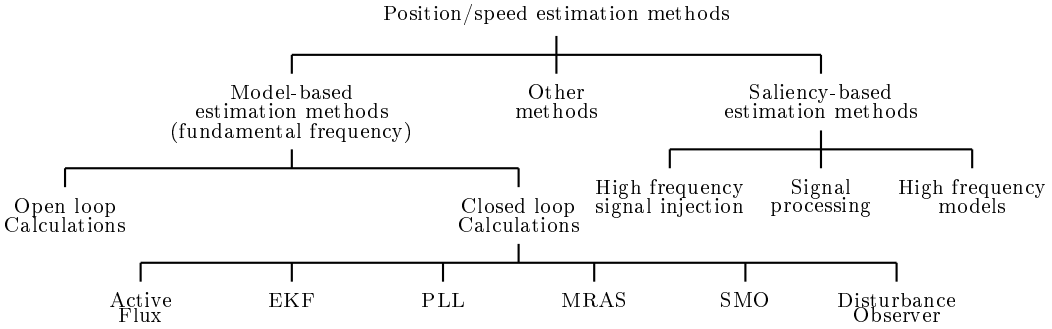

Figure 2.1: Classification of position/speed estimation methods.

2.3 Model-based estimation methods

Model-based rotor position/speed estimation methods developed based on the conventional DFIG model at the fundamental frequency [5]. The model-based estimation methods are suitable for meduim-speed and high-speed applications [40]. They are generally grouped into two categories: the open loop calculations and closed loop observers as shown in Figure 2.1. The open loop calculations are easy to implement. In the closed loop calculations, the state variables of the DFIG (back-EMF, stator current, rotor current or rotor flux) are used as inputs. Using the DFIG model, the state of interests are deduced. The estimated rotor speed/angle is extracted from the calculated state of interests. In the closed loop observers, both the state variable and the error between the outputs of the plant and that of the observer are input to the observer. The observer gains are designed such that the state variable of the observer converge to their real values from the plant. In this way, the estimated speed/position can be extracted. There are several closed loop observers presented in the literature for the sensor-less control of the DFIG system. There exists the sliding mode observers (SMO), the extended Kalman filters (EKF), the disturbance observers and the model reference adaptive system (MRAS), the active flux methods and the phase locked loop (PLL), as it can be seen from Figure 2.1. In this section, the review of both the open loop calculations and the closed loop is presented.

2.3.1 Open loop calculations

Early work on the rotor position/speed estimation of the DFIG system is based on the comparison between the measured rotor current and the estimated rotor

Stellenbosch University https://scholar.sun.ac.za

current into the synchronous reference frame in order to deduce the rotor speed/position [9, 41, 42]. In [43], the rotor position is estimated based on the rotor flux linkage, and the rotor flux linkage is determined by integrating the back electromotive force (EMF). The drawback for this rotor position/speed estimation method is that it is inaccurate when used to determine the rotor flux linkage at synchronous speed [41]. This is because the rotor frequency is almost zero at synchronous speed [41].

In [44], an open loop and implicit sensor-less control of a DFIG is presented. In the proposed rotor speed estimator, only the knowlegde of the stator and rotor currents and the stator voltage are needed for extraction of the rotor speed/position. This estimation technique has the advantage of being devoided of any flux terms calculations. This is useful because the static error introduced by the integration in the flux expressions is avoided. Similar work is presented in [45], whereby a rotor position computation algorithm (RPCA) for the rotor position/speed sensor-less control strategy for the DFIG system is proposed. The proposed estimation method uses the reference frame properties together with the trigonometrical calculations for the estimation of the rotor speed. The advantage of the proposed method is that it does not involve any voltage integration, recursive inverse trigonometric calculations nor does it assume a constant stator flux linkage. The proposed rotor speed/position estimator is validated by experiment, and it is shown that machine parameters have less effect on the rotor speed/position estimation. The estimated rotor speed is deduced from the time derivative of the rotor position and this can lead to spikes in the computed rotor speed [22]. Hence, the need to use the low pass filter (LPF). In [46], the influence of the rotor position error on the vector control is analysed. It is shown that this error influences the efficiency of the power control by offsetting the reference power from the actual measured power.

In [47, 48], an open loop sensor-less control scheme for a DFIG system is presented. The proposed rotor speed/position estimation method is based on the phase comparison of the estimated air-gap power and the measured rotor current in a common reference frame. The authors suggested the use of the air-gap power vector for the slip speed estimation. The measured stator and rotor currents, and the stator voltage are transformed into the $\alpha\beta 0$-reference frame in order to directly estimate the slip angle. In addition, the analysis of the sensitivity of the proposed method to the stator inductance was conducted. It led to the determination of an analytic expression for the estimation error of the slip angle with regards to the stator inductance, L_s. Experimental results were presented to validate the performance of the proposed estimator. A similar approach was proposed in [49].

Stellenbosch University https://scholar.sun.ac.za

2.3.2 Closed loop calculations

In the close loop observer approach, both the inputs of the plant and the error between the measured and the estimated outputs are the inputs of the observer. A proper design of the observer gains and that of an appropriate internal state adjustment scheme is necessary for the convergence of the observer outputs to the actual outputs. Based on the internal state adjustment scheme, one can distinguish the disturbance observer, the SMO, the MRAS-based observer, the PLL-based observer, the EKF and the active flux observer. Hence, all the observers are reviewed in this section.

2.3.2.1 Sliding mode observers

The notion of sliding mode control appeared first in the former Soviet Union in the early 1960s. A survey paper on sliding mode control was presented by Utkin in 1977 [50]. Since then, several research on the practical and the theoretical aspects of the sliding mode control has been presented in the literature [50–52]. In general, the sliding mode observer (SMO), is a closed loop observer which uses the discontinuous or continuous functions from the error between the real and estimated state variables. The system state reconstruction can be achieved by enforcing the sliding mode. The Lyapunov stability criteria is mostly used for the design of the sliding mode observer gains [15–18]. A schematics of a second order sliding mode observer for the DFIG system is displayed in Figure 2.2.

The SMO inherites the advantage of the sliding mode control such as, the disturbance rejection and strong robustness to parameter variations [19]. The SMO approach is widely used for sensor-less control strategies [15–18]. The SMO is well known for its easy implementation and robustness against machine parameter variations. However, the main drawback is the noise in the estimated signal that is introduced by the sliding mode control function/ discontinuous or continuous functions (mostly the signum, saturation or sigmoid functions). In [53], a sigmoid function which is a continous function was used in order to mitigate the noise in the estimated signal. However, the experi-

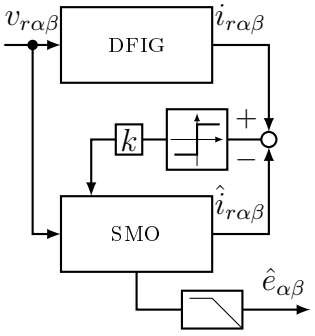

Figure 2.2: Illustration of a sliding mode observer.

Stellenbosch University https://scholar.sun.ac.za

mental results show that there is still lesser noise in the estimated signal. It is common to use the inverse tangent function in order to estimate the rotor position/speed. This implies the use of filters to filter the noise. However, the phase shift that comes with the use of the filter requires some compensations [1]. Based on the selected sliding mode control functions, several types of SMOs can be realised, as shown in Figure 2.3.

A. Second order sliding mode observer

In [16], a stator current-based sliding mode observer for sensor-less vector control of the conventional DFIG system is presented. The stator current is used as state variables. Given that an inverse tangent (*atan*) function, a second order low pass discrete butter-worth filter is is utilized for suppressing the noise in the estimated signal. The phase shift introduced by the filter is compensated by adding the phase of the filter itself. The robustness of the proposed sensor-less control strategy is verified using simulations and experimental results. However, the drawback of this method is that the dynamics of the back EMF are neglected for the construction of the sliding mode observer. Therefore, the estimation performance is limited during transient operating conditions. In [17], a stator flux-based SMO is proposed for the sensor-less direct power control of conventional DFIG systems. The stator flux linkage is used as a state variable. The rotor position is calculated using an inverse tangent, *atan*, function which implies the use of a low pass filter. The estimated rotor position is directly used in the direct power control algorithm for the determination of the sector numbers. The performance of the proposed sensor-less control strategy is only validated through simulations. However, the effect of the noise contained in the estimated rotor position on the direct power control algorithm is neglected. In addition, the proposed sliding mode observer does not take into consideration the dynamics of the stator flux linkage.

In [1], a PLL-based sliding mode observer for sensor-less vector control of rotor-tied doubly-fed induction generators (RDFIG) systems is presented. The proposed sensor-less control strategy holds the advantage of starting the estimation of the rotor position even before the RDFIG system is connected to the grid (in grid-connected mode). The proposed second order sliding mode observer uses the stator current, as state variables. Instead of an inverse tangent (*atan*) function, a phase locked loop estimator (PLL) is

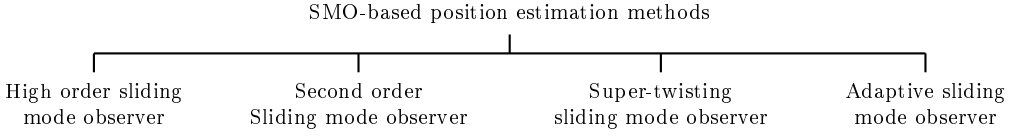

Figure 2.3: Classification of SMO-based rotor speed estimation methods.

Stellenbosch University https://scholar.sun.ac.za

used in order to enhance the estimation performance. This helps in avoiding the used of a low pass filter (LPF). Given that the PLL estimator uses a sine function, there could exist a phase shift of π when the slip angle is negative (in super-synchronous operating conditions) [23, 54]. Hence, a judgement function is proposed in order to compensate for the phase shift. The effectiveness of the proposed sensor-less vector control strategy is validated through simulations and experimental results. However, in this technique a large slip angle error can be seen especially at the transition from synchronous to super-synchronous operating conditions. Also, given that the dynamics of the back-EMF are neglected, the estimation performance is limited.

B. Adaptive sliding mode observer

In general, the sliding mode observers proposed in the literature for sensor-less control strategies of the rotor-tied/conventional DFIG systems make use of constant control gains [1, 16, 17]. This leads to undeasirable chattering while the system trajectories have already reached the sliding surface. To eliminate this chattering effect, the adaptive control gain approach is proposed in [55] where an adaptive sliding mode observer (ASMO) for the sensor-less control of a permanent magnet synchronous machine (PMSM) is proposed and disscussed. It was shown that the ASMO is superior to the standard SMO when chattering and disturbance response is considered. Simulation results were used to validate the performance of the ASMO. In [56], an ASMO is proposed. The proposed ASMO is used in order to improve the robustness, the smoothness and the fast transient performance of the estimation performance. In [57, 58], an ASMO is proposed for the adaptive parameters for a class of uncertain non linear systems.

C. Super-twisting sliding mode observer

The super-twisting algorithm (STA) for the SMO is also branded to be an excellent solution to alleviate the chattering behavior and it also improves its dynamic performance [59–67]. The supertwisting sliding mode observer uses the STA as the sliding mode control function/discontinous functions. The use of the STA aims at improving the performance of the sliding mode observer while reducing the noise created by the use of the saturation, sigmoid or signum functions. The stability of the STA is proved based on a strong constructed Lyapunov function. The STA-based SMO (STSMO) for the sensor-less control of an induction machine drive is proposed in [62]. Recently, similar work has been presented on permanent magnet synchronous machine drives in [63, 68].

Stellenbosch University https://scholar.sun.ac.za

D. High order sliding mode observer

In [15], a high-order sliding mode observer for rotor speed estimation is proposed. The rotor speed/position is estimated using a second order sliding mode. This proposed sensor-less control strategy has the advantage of being chatter-free and robust to parameter variations. Only simulation results were presented. A similar approach is conducted in [18] where a rotor speed estimation based on the stator flux, using a full order observer is proposed. However, only simulations are conducted to verify the proposed rotor speed/position estimation method.

2.3.2.2 Model reference adaptive system-based methods

The encoderless control based on model-reference adaptive system (MRAS) method is one of the most popular speed/position estimation methods in the literature due to its simplicity [5]. This rotor speed estimation method can be used in stand-alone mode as well as grid-connected mode of the DFIG systems [5]. However, the MRAS is very sensitive to machine parameter variations. The MRAS-based sensor-less control for the induction machine was first discussed in [69] whereby the author presented the small signal model together with the observer design. In general, the MRAS observer used for the sensor-less control of the DFIG system consists of an adjustable model, a reference model and an adaptive mechanism [70–87]. A schematic of the MRAS observer is shown in Figure 2.4. The output of the adaptive mechanism tunes the adjustable model so that the state variables in both models converge. The reference model is usually composed of the dynamic equations of the DFIG with the reference output $\vec{x}$. This output can be any of the machine quantities (rotor current, stator current, rotor flux, stator flux or even the back emf), as shown in Figure 2.5. The MRAS observer can also be associated with other observers [40]. For example, the use of the sliding mode observer in the reference model in order to improve the robustness of the MRAS against parameter variations. The MRAS used for rotor speed/position estimation methods are reviewed below.

A. Stator flux-based MRAS

In [80], the sensitivity to machine parameter variations of the stator flux-based MRAS, rotor current-based MRAS and rotor flux-based MRAS is investigated. It is shown that the estimation error in the rotor current is only affected by the stator inductance inaccuracy. The effect of the stator resistance was not investigated. However, when calculating the stator flux, the integration of the electromotive force includes the stator voltage offsets. The presence of the LPF leads to a lagging estimated output which is the source of the error in the estimated speed.

Stellenbosch University https://scholar.sun.ac.za

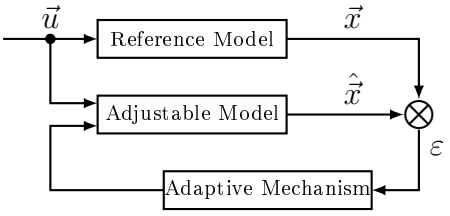

Figure 2.4: Schematic of a MRAS-based rotor speed estimation.

In [88], the reduced-order MRAS observer is presented, whereby, the reference model is essentially based on the dynamic model since the stator flux linkage is assumed to be available. The design of the observer is presented and simulation results are presented in order to validate the performance of the proposed rotor speed/position estimation algorithm. In [89], the harmonic analysis of a stator-flux based MRAS observer for rotor speed estimation is discussed. The authors showed through simulations, that the presence of harmonics, in the stator current and rotor current affect the accuracy of the estimated rotor speed/position. Hence, a harmonic compensation term ($A\sin(2\theta_{sl}+\phi)$) is added to the rotor current in the $\alpha\beta 0$-reference frame in order to mitigate the error in the rotor speed/ position estimation.

Usually, the errors, ε, in the MRAS are obtained from the cross product, as portrayed in Figure 2.4. This leads to a nonlinear and non-monotonic function. These properties cause high transients when starting on the fly [90]. A solution to this drawback is proposed in [90] whereby the inverse tangent function was proposed instead of a cross product. However, the proposed method leads to a high computational burden. The error, ε, deduced from the cross product of the real state variable $\vec{x}$, and the estimated state variable, $\hat{\vec{x}}$, requires the use of a LPF. In order to address this aspects in [91], the authors proposed to add correction terms under the integration of the electromotive force, which is proportional to the difference between the voltage model and the current model of the stator flux linkage. The advantage of this technique is that it improves the rotor speed/position estimation by making it less sensible to parameter variations [91].

In [92], a simple time-dynamic brush-less doubly fed induction generator (BDFIG) model is proposed. From this proposed mathematical model, the

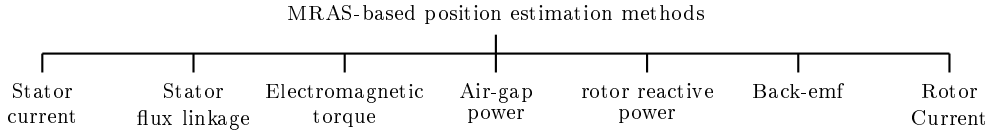

Figure 2.5: Classification of MRAS-based rotor speed/position estimation methods.

Stellenbosch University https://scholar.sun.ac.za

rotor speed/angle is deduced by estimating the winding flux. The performance of the the proposed control scheme is validated using experiments and simulations results. However, the estimated rotor angle is not presented in both the experiment and simulation results.

B. Air-gap power-based MRAS

In [93], an air-gap power-based MRAS observer for slip speed estimation is proposed. This method is based on comparing the measured rotor current space vector and the air-gap power. In this publication, the stability analysis is performed using small signal methods (using stability theory of sliding mode systems). In addition, the sensitivity analysis was also conducted showing that the proposed method is sensitive to the no-load active and reactive powers. Simulation and experiment results were presented to validate the proposed method. Similar work is presented in [94], were the focus is on the adaptive tuning of the stator inductance by adding a self tuning algorithm, since any mismatch can deeply affect the operation of the grid-connected DFIG. To realise the adaptive mechanism tuning, the authors suggested a minimisation of the error between the squared modulus of two air-gap complex power space vectors. In addition, a discussion on the the criterion to settle the dynamics of the adaptation mechanism is performed. The proposed method was tested using experiments. It was shown that the performance of the proposed sensor-less control strategy is satisfactory.

C. Electromagnetic torque-based MRAS

In [95], a rotor speed estimator that is based on the electromagnetic torque calculations is proposed. This method uses the electromagnetic torque as a working error variable. The electromagnetic torque can be expressed in the $\alpha\beta 0$-reference frame as a function of the stator and rotor currents, and the rotor position. In this method, the error to be driven to zero is determined by the difference between the electromagnetic torque evaluated by the power transferred across the air-gap in the synchronous reference frame and the electromagnetic torque that is evaluated from the stator and rotor currents, and rotor position in the $\alpha\beta 0$-reference frame. Also, the stability of the proposed method was investigated and led to the determination of the instability region (a circle with a diameter equal to the no-load stator current).

D. Reactive power-based MRAS

An MRAS observer based on the rotor reactive power is proposed in [78, 96]. This estimation method has the advantage of not being dependant on the rotor resistance. The performance of the proposed estimation method is validated under various operating conditions such as under balanced, unbalanced or non-linear loads. In addition, an on-line estimation of the

Stellenbosch University https://scholar.sun.ac.za

magnetising inductance is proposed in order to improve the control of the system. The estimated slip angular speed is used to tune the adjustable model in order for the PI controller to drive the error, ε, to zero. Since, the rotor voltage contains harmonics, then the estimated angular slip speed is very noisy.

E. Back EMF-based MRAS

In [13], a back-emf-based MRAS is presented, whereby the error, $\varepsilon = e - \hat{e}$, is to be driven to zero. In this publication, the adaptive mechanism and the stability of the closed loop system is derived using the Popov's criterion. Also, the tuning of the PI parameters in the adaptive model is limited by noise consideration [13]. The performance of the proposed method is validated using experiments.

F. Rotor current-based MRAS

In [97], a direct slip position-based MRAS observer self-sensing control method for a DFIG system, connected to a DC grid through a diode rectifier, is proposed. The authors aimed at maintaining the stator frequency constant. The control algorithm is based on the Γ-equivalent circuit of the DFIG. The control scheme is composed of an outer control loop, dedicated to the control of the stator frequency and an inner control loop that is dedicated to the control of the rotor current. The control is implemented in the synchronous reference frame. Further, a PLL-based method is also implemented in order to estimate the stator frequency which is used for the outer control loop. Compared to the standard PLL, the inputs of the PI controller is the dot product of the α-axis and β-axis stator voltage and the sine and cosine of the estimated stator angle (output of the proposed PLL). However, instead of using the sine, the cosine of the angle is used. In addition, the slip angle estimation is based on assuming that the d-axis stator current ($i_{sd} \approx 0$) is zero due to the diode bridge operation [98]. The experimental results and the simulation results presented in [97] showed that the slip error is very noisy. However, neither the sensitivity study nor the design criteria was discussed.

Recently in [99], a MRAS-based speed/position estimator which uses the rotor current in the synchronous reference frame is presented. The proposed rotor speed estimator utilizes only the stator resistance and the stator inductance. The adjustable model is composed of the current measurements transformed into the synchronous $dq0$-reference frame. The reference model is based on a new vector, $\vec{X} = k\vec{i}_r$, which is proportional to the rotor current space vector, $\vec{i}_r$. Also, in [99], a comparative study between the rotor speed estimation based on PLL and the proposed method is conducted. It is shown that the proposed method can catch on the fly and outperform

Stellenbosch University https://scholar.sun.ac.za

the rotor speed estimation based on the rotor speed PLL. However, the estimated rotor speed is noisy at all stator current.

G. Stator current-based MRAS

In [100], a stator current-based MRAS is described for brushless doubly-fed induction generators. The reference model is based on the simplified model of the BDFIG proposed in [101]. The design of the MRAS observer is done based on the control winding stator current. The performance of the proposed control scheme is validated using experiments and its performance was satisfactory.

2.3.2.3 Extended Kalman filter-based methods

The extended Kalman filter is a stochastic state observer which is a viable candidate for the rotor speed estimation. The EKF-based rotor speed estimation was first reported in [102], whereby the EKF algorithm procedure for rotor speed estimation is presented. However, the design of the process noise and the measurement covariance matrices is done by trial and error. Further, the state variables chosen were presented in both the synchronous $dq0$-reference frame and the $\alpha\beta0$-reference frame. This increases the complexity of the EKF algorithm since, at each iteration there should be a transformation during the prediction of the measurement and the update of the Kalman filter gain [103]. To validate the proposed EKF algorithm only simulations results were presented. In addition, the observability of the linearised DFIG model is not addressed. This issue was analysed and an extended Kalman filter was proposed as a rotor position observer in [103, 104]. Experimental results were presented in [104] while in [103] simulation results are presented.

It was shown that the EKF-based rotor speed estimation has great robustness to parameter inaccuracy, measurement noise and load changes [103, 104]. However, the EKF algorithm is computationally intensive and time consuming. In addition, the tuning of the matrices $\mathbf{Q}$ and $\mathbf{R}$ is difficult. The matrix $\mathbf{R}$ is linked to the measurement noise characteristics while the $\mathbf{Q}$ describes the confidence of the system model. To the best knowledge of the author, the unscented Kalman filter (UKF) has not been used yet as a rotor speed estimator in DFIG systems.

2.3.2.4 PLL-based methods

In [105,106], a PLL-based rotor position estimation method is presented. This method is used to simultaneously determine the stator speed, the rotor angle and the stator angle. The basic idea of this method is to transform the stator and rotor currents together with the stator voltage into the $dq0$-reference frame. This idea is based on the fact that for an induction machine the rotor magnetic field is equal and opposite to the stator magnetic field [105]. A

Stellenbosch University https://scholar.sun.ac.za

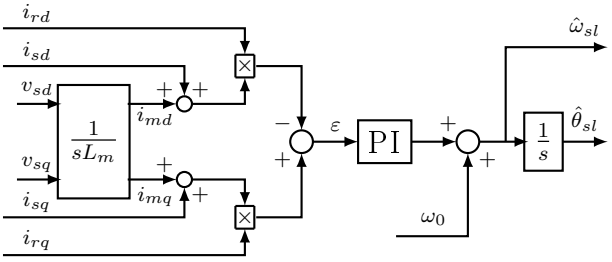

Figure 2.6: Schematic of a PLL-based rotor speed estimation.

schematics of the PLL estimator is depicted in Figure 2.6. However, when a central frequency, ω_0, is added as portrayed in Figure 2.6, this can lead to a long response time. Further, at lower speeds the use of a larger central frequency, ω_0, could lead to steady state errors. A similar approach is presented in [20, 21]. Here, based on the Kirchoff's law and based on the equivalent circuit of the DFIG, a pseudo rotor current which rotates at slip speed into the synchronous $dq0$-reference frame is deduced. This method has the advantage of being immune to the change of stator and rotor resistances. It needs only the magnetising inductance L_m.

In [107], the performance comparison of the sensorless algorithm-based MRAS and PLL rotor angle estimation is investigated. The comparison is based on the start-up operating conditions and the error of the rotor position angle. It is shown that the stator-flux MRAS observer has a poorer settling time performance during start-up compared to PLL-based rotor speed estimation. Furthermore, under speed variation the PLL-based method showed better performance than the stator flux PLL. In [22] the rotor speed estimation method presented in [105,106] has been extended to include unbalanced operating conditions. The authors proposed a PLL-based rotor estimation algorithm that associates the estimation of the rotor speed with the central frequency and the PLL-based speed estimation technique discussed in [105, 106]. This add-on scheme uses the rotor and the stator currents together with the stator voltage measurements. Hence, its main drawback being the dependency to the magnetising inductance.

2.3.2.5 Active flux methods

In [108], the active flux concept for position sensor-less control of unified AC drives is presented. The active flux concept consists of converting the salient poles travelling field machines into non-salient pole ones mathematically. The active flux concept was designed for a synchronous machine and an induction machine. The proposed estimation technique was verified experimentally. A review on active flux methods for AC drives is presented in [109].

Stellenbosch University https://scholar.sun.ac.za

2.3.2.6 Disturbance observer-based methods

In [110], the disturbance observer and the sliding mode observer schemes for sensor-less control of induction machines are compared. Compared to the sliding mode observer scheme, it was shown that the disturbance observer-based sensor-less control strategy was simpler in the designed implementation. It was suggested that the disturbance observer scheme should be used with parameter estimation algorithms. In [14], a speed sensor-less mode predictive control based on the disturbance observer for induction motor drives. The proposed control strategy is validated through simulations.

2.4 Saliency-based estimation methods

For the saliency-based methods, the rotor position is estimated from the position-dependant machine saliency. Usually, a high-frequency excitation is required. These estimation methods are suitable for low speed applications. The saliency-based estimation method presented in the literature for DFIG systems can be categorised into the signal processing methods and the high frequency methods.

2.4.1 High Frequency signal injection methods

In [111, 112], an investigation on the sensorless control based on the high frequency injection signal is conducted. The method consists of injecting high frequency current into the rotor which induces a high frequency voltage in the stator side, while measuring the phase shift between the induced high frequency voltage and the injected high frequency rotor current,thus obtaining the information regarding the speed is deduced. Similar approach is proposed in [113], where the authors suggest the injection of a high frequency rotor voltage which induces a high frequency voltage in the stator side. The rotor speed or the rotor position is estimated by measuring the phase shift between the injected rotor voltage and the induced stator voltage. In high frequencies, the stator inductance and that of the grid are very high. The addition of the grid impedance at high frequency can deter the estimation performance of these method [6]. This issue was adressed in [6], where the authors suggested to inject a high frequency voltage into the stator side using a grid-side converter. Also, a high frequency current cancellation method is proposed in order to reduce the effect of the harmonics on the rotor side. Although this technique has high accuracy in estimating rotor position even during low speed operating conditions, it requires a complicated algorithm and additional equipment for the injection of high frequency signals. In addition, high harmonic distortion can lead to losses.

Stellenbosch University https://scholar.sun.ac.za

2.4.2 Signal processing methods

In [114], an estimation method of the rotor speed is described. In this method, a signal window is applied on the stator power signal. The signal window is determied through the use of the iscrete Fourier transform. Practical experiment on the wound rotor induction machine are used to validate the proposed estimation method. The boundaries of the narrow band are determined based on the range of the rotor speed in which the machine can operate. The performance of the proposed sensor-less control strategy are validated through experiments. A similar approach is followed in [8], where the window signal is applied to the stator current frequency.

2.4.3 High frequency model methods

In [115], an observer is proposed based on the injection of the fifth harmonic component of the stator voltage for rotor speed/position estimation. This estimation method is based on the rotor current and stator voltage measurements. In this method, a phase-locked loop is used to track the harmonic component of the rotor current, induced by the fifth harmonic of the stator voltage. The proposed observer is designed based on the equivalent circuit of the machine for the fifth harmonics. This method has the advantage of not requiring the stator current measurement. However, this method is very complex.

2.5 Other methods

A position sensorless control of a DFIG system that is connected to a DC micro-grid is described in [116]. In this configuration, the stator is directly connected to the DC micro-grid through a diode rectifier, and the rotor is fed by only one VSC. The sensor-less control strategy is based on the detection of the stator frequency, and it is designed to operate without any machine parameters. Then, the stator frequency and the reference stator frequency is inputted to a PI controller. The proposed control strategy is validated through experiments. A similar slip estimation method is presented in [117], describing the model predictive control of DFIG system connected to a DC grid. The proposed control strategy is validated through experiments.

2.6 Summary

In this chapter, the literature review on the rotor speed/position estimation techniques for sensor-less control of the DFIG and RDFIG systems is presented. It was shown that the rotor speed estimation techniques can be classified into the model-based methods, the saliency based methods and the other methods. The saliency-based estimation methods are mostly used for low

Stellenbosch University https://scholar.sun.ac.za

speed applications while the model-based estimation methods and the other estimation methods are mostly used for medium-speed and high-speed applications.

Stellenbosch University https://scholar.sun.ac.za

Chapter 3

Background

3.1 Introduction

In this Chapter, the background theory and the modelling of RDFIG-based WECSs are presented. In addition, the modelling of the main components of the RDFIG-based WECSs is presented. There are the wind turbine, the RDFIG, the DC-link and the filter. Further, the sliding mode observer and the PLL estimator are introduced.

3.2 Overview of the RDFIG-based WECS

A RDFIG-based WECS is shown in Figure 3.1. It can be seen that the RDFIG-based WECS consists of the wind turbine, the RDFIG, the back-to-back converters, the filter, the control system, the transformer and the point of common coupling (PCC).

3.3 Wind turbine model

In this section, the modelling of the wind turbine is introduced.

3.3.1 Mechanical power

The mechanical power captured by the wind turbine is expressed by [118–121]

$$P_m = \frac{1}{2} C_p(\varsigma, \beta) \rho_{\text{air}} \pi r^2 V_{wind}^3, \tag{3.1}$$

where P_m is the captured mechanical power; $C_p(\varsigma, \beta)$ is the power coefficient; ρ_{air} is the air density; r is the radius of the turbine propeller; and, V_{wind} is the wind speed. The power coefficient can be approximated as [122];

$$C_p(\varsigma, \beta) = 0.73\Big(\frac{151}{\varsigma} - 0.58\beta - 0.002\beta^{2.14} - 13.2\Big)e^{-18.5\varsigma_k}, \tag{3.2}$$

Stellenbosch University https://scholar.sun.ac.za

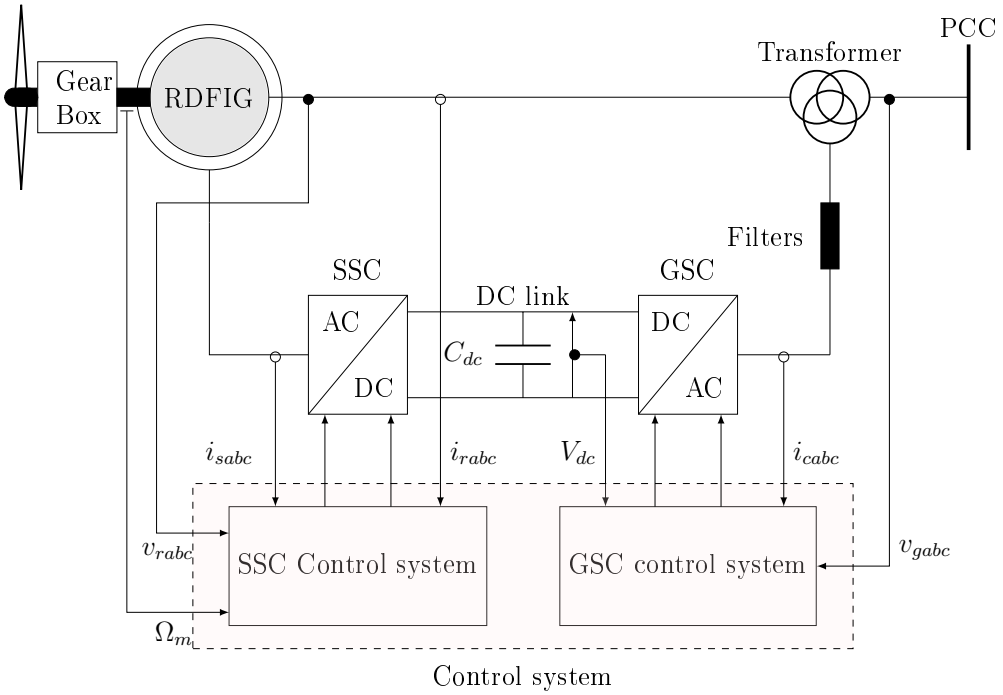

Figure 3.1: Schematic of the RDFIG-based WECS.

with

$$\varsigma = \frac{V_{tip}}{V_{wind}} = \frac{\Omega_t r}{V_{wind}}, \tag{3.3}$$

and

$$\frac{1}{\varsigma_k} = \frac{1}{\frac{1}{\varsigma - 0.02\beta} - \frac{0.003}{\beta^3+1}}. \tag{3.4}$$

In (3.2) and (3.3), ς is the tip-speed ratio and β is the pitch angle; and, $V_{tip} = \Omega_t r$ and Ω_t are the turbine tip speed and the angular speed of the rotor blades, respectively. The power coefficient denotes the portion of power that the wind turbine can extract from the total wind power available. The power coefficient is a specific characteristic of a given wind turbine. The optimal value of the power coefficient allows for the optimal capture of the available wind power. A typical relationship between the power coefficient and the tip speed ratio is shown in Figure 3.2.

3.3.2 Mechanical torque

From (3.1), the torque produced by the wind turbine is given by

$$\tau_t = \frac{C_p(\varsigma, \beta)\rho_{\text{air}}\pi r^2 V_{wind}^3}{2\Omega_t}, \tag{3.5}$$

where τ_t is the torque produced by the turbine.

Stellenbosch University https://scholar.sun.ac.za

Assume that the gearbox is perfect stiff, it yields that the mechanical torque delivered by the gearbox is given by

$$\tau_m = \frac{\tau_t}{m} = \frac{1}{2m} C_p(\varsigma, \beta) \rho_{\text{air}} \pi r^3 V_{wind}^2, \tag{3.6}$$

where τ_m is the mechanical torque while m is the gearbox ratio. The mechanical speed at the generator in the machine side is given by

$$\Omega_m = m\Omega_t, \tag{3.7}$$

Ω_m is the mechanical shaft speed of the generator.

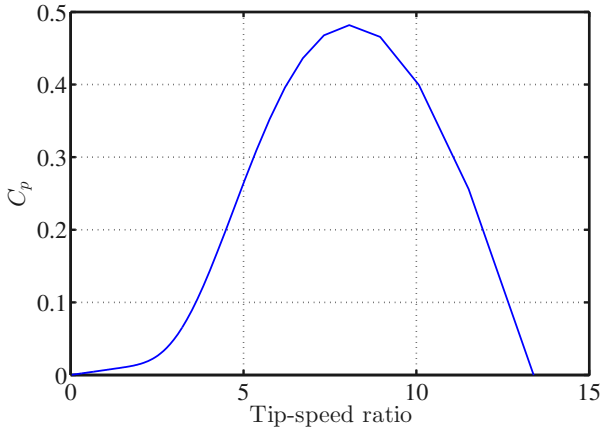

Figure 3.2: Tip-speed ratio(ς) versus power coefficient(C_p).

3.4 Operation principle of the RDFIG system

The RDFIG is a wound rotor induction machine that can be fed from the rotor and stator terminals at the same time. For the following discussions, it is assumed that the stator and rotor windings are sinusoidally distributed and the air gap is uniform. From a transformer model point of view, the RDFIG has its rotor as the primary and the stator as the secondary side. Even though, the RDFIGs and the DFIGs performs the same function in the WECSs, they operates slightly differently.

In the conventional DFIGs, the rotor rotates in the same direction as the stator and rotor magnetic fields as it can be seen in Figure 3.3(a). On the other hand, in the RDFIG, the rotor rotates in the opposite direction to that of the stator and rotor magnetic fields, as shown in Figure 3.3(b).

Stellenbosch University https://scholar.sun.ac.za

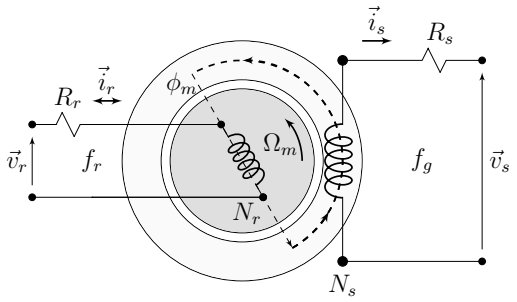

(a)

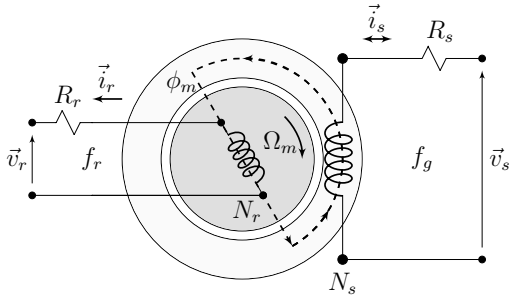

(b)

Figure 3.3: The DFIGs and RDFIGs operations: (a) DFIG operations; and, (b) RDFIG operations.

3.4.1 Slip and speed equations

For the RDFIGs, the rotor windings are connected to the grid, therefore the rotor voltage pulsates at grid frequency. The rotor voltage induces a rotating rotor flux that pulsates at the grid angular frequency which is described by

$$\omega_g = 2\pi f_g, \tag{3.8}$$

where f_g and ω_g are the fixed grid frequency and the angular grid speed. The rotor of the RDFIG rotates in the opposite direction to the rotor and stator magnetic fluxes as depicted in Figure 3.3(b). Hence, the mechanical shaft speed is negative with regards to the electrical rotor frequency. When the rotor of the RDFIG rotates, there is an induced electromotive force (EMF) in the stator windings that pulsates at slip frequency. Hence, both the stator voltage and current pulsate at the slip angular speed. The slip angular frequency is given by

$$\omega_s = \omega_g + \omega_r, \tag{3.9}$$

where ω_s is the slip angular frequency and ω_r is the electrical rotor angular speed. The electrical rotor angular speed is given by

$$\omega_r = P\Omega_m, \tag{3.10}$$

Stellenbosch University https://scholar.sun.ac.za

where P denotes the number of pole-pairs and Ω_m represents the mechanical shaft speed. It is important to note that the mechanical shaft speed, Ω_m, has a negative value. The slip, s, is given by

$$s = \frac{\omega_g + \omega_r}{\omega_g}. \tag{3.11}$$

When $s = 0$, the RDFIG operates under synchronous operating conditions while when $s = 1$ the RDFIG is at standstill. When $s = -1$, the RDFIG rotates at twice the synchronous speed.

3.5 Power flow in RDFIG systems

Assuming that the RDFIG-based WECS is a lossless system, the mechanical power captured by the wind turbine is given by

$$P_m = P_g = P_r + P_s, \tag{3.12}$$

where P_m is the mechanical power, P_r is the generated power from the rotor side and P_s is the power generated from the stator side of the RDFIG. P_g is the total generated power by the RDFIG system. For the RDFIG, there exists three operating modes with each having a specific power flow. These are the sub-synchronous operating mode, the synchronous operating mode and the super-synchronous operating mode. It is important to note for a RDFIG, given the rotor rotates in the opposite direction to that of the rotor magnetic flux, the electromagnetic torque and the mechanical torque are positive in generating mode. This implies that the expression of the active stator power is given by

$$P_m = \tau_m \omega_r, \tag{3.13}$$

The active rotor power is given by

$$P_r = -\tau_{em} \omega_g. \tag{3.14}$$

where τ_{em} is the electromagnetic torque. Note that there is a negative sign in (3.14) that guarantees that the generated power is negative because both the electromagnetic torque and the grid angular speed are positive. In a lossless RDFIG system, the expression in (3.12) can be rewritten using (3.13) and (3.14) as

$$P_s = P_m - P_r = \tau_m \omega_r - (-\tau_{em} \omega_g). \tag{3.15}$$

Also, in a lossless RDFIG system the electromagnetic torque is equal to the mechanical torque ($\tau_{em} = \tau_m$). Equation (3.15) can then be rewritten as

$$P_s = \tau_{em}(\omega_r + \omega_g). \tag{3.16}$$

Stellenbosch University https://scholar.sun.ac.za

Table 3.1: Generated Power and electromagnetic torque signs

slip range	Operating modes	signs
$0 < s < 1$	sub-synchronous mode	$P_r < 0$,$P_s > 0$ and $\tau_{em} > 0$
$s = 0$	synchronous mode	$P_r < 0$, $P_s = 0$ and $\tau_{em} > 0$
$s < 0$	super-synchronous mode	$P_r < 0$,$P_s < 0$ and $\tau_{em} > 0$

Substituting (3.14) into (3.16) yields

$$P_s = -P_r \frac{\omega_r + \omega_g}{\omega_g} = -sP_r. \tag{3.17}$$

From (3.17), it can be seen that, the sign of the stator active power (generated or consumed) also depends also on the sign of the slip. Based on (3.16) and the assumption that the generated power is negative, the polarity of different power according to the generating mode of the RDFIG system is summarised in Table 3.1.

A. Sub-synchronous operating mode

As it is shown in Table 3.1, when the RDFIG operates under sub-synchronous operating mode, the absolute electrical angular rotor speed is less than that of the grid angular speed. Thus, the slip is positive and less than one. The RDFIG system generates active power from the rotor side while it consumes active power through the back-to-back converters from the grid. The power flow scheme of a lossless RDFIG system is portrayed Figure 3.4. The active power through the back-to-back converters can increase or decrease the DC-link voltage. In order to guarantee maximum power transfer, the DC-link voltage is always maintains constant. The DC-link capacitor is used as the storage element in the DFIG system.

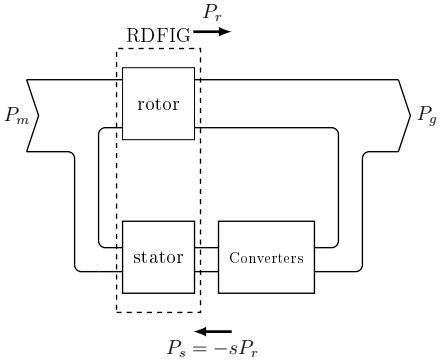

Figure 3.4: The RDFIG's sub-synchronous power flow scheme.

Stellenbosch University https://scholar.sun.ac.za

B. Synchronous operating mode

The slip is equal to zero in the synchronous mode, as it can be seen in Table 3.1. As a consequence, there is no induced EMF in the stator windings since this induced EMF in the rotor windings depends on the relative speed between grid angular speed and the electrical rotor speed. Therefore, the RDFIG operates as a synchronous generator. This operating mode does not allow for the production or the consumption of active power at the stator side of the RDFIG. The synchronous power flow of the RDFIG is presented in Figure 3.5.

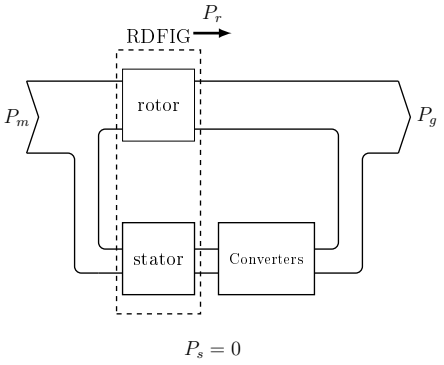

Figure 3.5: The RDFIG's synchronous power flow scheme.

C. Super-synchronous operating mode

Unlike in the sub-synchronous mode, the RDFIG produces active power from both the stator side and rotor side in the super-synchronous operating mode. The slip is negative as it can be seen from Table 3.1. As above mentioned, the DC-link voltage can increase or decrease depending on the power transfer through the back-to-back converter. Thus, the main aim of the grid side converter control is to to maintain the DC-link voltage constant.

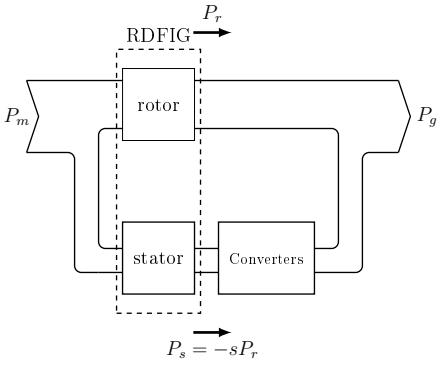

Figure 3.6: The RDFIG's super-synchronous power flow scheme.

Stellenbosch University https://scholar.sun.ac.za

3.6 Modelling of the RDFIG

In this section, the modelling of the RDFIG is presented. The modelling of the RDFIG in this section is similar to that presented in [27, 28, 31].

3.6.1 RDFIG modelling in *abc*-reference frame

The winding layout of a three-phase RDFIG is portrayed in Figure 3.7. The winding layout of a RDFIG is portrayed in Figure 3.7(a). The wye connected stator and rotor equivalent circuits of a RDFIG are shown in Figure 3.7(b). From Figure 3.7(b), and using Faraday's and Kirchoff's laws in the stator and rotor equivalent circuits of the RDFIG, the voltage equations of the induction

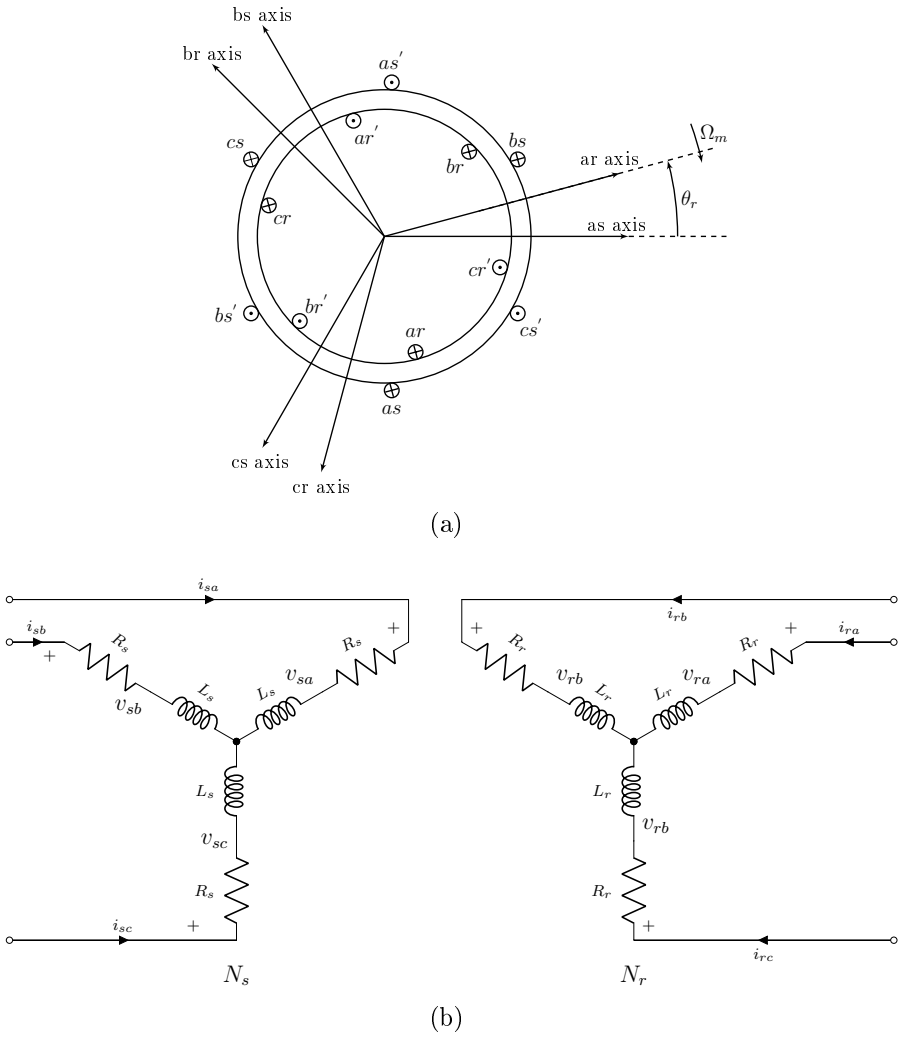

Figure 3.7: RDIFG schematics: (a) Winding layout of a two-pole RDFIG; and, (b) stator and rotor equivalent circuit of a wye-connected symmetrical RDFIG.

Stellenbosch University https://scholar.sun.ac.za

machine are

$$\begin{bmatrix} \boldsymbol{v_{sabc}} \\ \boldsymbol{v_{rabc}} \end{bmatrix} = \begin{bmatrix} \boldsymbol{R_s} & 0 \\ 0 & \boldsymbol{R_r} \end{bmatrix} \begin{bmatrix} \boldsymbol{i_{sabc}} \\ \boldsymbol{i_{rabc}} \end{bmatrix} + \frac{d}{dt} \begin{bmatrix} \boldsymbol{\lambda_{sabc}} \\ \boldsymbol{\lambda_{rabc}} \end{bmatrix}, \tag{3.18}$$

where $\boldsymbol{v_{sabc}}$ and $\boldsymbol{v_{rabc}}$ are the instantaneous three-phase stator and rotor voltages respectively; $\boldsymbol{i_{sabc}}$ and $\boldsymbol{i_{rabc}}$ are the three-phase stator and rotor currents respectively; and, $\boldsymbol{\lambda_{sabc}}$ and $\boldsymbol{\lambda_{rabc}}$ are the three-phase stator and rotor flux linkages respectively.

$\boldsymbol{R_r}$ and $\boldsymbol{R_s}$ are the stator and rotor resistance matrices respectively and they are given by

$$\boldsymbol{R_s} = \begin{bmatrix} R_s & 0 & 0 \\ 0 & R_s & 0 \\ 0 & 0 & R_s \end{bmatrix} \tag{3.19}$$

and

$$\boldsymbol{R_r} = \begin{bmatrix} R_r & 0 & 0 \\ 0 & R_r & 0 \\ 0 & 0 & R_r \end{bmatrix}, \tag{3.20}$$

with R_r and R_s are the per-phase rotor and stator resistances respectively. When the stator variables are referred to the rotor, referring all the stator variables to rotor, the instantaneous three-phase stator voltage is given by

$$\boldsymbol{v'_{sabc}} = \boldsymbol{R'_s} \boldsymbol{i'_{sabc}} + \frac{d\boldsymbol{\lambda'_{sabc}}}{dt}, \tag{3.21}$$

where

$$\boldsymbol{v'_{sabc}} = \frac{N_r}{N_s} \boldsymbol{v_{sabc}}, \qquad \boldsymbol{i'_{sabc}} = \frac{N_s}{N_r} \boldsymbol{i_{sabc}}, \qquad \boldsymbol{\psi'_{sabc}} = \frac{N_r}{N_s} \boldsymbol{\lambda_{sabc}}, \tag{3.22}$$

and

$$\boldsymbol{R'_s} = \left(\frac{N_r}{N_s}\right)^2 \boldsymbol{R_s}, \qquad \boldsymbol{L'_s} = \left(\frac{N_r}{N_s}\right)^2 \boldsymbol{L_s}, \qquad \boldsymbol{L'_{sr}} = \frac{N_r}{N_s} \boldsymbol{L_{sr}} \tag{3.23}$$

where the superscript ($'$) represents the stator variables referred to the rotor windings. In order to simplify the notations, the superscript ($'$) is taken out from here and on.

The three-phase rotor flux linkage and the referred three-phase stator flux linkage are then given by

$$\begin{bmatrix} \boldsymbol{\lambda_{sabc}} \\ \boldsymbol{\lambda_{rabc}} \end{bmatrix} = \begin{bmatrix} \boldsymbol{L_s} & \boldsymbol{L_{sr}} \\ (\boldsymbol{L_{sr}})^t & \boldsymbol{L_r} \end{bmatrix} \begin{bmatrix} \boldsymbol{i_{sabc}} \\ \boldsymbol{i_{rabc}} \end{bmatrix}, \tag{3.24}$$

where the stator inductance matrix is given by

$$\boldsymbol{L_r} = \begin{bmatrix} L_{sl} + L_{sm} & -\frac{1}{2}L_{sm} & -\frac{1}{2}L_{sm} \\ -\frac{1}{2}L_{sm} & L_{sl} + L_{sm} & -\frac{1}{2}L_{sm} \\ -\frac{1}{2}L_{sm} & -\frac{1}{2}L_{sm} & L_{sl} + L_{sm} \end{bmatrix}, \tag{3.25}$$

Stellenbosch University https://scholar.sun.ac.za

the referred mutual inductance matrix is given by

$$\boldsymbol{L_{sr}} = L_{sm}\begin{bmatrix} \cos\theta_r & \cos(\theta_r + \frac{2\pi}{3}) & \cos(\theta_r - \frac{2\pi}{3}) \\ \cos(\theta_r - \frac{2\pi}{3}) & \cos\theta_r & \cos(\theta_r + \frac{2\pi}{3}) \\ \cos(\theta_r + \frac{2\pi}{3}) & \cos(\theta_r - \frac{2\pi}{3}) & \cos\theta_r \end{bmatrix}, \tag{3.26}$$

and the referred rotor inductance matrix is given by

$$\boldsymbol{L_r} = \begin{bmatrix} L_{rl} + L_{sm} & -\frac{1}{2}L_{sm} & -\frac{1}{2}L_{sm} \\ -\frac{1}{2}L_{sm} & L_{rl} + L_{sm} & -\frac{1}{2}L_{sm} \\ -\frac{1}{2}L_{sm} & -\frac{1}{2}L_{sm} & L_{rl} + L_{sm} \end{bmatrix}. \tag{3.27}$$

In (3.25)−(3.27), L_{sl} and L_{sm} are the leakage and magnetising inductances of the stator windings, respectively; L_{sr} is the mutual inductance; and, L_{rl} is the leakage rotor inductance. The mutual inductance matrix depicted in (3.26) depends on the electrical rotor position/angle, θ_r. The electrical rotor angle is given by

$$\theta_r = \int_0^t \omega_r dt + \theta_r(0), \tag{3.28}$$

where $\theta_r(0)$ is the initial electrical rotor angle. The electrical rotor angle is time dependant. Thus, there exist the need to transform the machine variables and parameters into a reference frame where the mutual inductances are constant.

3.6.2 RDFIG modelling in the synchronous $dq0$-reference Frame

Reference frames are used to eliminate the time dependency terms of the mutual inductance of the AC machines. In Figure 3.8, the stationary $\alpha\beta0$-reference frame, the synchronous $dq0$-reference frame and the reference frame attached to the rotor of the RDFIG are presented.

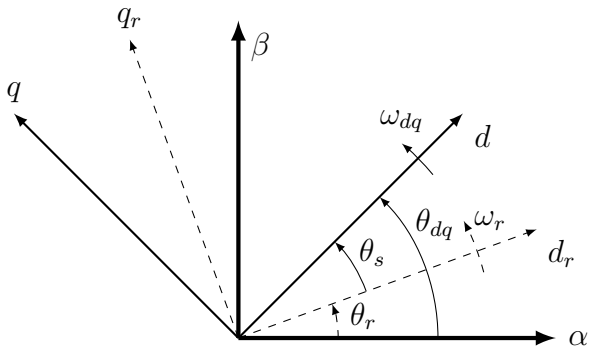

Figure 3.8: Schematic of the reference frames.

Stellenbosch University https://scholar.sun.ac.za

The transformation matrix, $\boldsymbol{T_{dq}}$, used to transform any quantity from the *abc*-reference frame into the rotating *dq*0-reference frame is given by

$$\boldsymbol{T_{dq}} = \frac{2}{3}\begin{bmatrix} \cos(\theta_{dq}) & \cos(\theta_{dq} - \frac{2\pi}{3}) & \cos(\theta_{dq} + \frac{2\pi}{3}) \\ \sin(\theta_{dq}) & \sin(\theta_{dq} - \frac{2\pi}{3}) & \sin(\theta_{dq} + \frac{2\pi}{3}) \\ \frac{1}{2} & \frac{1}{2} & \frac{1}{2} \end{bmatrix}, \tag{3.29}$$

where,

$$\theta_{dq} = \int_0^t \omega_{dq} dt + \theta_{dq}(0). \tag{3.30}$$

Note that for the RDFIG system, the rotor quantities pulsates at grid frequency. θ_{dq} is the angle between the stationary reference frame and the rotating *dq*0-reference frame; ω_{dq} is the angular speed at which the *dq*0-reference frame rotates; $\boldsymbol{T_{dq}}$ is the transformation matrix from *abc*-reference frame to the rotating *dq*0-reference frame; and, $\theta_{dq}(0)$ is the initial value of the angle between the stationary reference frame and the arbitrary *dq*0-reference frame.

When the rotating *dq*0-reference frame is rotating at synchronous angular speed, it yields

$$\omega_{dq} = \omega_g \tag{3.31}$$

and

$$\theta_{dq} = \theta_g, \tag{3.32}$$

where $\theta_g = \int_0^t \omega_g dt + \theta_g(0)$ is the angle between the stationary reference frame and the synchronous reference frame, as shown in Figure 3.8. θ_g is calculated from either the grid voltage space vector (when voltage-oriented control (VOC) is used) or from the rotor flux linkage space vector (when field oriented control (FOC) is used).

3.6.2.1 Three-phase rotor voltages

Transforming the three-phase rotor voltages in (3.18) into the synchronous *dq*0-reference frame using (3.29), yields

$$\begin{bmatrix} v_{rd} \\ v_{rq} \end{bmatrix} = R_r \begin{bmatrix} i_{rd} \\ i_{rq} \end{bmatrix} + \frac{d}{dt}\begin{bmatrix} \lambda_{rd} \\ \lambda_{rq} \end{bmatrix} + \omega_g \begin{bmatrix} -\lambda_{rq} \\ \lambda_{rd} \end{bmatrix}, \tag{3.33}$$

where v_{rd} and v_{rq} are the *d*-axis and *q*-axis rotor voltages respectively; i_{rd} and i_{rq} are the *d*-axis and *q*-axis rotor current, respectively; and, λ_{rd} and λ_{rq} are the *d*-axis and *q*-axis rotor flux linkages respectively.

3.6.2.2 Three-phase stator voltages

Given that the three-phase stator current rotates at slip frequency, the transformation matrix is given by

$$\boldsymbol{T_{dq}} = \frac{2}{3}\begin{bmatrix} \cos(\theta_s) & \cos(\theta_s - \frac{2\pi}{3}) & \cos(\theta_s + \frac{2\pi}{3}) \\ \sin(\theta_s) & \sin(\theta_s - \frac{2\pi}{3}) & \sin(\theta_s + \frac{2\pi}{3}) \\ \frac{1}{2} & \frac{1}{2} & \frac{1}{2} \end{bmatrix}, \tag{3.34}$$

Stellenbosch University https://scholar.sun.ac.za

and

$$\theta_s = \int_0^t \omega_s dt + \theta_s(0), \tag{3.35}$$

where $\omega_s = \omega_g + \omega_r$ is slip angular speed and θ_s is the slip position.

Thus, the three-phase stator voltages transformed into the synchronous $dq0$-reference frame become

$$\begin{bmatrix} v_{sd} \\ v_{sq} \end{bmatrix} = R_s \begin{bmatrix} i_{sd} \\ i_{sq} \end{bmatrix} + \frac{d}{dt} \begin{bmatrix} \lambda_{sd} \\ \lambda_{sq} \end{bmatrix} + \omega_s \begin{bmatrix} -\lambda_{sq} \\ \lambda_{sd} \end{bmatrix}, \tag{3.36}$$

where v_{sd} and v_{sd} are the d-axis and q-axis stator voltages respectively; i_{sd} and i_{sq} are the d-axis and q-axis stator currents respectively; and, λ_{sd} and λ_{sq} are the d-axis and q-axis stator flux linkages respectively.

3.6.2.3 Three-phase flux linkages

The three-phase stator and rotor flux linkages into the synchronous $dq0$-reference frame are given by

$$\begin{bmatrix} \boldsymbol{\lambda_{sdq0}} \\ \boldsymbol{\lambda_{rdq0}} \end{bmatrix} = \begin{bmatrix} \boldsymbol{T_s L_s (T_s)^{-1}} & \boldsymbol{T_s L_{sr} (T_r)^{-1}} \\ \boldsymbol{T_s (L_{sr})^T (T_s)^{-1}} & \boldsymbol{T_r L_r (T_r)^{-1}} \end{bmatrix} \begin{bmatrix} \boldsymbol{i_{sdq0}} \\ \boldsymbol{i_{rdq0}} \end{bmatrix}, \tag{3.37}$$

where

$$\boldsymbol{T_s L_s (T_s)^{-1}} = \begin{bmatrix} L_{sl} + L_m & 0 & 0 \\ 0 & L_{sl} + L_m & 0 \\ 0 & 0 & L_{sl} \end{bmatrix}, \tag{3.38}$$

$$\boldsymbol{T_r L_r (T_r)^{-1}} = \begin{bmatrix} L_{rl} + L_m & 0 & 0 \\ 0 & L_{rl} + L_m & 0 \\ 0 & 0 & L_{rl} \end{bmatrix}, \tag{3.39}$$

and

$$\boldsymbol{T_r (L_{sr})^T (T_s)^{-1}} = \boldsymbol{T_s L_{sr} (T_r)^{-1}} = \begin{bmatrix} L_m & 0 & 0 \\ 0 & L_m & 0 \\ 0 & 0 & 0 \end{bmatrix}. \tag{3.40}$$

In (3.38)−(3.40), L_{sl} and $L_m = \frac{3}{2} L_{sm}$ are the leakage inductance and the magnetising inductance respectively; and, L_{rl} is the leakage inductance referred to the stator. Substituting (3.38), (3.39) and (3.40) into (3.37), the d-axis stator and rotor flux linkages are given by

$$\lambda_{sd} = L_s i_{sd} + L_m i_{rd}, \tag{3.41}$$

$$\lambda_{sq} = L_s i_{sq} + L_m i_{rq}, \tag{3.42}$$

$$\lambda_{rd} = L_r i_{rd} + L_m i_{sd}, \tag{3.43}$$

and

$$\lambda_{rq} = L_r i_{rq} + L_m i_{sq}. \tag{3.44}$$

Stellenbosch University https://scholar.sun.ac.za

3.6.2.4 RDFIG equivalent circuit

In this section the space vector notation is particularly adopted for simplicity. Assuming that the space vector quantities in the synchronous reference frame are defined as

$$\vec{f}^{s} = f_d + jf_q, \tag{3.45}$$

where, the superscript s refers to the space vector in the synchronous reference frame. Based on the analysis conducted on the stator and rotor voltage equations in the of the RDFIG in the synchronous reference frame, the dynamics of the stator and rotor voltages space vectors are given by

$$\begin{bmatrix} \vec{v}_s^s \\ \vec{v}_r^s \end{bmatrix} = \begin{bmatrix} R_s & 0 \\ 0 & R_r \end{bmatrix} \begin{bmatrix} \vec{i}_s^s \\ \vec{i}_r^s \end{bmatrix} + \frac{d}{dt} \begin{bmatrix} \vec{\lambda}_s^s \\ \vec{\lambda}_r^s \end{bmatrix} + j \begin{bmatrix} -\omega_s & 0 \\ 0 & \omega_g \end{bmatrix} \begin{bmatrix} \vec{\lambda}_s^s \\ \vec{\lambda}_r^s \end{bmatrix}, \tag{3.46}$$

where $\vec{v}_s^s = v_{sd} + jv_{sq}$ and $\vec{v}_r^s = v_{rd} + jv_{rq}$ are the stator and rotor voltage space vectors, respectively; $\vec{i}_s^s = i_{sd} + ji_{sq}$ and $\vec{i}_r^s = i_{rd} + ji_{rq}$ are the stator and rotor current space vectors, respectively; and, $\vec{\lambda}_s^s = \lambda_{sd} + j\lambda_{sq}$ and $\vec{\lambda}_r^s = \lambda_{rd} + j\lambda_{rq}$ are the stator and rotor flux linkage space vectors, respectively. From (3.46), the equivalent circuit of the RDFIG in the synchronous reference frame is deduced and shown in Figure 3.9. In Figure 3.9, the magnetising current space vector $\vec{i}_{rm}^s$ is given by

$$\vec{i}_{rm}^s = \vec{i}_s^s + \vec{i}_r^s. \tag{3.47}$$

3.6.3 RDFIG modelling into the stationary $\alpha\beta 0$-reference frame

The modelling in the $\alpha\beta 0$-reference frame is important for the design of the observers proposed in this thesis. The approach to modelling the RDFIG in the $\alpha\beta 0$-reference frame is similar to that presented in section 3.6.2. However, the difference is that in the transformation matrix presented in (3.29), the angle θ_{dq} is equal to zero.

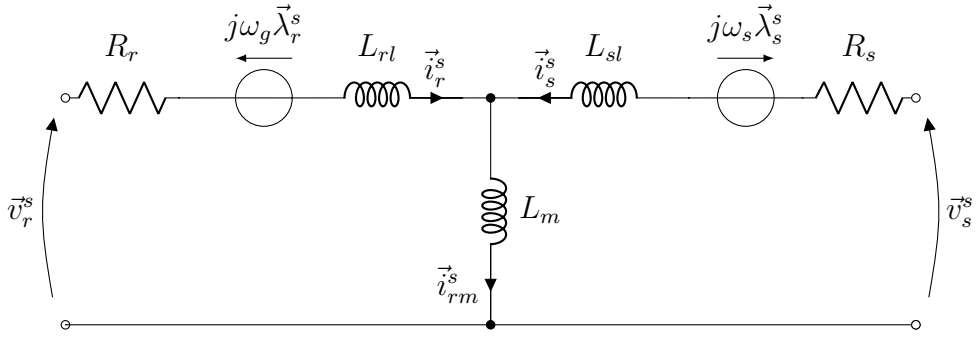

Figure 3.9: RDFIG equivalent circuit in the synchronous reference frame.

Stellenbosch University https://scholar.sun.ac.za

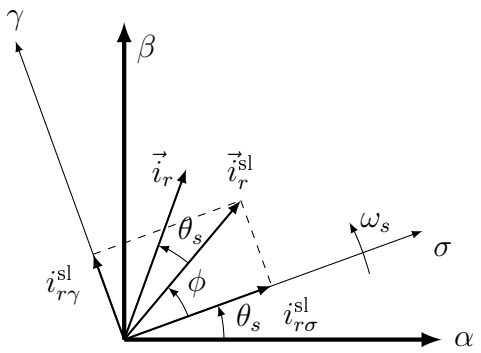

Figure 3.10: Vector diagram of the rotor current space vector.

3.6.3.1 Stator and rotor voltages

The expressions of the stator voltage into the $\alpha\beta 0$-reference frame are given by

$$\begin{bmatrix} v_{s\alpha} \\ v_{s\beta} \end{bmatrix} = \begin{bmatrix} R_s & 0 \\ 0 & R_s \end{bmatrix} \begin{bmatrix} i_{s\alpha} \\ i_{s\beta} \end{bmatrix} + \frac{d}{dt} \begin{bmatrix} \lambda_{s\alpha} \\ \lambda_{s\beta} \end{bmatrix} + \begin{bmatrix} 0 & \omega_r \\ -\omega_r & 0 \end{bmatrix} \begin{bmatrix} \lambda_{s\alpha} \\ \lambda_{s\beta} \end{bmatrix}, \tag{3.48}$$

where $v_{s\alpha}$ and $v_{s\beta}$ are the α-axis and β-axis stator voltages respectively; $i_{s\alpha}$ and $i_{s\beta}$ are the α-axis and β-axis stator currents respectively; and, $\lambda_{s\alpha}$ and $\lambda_{s\beta}$ are the α-axis and β-axis stator flux linkages respectively. The rotor voltage space vector transformed into the $\alpha\beta 0$-reference frame is given by

$$\begin{bmatrix} v_{r\alpha} \\ v_{r\beta} \end{bmatrix} = \begin{bmatrix} R_r & 0 \\ 0 & R_r \end{bmatrix} \begin{bmatrix} i_{r\alpha} \\ i_{r\beta} \end{bmatrix} + \frac{d}{dt} \begin{bmatrix} \lambda_{r\alpha} \\ \lambda_{r\beta} \end{bmatrix} + \begin{bmatrix} 0 & \omega_g \\ -\omega_g & 0 \end{bmatrix} \begin{bmatrix} \lambda_{r\alpha} \\ \lambda_{r\beta} \end{bmatrix}, \tag{3.49}$$

where $v_{r\alpha}$ and $v_{r\beta}$ are the α-axis and β-axis rotor voltages respectively; $i_{r\alpha}$ and $i_{r\beta}$ are the α-axis and β-axis rotor currents respectively; and, $\lambda_{r\alpha}$ and $\lambda_{r\beta}$ are the α-axis and β-axis rotor flux linkages respectively.

3.6.3.2 Stator and rotor flux linkages

The stator flux linkage transformed into the $\alpha\beta 0$-reference frame is given by

$$\begin{bmatrix} \lambda_{s\alpha} \\ \lambda_{s\beta} \end{bmatrix} = \begin{bmatrix} L_s & 0 \\ 0 & L_s \end{bmatrix} \begin{bmatrix} i_{s\alpha} \\ i_{s\beta} \end{bmatrix} + \begin{bmatrix} L_m & 0 \\ 0 & L_m \end{bmatrix} \begin{bmatrix} i_{r\alpha} \\ i_{r\beta} \end{bmatrix}, \tag{3.50}$$

and, the rotor flux linkage transformed into the $\alpha\beta 0$-reference frame is given by

$$\begin{bmatrix} \lambda_{r\alpha} \\ \lambda_{r\beta} \end{bmatrix} = \begin{bmatrix} L_r & 0 \\ 0 & L_r \end{bmatrix} \begin{bmatrix} i_{r\alpha} \\ i_{r\beta} \end{bmatrix} + \begin{bmatrix} L_m & 0 \\ 0 & L_m \end{bmatrix} \begin{bmatrix} i_{s\alpha} \\ i_{s\beta} \end{bmatrix}. \tag{3.51}$$

3.6.3.3 Stator current dynamics in the $\alpha\beta 0$-reference frame

Based on Figure 3.10, the rotor current can be written as

$$\begin{bmatrix} i_{r\alpha} \\ i_{r\beta} \end{bmatrix} = |\vec{i}_r^{\,\mathrm{sl}}| \begin{bmatrix} \cos(\theta_s + \phi) \\ \sin(\theta_s + \phi) \end{bmatrix}, \tag{3.52}$$

Stellenbosch University https://scholar.sun.ac.za

where $\vec{i}_r^{\,\mathrm{sl}} = |\vec{i}_r^{\,\mathrm{sl}}|e^{j\phi}$ is the rotor current space vector in the slip reference frame (σ, γ); θ_s is the slip angle; ϕ is the phase angle of the rotor current in the slip reference frame. The magnitude of the rotor current space vector in the slip reference frame is given by

$$|\vec{i}_r^{\,\mathrm{sl}}| = \sqrt{(i_{r\gamma}^{\mathrm{sl}})^2 + (i_{r\sigma}^{\mathrm{sl}})^2}, \tag{3.53}$$

where $i_{r\sigma}^{\mathrm{sl}}$ and $i_{r\gamma}^{\mathrm{sl}}$ are the σ-axis and γ-axis rotor currents in the slip reference frame; and $\phi = \tan^{-1}\left(\frac{i_{r\gamma}^{\mathrm{sl}}}{i_{r\sigma}^{\mathrm{sl}}}\right)$. Substituting (3.52) into (3.50) yields

$$\begin{bmatrix}\lambda_{s\alpha}\\ \lambda_{s\beta}\end{bmatrix} = \begin{bmatrix}L_s & 0\\ 0 & L_s\end{bmatrix}\begin{bmatrix}i_{s\alpha}\\ i_{s\beta}\end{bmatrix} + |\vec{i}_r^{\,\mathrm{sl}}|\begin{bmatrix}L_m & 0\\ 0 & L_m\end{bmatrix}\begin{bmatrix}\cos(\theta_s+\phi)\\ \sin(\theta_s+\phi)\end{bmatrix}. \tag{3.54}$$

Substituting (3.54) into (3.48) and rewriting it, yields the dynamic equations of the stator current space vector of a RDFIG in the $\alpha\beta$0-reference frame, that is,

$$\begin{bmatrix}\dot{i}_{s\alpha}\\ \dot{i}_{s\beta}\end{bmatrix} = \begin{bmatrix}\frac{-R_s}{L_s} & \omega_r\\ -\omega_r & \frac{-R_s}{L_s}\end{bmatrix}\begin{bmatrix}i_{s\alpha}\\ i_{s\beta}\end{bmatrix} + \begin{bmatrix}\frac{1}{L_s} & 0\\ 0 & \frac{1}{L_s}\end{bmatrix}\begin{bmatrix}e_\alpha\\ e_\beta\end{bmatrix} + \frac{1}{L_s}\begin{bmatrix}v_{s\alpha}\\ v_{s\beta}\end{bmatrix}, \tag{3.55}$$

where e_α and e_β are the α-axis and β-axis back-EMFs, respectively. The back-EMF space vector transformed into the $\alpha\beta$0 reference frame is given by

$$\begin{bmatrix}e_\alpha\\ e_\beta\end{bmatrix} = L_m|\vec{i}_r^{\,\mathrm{sl}}|\omega_g\begin{bmatrix}\sin\theta_k\\ -\cos\theta_k\end{bmatrix}. \tag{3.56}$$

where $\theta_k = \theta_s + \phi$. From (3.56), the dynamic equations of the back-EMF space vector in the $\alpha\beta$0-reference frame can be deduced as

$$\begin{bmatrix}\dot{e}_\alpha\\ \dot{e}_\beta\end{bmatrix} = \begin{bmatrix}0 & -\omega_s\\ \omega_s & 0\end{bmatrix}\begin{bmatrix}e_\alpha\\ e_\beta\end{bmatrix}, \tag{3.57}$$

where $\omega_s = \frac{d\theta_k}{dt}$ given the fact that the back-EMF pulsates at slip frequency.

3.6.3.4 Dynamic equations of the stator side of the RDIFG in the $\alpha\beta$0-reference frame

Based on (3.55) and (3.57), the state space dynamic model of the stator side of the RDFIG can be written as

$$\begin{bmatrix}\dot{\mathbf{i}}\\ \dot{\mathbf{e}}\end{bmatrix} = \begin{bmatrix}\boldsymbol{A_{11}} & \boldsymbol{A_{12}}\\ 0 & \boldsymbol{A_{22}}\end{bmatrix}\begin{bmatrix}\mathbf{i}\\ \mathbf{e}\end{bmatrix} + \begin{bmatrix}\boldsymbol{B_{11}}\\ 0\end{bmatrix}\mathbf{v} \tag{3.58}$$

where $\mathbf{i} = \begin{bmatrix}i_{s\alpha} & i_{s\beta}\end{bmatrix}^T$, $\mathbf{e} = \begin{bmatrix}e_\alpha & e_\beta\end{bmatrix}^T$, $\mathbf{v} = \begin{bmatrix}v_{s\alpha} & v_{s\beta}\end{bmatrix}^T$ $\boldsymbol{A_{11}} = -\frac{R_s}{L_s}\mathbf{I} - \omega_r\mathbf{J}$, $\boldsymbol{A_{12}} = \frac{1}{L_s}\mathbf{I}$, $\boldsymbol{A_{22}} = \omega_s\mathbf{J}$ and $\boldsymbol{B_{11}} = \frac{1}{L_s}\mathbf{I}$, $\mathbf{J} = \begin{bmatrix}0 & -1\\ 1 & 0\end{bmatrix}$ and $\mathbf{I} = \begin{bmatrix}1 & 0\\ 0 & 1\end{bmatrix}$.

Stellenbosch University https://scholar.sun.ac.za

3.6.4 Power and electromagnetic torque equations

The stator active power, P_s, is given by

$$P_s = \frac{3}{2}(v_{sd}i_{sd} + v_{sq}i_{sq}) \tag{3.59}$$

The stator reactive power, Q_s, is given by

$$Q_s = \frac{3}{2}(v_{sq}i_{sd} - v_{sd}i_{sq}) \tag{3.60}$$

In the rotor side, the rotor active power, P_r, is given by

$$P_r = \frac{3}{2}(v_{rd}i_{rd} + v_{rq}i_{rq}) \tag{3.61}$$

and rotor reactive power are given by

$$Q_r = \frac{3}{2}(v_{rq}i_{rd} - v_{rd}i_{rq}) \tag{3.62}$$

The electromagnetic torque, τ_{em}, can be given by

$$\tau_{em} = 3P(\lambda_{rq}i_{rd} - \lambda_{rd}i_{rq}) \tag{3.63}$$

3.6.5 Mechanical equations

The relationship between the electromagnetic torque and the mechanical torque for the RDFIG can be expressed as

$$J\frac{d\Omega_m}{dt} + B\Omega_m = \tau_m - \tau_{em}, \tag{3.64}$$

where J is the inertia, Ω_m is the shaft angular speed, τ_m is the mechanical torque of the machine, τ_{em} is the electromagnetic torque, and, B is the friction coefficient.

3.7 L filter model

The schematic of a single-phase L filter is shown in Figure 3.11. The grid voltage dynamics into the $dq0$-reference frame, are given by

$$\begin{bmatrix} v_{gd} \\ v_{gq} \end{bmatrix} = \begin{bmatrix} R_f & 0 \\ 0 & R_f \end{bmatrix} \begin{bmatrix} i_{cd} \\ i_{cq} \end{bmatrix} + L_f \frac{d}{dt} \begin{bmatrix} i_{cd} \\ i_{cq} \end{bmatrix} + \begin{bmatrix} 0 & -\omega_g L_f \\ \omega_g L_f & 0 \end{bmatrix} \begin{bmatrix} i_{cd} \\ i_{cq} \end{bmatrix} + \begin{bmatrix} v_{cd} \\ v_{cq} \end{bmatrix}, \tag{3.65}$$

where v_{gd} and v_{gq} are the d-axis and q-axis grid voltages respectively; i_{cd} and i_{cq} are the d-axis and q-axis converter currents respectively; and, v_{cd} and v_{cq} are the d-axis and q-axis converter voltages respectively.

Stellenbosch University https://scholar.sun.ac.za

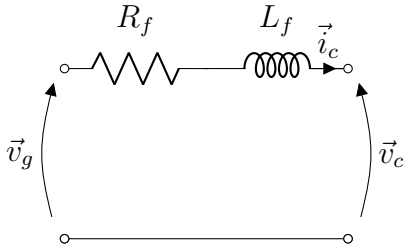

Figure 3.11: Schematic of the single-phase L filter.

Assuming that only the grid side converter (GSC) is the source of harmonic components in the system, Figure 3.11 becomes Figure 3.12 and the transfer function of the L filter, $H_l(\mathrm{p})$, becomes

$$H_l(\mathrm{p}) = \frac{i_c}{v_c} = \frac{1}{L_f \mathrm{p} + R_f}, \tag{3.66}$$

where $\mathrm{p} = j\omega_h$ and ω_h is the harmonic angular frequency.

Assuming that at high frequencies, $L_f^2\omega_h^2 >> R_f^2$, the filter attenuation becomes,

$$|H_l(j\omega_h)| \approx \frac{1}{\sqrt{L_f^2\omega_h^2}}, \tag{3.67}$$

where $|H_l(j\omega_h)|$ denotes the L filter attenuation.

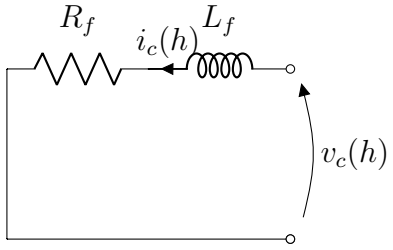

Figure 3.12: Schematic of the per-phase L filter at high frequency.

3.8 DC-link model

The modelling of the DC-link in this section is similar to that presented in [2, 123–125]. The energy stored in the capacitor of the DC-link, W_{dc}, as shown in Figure 3.13, is given by

$$W_{dc} = \frac{C_{dc}}{2} V_{dc}^2 \tag{3.68}$$

where V_{dc} is DC-link voltage, and C_{dc} is the DC-link capacitor. The dynamic behaviour of the DC-link voltage of the back-to-back power converter is given

Stellenbosch University https://scholar.sun.ac.za

by

$$C_{dc}\frac{dV_{dc}}{dt} = I_{dc}, \tag{3.69}$$

where I_{dc} is the current in the DC-link capacitor. Based on Figure 3.13, it can be seen that the current through the DC-link capacitor is given by

$$I_{dc} = I_c - I_s, \tag{3.70}$$

where I_s is the current into the stator side converter (SSC) while I_c is the current from the GSC, respectively.

Substituting (3.70) into (3.69) yields,

$$C_{dc}\frac{dV_{dc}}{dt} = I_c - I_s. \tag{3.71}$$

Multiplying (3.71) by V_{dc} with the assumption that the back-to-back converter is ideal, then,

$$C_{dc}V_{dc}\frac{dV_{dc}}{dt} = \frac{C_{dc}}{2}\frac{dV_{dc}^2}{dt} = P_c^{dc} - P_s^{dc}, \tag{3.72}$$

where $P_c^{dc} = V_{dc}I_c$ is the converter power on the DC side of the GSC; and $P_s^{dc} = V_{dc}I_s$ is the stator active power on the DC side of the SSC.

Substituting (3.68) into (3.72), yields,

$$\frac{dW_{dc}}{dt} = P_c^{dc} - P_s^{dc}. \tag{3.73}$$

Hence from (3.73), it can be seen that at steady state operating conditions the power through the SSC is equal to the power through the GSC, that is

$$P_c^{dc} = P_s^{dc}. \tag{3.74}$$

The converter active power at the AC side of the GSC is given by

$$P_c = \frac{3}{2}(v_{gd}i_{cd} + v_{gd}i_{cd}), \tag{3.75}$$

and, the converter reactive power at the AC side of the VSC is given by

$$Q_c = \frac{3}{2}(v_{gq}i_{cd} - v_{gd}i_{cq}). \tag{3.76}$$

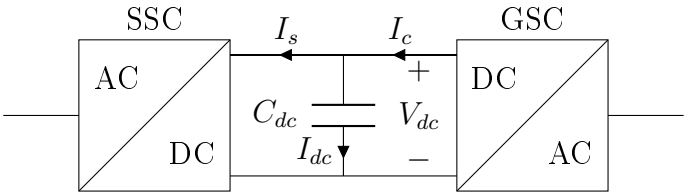

Figure 3.13: Schematic of the DC-link.

Stellenbosch University https://scholar.sun.ac.za

3.9 RDFIG vector control

The RDFIG vector control strategy consists of the stator side control strategy and the grid side control strategy. The cascaded structure in the synchronous reference frame is mostly used in both these control strategies. The vector control strategy for the RDFIG-based WECS was first proposed in [28]. In addition, an efficiency comparison between the conventional DFIG and the RDFIG at the same power rating was conducted in [28], as it was shown that the RDFIG has better efficiency. However, the experimental results were based on a conventional DFIG which is connected in stator-tied and rotor-tied configurations. In [32], a vector control strategy of a custom-designed RDFIG is proposed. The control strategy aims at the regulation of the electromagnetic torque using the q-axis stator current. It is obvious that sensor-less control of the RDFIG could be beneficial in improving its reliability when realized. In both [28, 32], the authors used the voltage-oriented control technique in order to implement the vector control. A synchronous reference frame (SRF)-PLL is used for the calculation of the angle of the rotor voltage space vector.

3.9.1 Vector control of the stator side converter

The basic schematic of the vector control strategy of the stator side converter for the grid-connected RDFIG system is shown in Figure 3.14. The vector control strategy of the stator side converter is developed in the synchronous $dq0$-reference frame, along either the rotor flux linkage space vector or the rotor voltage space vector. The stator current is usually used as a control variable in order to regulate the machine quantities. With the alignment of the d-axis synchronous reference frame along the rotor flux linkage space vector, the electromagnetic torque, the rotor active power, the rotor speed are all proportional to the q-axis stator current while the reactive rotor power is proportional to the d-axis stator current [2, 5, 32, 118].

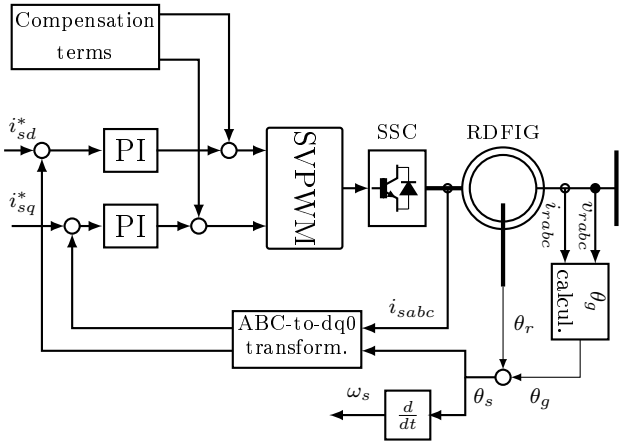

Figure 3.14: Schematic of a vector control of RDFIG system.

Stellenbosch University https://scholar.sun.ac.za

3.9.2 Vector control of the grid-side converter

The aim of the grid-side control strategy is maintain the DC-link voltage constant and guaranteeing a bi-directional power flow. Also, it aims at regulating the power factor with the reative power maintain at zero. The vector control technique is mostly adopted, with the $dq0$-reference frame aligned along the stator voltage space vector [2]. This alignment allows for the decoupled control of the active and reactive power. The control of the grid-side converter is similar to that of the voltage-source converter (VSC) [2]. The several vector control schemes of the VSC are proposed in [2, 123–125]. A cascaded structure was chosen. The aim of the inner control loops is to control the converter current while the aim of the outer control loop is to regulate the DC-link voltage. The single phase equivalent circuit of the grid side converter is presented in Figure 3.15.

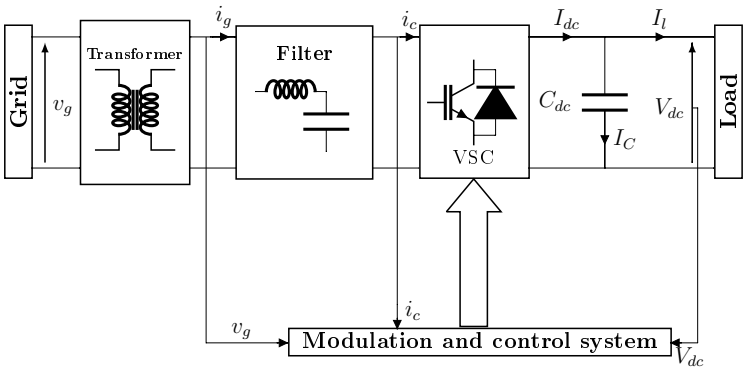

Figure 3.15: Schematic of the per-phase grid-connected VSC.

3.10 Speed/position estimation

In this section, the focus is on the speed/position estimator that is based on the association of the sliding mode observer and the phase-locked loop (PLL) estimator. In general, the second order sliding mode observer (SMO), is a closed loop observer which uses the discontinuous or continuous functions from the error between the real and estimated state variables as inputs. The system state reconstruction can be achieved by enforcing the sliding mode. The Lyapunov stability criteria is mostly used for the design of the sliding mode observer gains. The examples presented in this section are adapted from [1].

3.10.1 Sliding mode control

The basic principle of the sliding mode control consists of forcing the system trajectories to reach and stay, in a finite time, on a given sliding manifold in

Stellenbosch University https://scholar.sun.ac.za

the state space. The dynamics of any system can be described, in state space, by

$$\dot{\boldsymbol{x}} = \boldsymbol{f}(\boldsymbol{x}, \boldsymbol{t}) + \boldsymbol{g}(\boldsymbol{t}, \boldsymbol{x})\boldsymbol{u}(\boldsymbol{t}, \boldsymbol{x}), \tag{3.77}$$

where $(\dot{})$ denote the time derivative and $\boldsymbol{x} \in \mathbb{R}^n$ is the state variable, $\boldsymbol{f}(\boldsymbol{x}, \boldsymbol{t}) \in \mathbb{R}^n$, $\boldsymbol{g}(\boldsymbol{t}, \boldsymbol{x}) \in \mathbb{R}^{n \times m}$ and $\boldsymbol{u}(\boldsymbol{t}, \boldsymbol{x}) \in \mathbb{R}^m$ are sufficiently smooth vector fields. The sliding surface is defined by the vanishing corresponding sliding variable, $\boldsymbol{S}(\boldsymbol{x}) \in \mathbb{R}^m$, and its successive time derivatives. To this end, the control $u_i(t, x)$ is defined by

$$u_i(t, x) = \begin{cases} B, & \text{if } S_i(x) > B \\ S_i(x), & \text{if } S_i(x) \leq B \\ -B, & \text{if } S_i(x) < -B \end{cases}, \tag{3.78}$$

where $i = 1, ..., m$, B is th width of the boundary layer and the sliding mode control function, $\boldsymbol{u}(\boldsymbol{t}, \boldsymbol{x}) = [u_1(t, x), u_2(t, x), ..., u_m(t, x)]^T$. The existence of the sliding mode is equivalent to the condition of stability of motion on the subspaces, $\boldsymbol{S}(\boldsymbol{x}) = [S_1, S_2, ..., S_m]^T$ [50–52]. Hence, the Lyapunov stability theory can be used in order to guarantee the existence of the sliding mode.

3.10.2 Sliding mode observer design

The sliding mode observer (SMO), is a closed loop observer which uses the discontinuous or continuous functions from the error between the real and estimated state variables. It was shown in (3.56) that the back-EMF includes the slip angle. Hence, by estimating the back-EMF, which is not measurable, the slip speed/angle can be extracted. Based on the dynamic model of the RDFIG shown in (3.55), the sliding mode observer is designed as [1],

$$\begin{bmatrix} \dot{\hat{i}}_{s\alpha} \\ \dot{\hat{i}}_{s\beta} \end{bmatrix} = -\frac{R_s}{L_s} \begin{bmatrix} \hat{i}_{s\alpha} \\ \hat{i}_{s\beta} \end{bmatrix} + \begin{bmatrix} 0 & \hat{\omega}_r \\ -\hat{\omega}_r & 0 \end{bmatrix} \begin{bmatrix} i_{s\alpha} \\ i_{s\beta} \end{bmatrix} + \frac{1}{L_s} \begin{bmatrix} Z_\alpha \\ Z_\beta \end{bmatrix} + \frac{1}{L_s} \begin{bmatrix} v^*_{s\alpha} \\ v^*_{s\beta} \end{bmatrix}, \tag{3.79}$$

where $(*)$ and $(\hat{})$ is the reference and the estimated values, respectively. Z_α and Z_β are the discontinuous or continuous functions (they can be the saturation, sigmoid or signum functions).

The signum function is described by

$$\text{sgn}(S_i(x)) = \begin{cases} 1 & \text{if } S_i(x) > 1 \\ S_i(x) & \text{if } S_i(x) \leq 1 \\ -1 & \text{if } S_i(x) < -1 \end{cases}, \tag{3.80}$$

where sgn denotes the signum function. The signum function holds the advantage of being simple to implement. However, its main disadvantage is the high noise in the estimated signal of the variable of interest. The continuous

Stellenbosch University https://scholar.sun.ac.za

functions such as the saturation or sigmoid functions were used to mitigate the high noise created by the discontinuous functions. In [53], sigmoid function is given by

$$F(S_i(x)) = \left[\frac{2}{1+e^{-cS_i(x)}}\right] - 1, \tag{3.81}$$

where $F(S_i(x))$ is the sigmoid function while c is the adjustable parameter. Compared to the signum function, the sigmoid function creates lesser noise. However, there is still noise in the estimated signal that needs to be addressed.

In [1], the signum function is chosen because of simplicity. Compared to (3.77), from (3.79), it can be seen that the state variables, x, are the α-axis and β-axis stator current while the sliding mode control functions, $u(x,t)$, is Z_α and Z_β. The sliding mode control functions are given by

$$\begin{bmatrix} Z_\alpha \\ Z_\beta \end{bmatrix} = n \begin{bmatrix} \text{sgn}(i_{s\alpha} - \hat{i}_{s\alpha}) \\ \text{sgn}(i_{s\beta} - \hat{i}_{s\beta}) \end{bmatrix}, \tag{3.82}$$

where n is the gain of the sliding mode observer. The error of the estimated stator current is deduced by subtracting (3.79) from (3.55), yielding,

$$\begin{bmatrix} \dot{\tilde{i}}_{s\alpha} \\ \dot{\tilde{i}}_{s\beta} \end{bmatrix} = -\frac{R_s}{L_s} \begin{bmatrix} \tilde{i}_{s\alpha} \\ \tilde{i}_{s\beta} \end{bmatrix} + \begin{bmatrix} 0 & \tilde{\omega}_r \\ -\tilde{\omega}_r & 0 \end{bmatrix} \begin{bmatrix} i_{s\alpha} \\ i_{s\beta} \end{bmatrix} + \frac{1}{L_s} \begin{bmatrix} e_\alpha - Z_\alpha \\ e_\beta - Z_\beta \end{bmatrix}, \tag{3.83}$$

where $(\tilde{\ })$ is the difference between the actual and the estimated values. The reference stator voltage space vector from the control strategy is assumed to be equal to the actual stator voltage space vector. The stator current error and its time derivative have to be driven to zero in order to have accurate estimation. Hence, the predefined sliding surface, on which the system trajectory of the sliding mode observer will be forced to reach and stay at a finite time, is given by

$$\begin{bmatrix} \boldsymbol{S}(\boldsymbol{x}) \\ \dot{\boldsymbol{S}}(\boldsymbol{x}) \end{bmatrix} = \begin{bmatrix} 0 \\ 0 \end{bmatrix}. \tag{3.84}$$

Here $\boldsymbol{x} = [\hat{i}_{s\alpha} \quad \hat{i}_{s\beta}]^T$ represents the state variables (α-axis and β-axis stator currents). $\boldsymbol{S}(\boldsymbol{x}) = [i_{s\alpha} - \hat{i}_{s\alpha} \quad i_{s\beta} - \hat{i}_{s\beta}]^T$ is the sliding surface. One of the advantages of using the sliding mode observer is that its convergence rate can be tuned [19]. The Lyapunov stability theory is therefore used in order to guarantee the existence of the sliding motion and the Lyapunov stability theory is discussed in the following section.

3.10.3 Lyapunov stability criteria

The Lyapunov stability criteria is given by

$$\begin{cases} V(x) > 0 \\ \dot{V}(x) < 0 \end{cases}. \tag{3.85}$$

Stellenbosch University https://scholar.sun.ac.za

In [1], the Lyapunov function candidate is based on the stator current error. The Lyapunov function candidate is constructed as

$$V(x) = \frac{1}{2}\boldsymbol{S}(\boldsymbol{x})^T\boldsymbol{S}(\boldsymbol{x}) = \frac{1}{2}(\tilde{i}_{s\beta}^2 + \tilde{i}_{s\alpha}^2). \tag{3.86}$$

The time derivative of $V(x)$ is given by

$$\dot{V}(x) = -\frac{R_s}{L_s}(\tilde{i}_{s\beta}^2+\tilde{i}_{s\alpha}^2)+\tilde{i}_{s\alpha}[\frac{1}{L_s}e_\alpha+\tilde{\omega}_r i_{s\beta}]-\frac{n}{L_s}|\tilde{i}_{s\alpha}|+\dot{\tilde{i}}_{s\beta}[\frac{1}{L_s}e_\beta-\tilde{\omega}_r i_{s\alpha}]-\frac{n}{L_s}|\dot{\tilde{i}}_{s\beta}|. \tag{3.87}$$

It can be seen that (3.86) will always be positive. Therefore the first Lyapunov stability criteria is satisfied. In (3.87), the first term will always be negative. Then, n should be large enough in order to guarantee the existence of the sliding mode, that is ,

$$n > \begin{cases} |e_\alpha + L_s\tilde{\omega}_r i_{s\beta}| \\ |e_\beta - L_s\tilde{\omega}_r \tilde{i}_{s\alpha}| \end{cases}. \tag{3.88}$$

Therefore, $\tilde{i}_{s\alpha}$ and $\dot{\tilde{i}}_{s\alpha}$ are controlled to zero. However, the convergence rate of the sliding mode observer is dependant to how large n is. Based on the rated parameters of the RDFIG (rotor speed, stator current and back-EMF), if n is very large, then there is rapid convergence, but, as n increases the chattering effect also increases. So, there is a trade-off between a rapid convergence rate and the chattering effect. If the estimated rotor speed, $\hat{\omega}_r$, is accurate enough when the sliding motion occurs, then from (3.83), the estimated back-EMF becomes,

$$\begin{bmatrix}\hat{e}_\alpha \\ \hat{e}_\beta\end{bmatrix} \approx \begin{bmatrix}Z_\alpha \\ Z_\beta\end{bmatrix}. \tag{3.89}$$

Since the back-EMF is not measurable and that the back-EMF includes the slip angle as it is shown in (3.56), a phase locked loop (PLL) estimator can be used for the extraction of the slip angle/speed. The background for the design of the PLL estimator is presented in the following section.

3.10.4 Phase locked loop (PLL) estimator

The PLL estimator inputs the switching functions of the sliding mode observer in order to determine the input error to the PI controller. The error is determined using the trigonometric relationship of the tacking angle and the estimated angle. For example, in [1], the switching functions are multiplied by the cosine and sine functions of the tracking angle in order to construct a sine function of the estimated angle $\bar{\theta}_k = \bar{\theta}_s + \bar{\phi}_k$. So, multiplying the expression of the α-axis back-EMF in (3.56) by the cosine added with the multiplication of the sine of the tracking angle by the β-axis back-EMF in (3.56) yields

$$\epsilon = \frac{L_m|\vec{i}_r^{\,\text{sl}}|\omega_g}{\sqrt{e_\alpha^2+e_\beta^2}}\big(\sin\hat{\theta}_k\cos\bar{\theta}_k - \cos\hat{\theta}_k\sin\bar{\theta}_k\big) = \sin(\hat{\theta}_k - \bar{\theta}_k), \tag{3.90}$$

Stellenbosch University https://scholar.sun.ac.za

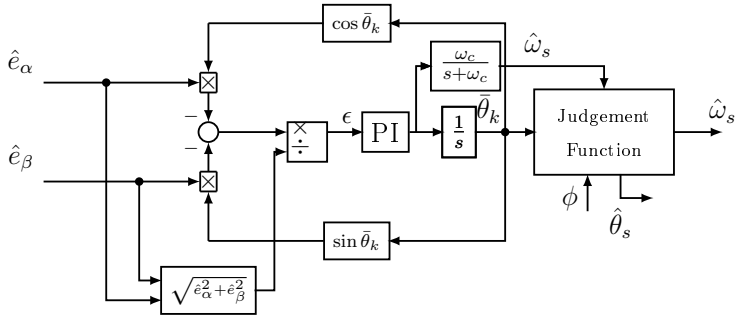

Figure 3.16: Schematic of the PLL estimator [1].

where, ϵ is the tracking error. The resulting sine function is composed of the difference between the estimated angle of the back-EMF and the tracking angle $\bar{\theta}_k$. When the error, ϵ, between the estimated angle and the tracking angle is very small the tracking error becomes,

$$\epsilon \approx \hat{\theta}_k - \bar{\theta}_k. \tag{3.91}$$

The tracking error is then driven to zero using a PI controller. The output of the PI controller is filtered using a simple low pass filter in order to provide the slip speed signal. Also, the output of the PI controller is integrated in order to obtain the tracking angle. It is important to note this the PLL estimator could only work properly in sub-synchronous operating conditions because of the change in sign of the slip angle. In fact, the tracking error is based on a sine function. This implies that there could be a phase shift of π when the tracking angle is negative [1]. In addition, in [1], a judgment function is proposed in order to eliminate the phase shift of π. This allows the improvement of the accuracy of the PLL estimator even in the super-synchronous operating conditions. The proposed judgement function is given by

$$\hat{\theta}_s = \begin{cases} \bar{\theta}_k - \bar{\phi}, & \hat{\omega}_s \geq 0 \\ \bar{\theta}_k - \bar{\phi} - \pi, & \hat{\omega}_s < 0 \end{cases}, \tag{3.92}$$

where ϵ and $\bar{\theta}_k = \bar{\theta}_s + \bar{\phi}$ are the error to be submitted to PI controller of the PLL estimator and the tracking angle of the outputs of the sliding mode control functions. Equation (3.92) helps in achieving better performances under all the operating conditions. The proposed PLL estimator is depicted in Figure 3.16. In Figure 3.16, the bandwidth of the filter, ω_c, can be chosen at about 100 Hz.

3.11 Summary

In this chapter, the modelling of the RDFIG-based WECSs on which the design of the sensor-less control strategy is based, is presented. In addition, the theoretical background on the slip speed estimator is presented.

Stellenbosch University https://scholar.sun.ac.za

Chapter 4

Sensor-less vector control of the RDIFG-based WECS

4.1 Introduction

In the previous Chapter, the modelling of the RDFIG-based WECS is provided. The design of the proposed sensor-less control strategy for RDFIG-based WECSs is provided in this Chapter.

4.2 Proposed sensor-less control strategy

The proposed sensor-less control strategy of the RDFIG systems consists of the stator-side converter control strategy and the grid-side converter control strategy. The proposed control strategy is presented in Figure 4.1. For both stator side and grid side control strategies, a cascaded structure with PI controllers is adopted, as shown in Figure 4.1.

4.2.1 Stator side control strategy

In the stator side control strategy, the rotor voltage-oriented control (VOC) technique is used. It is composed of the outer and inner control loops. The inner control loops are dedicated to the control of the d-axis and q-axis stator currents. The outer control loops are dedicated to the regulation of the rotor active and reactive stator powers. All quantities from the stator side in the abc-reference frame are transformed into the synchronous $dq0$-reference frame using the estimated slip angle, $\hat{\theta}_s$, from the proposed slip speed estimators discussed in Chapter 5. θ_g is calculated using a standard synchronous reference frame phase-locked loop (SRF-PLL) which is discussed in Section 4.5. The estimated slip angular speed, $\hat{\omega}_s$, is also used for the calculation of the compensation terms. In the outer control loops, either the active and reactive powers are

Stellenbosch University https://scholar.sun.ac.za

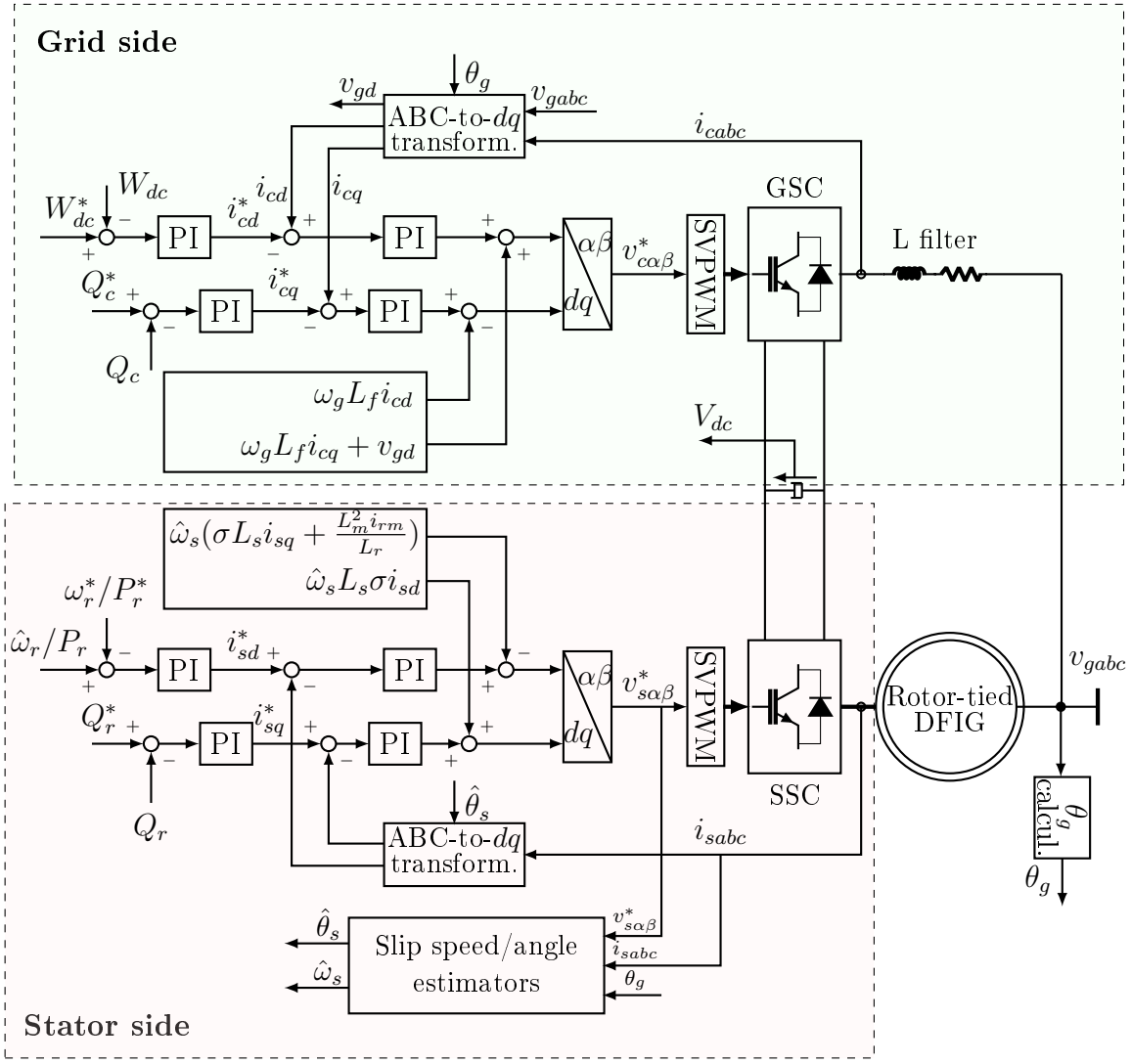

Figure 4.1: Schematic of the proposed sensor-less control strategy.

regulated using two PI controllers or the speed control is regulated using a PI controller with the reactive rotor power set to zero.

4.2.1.1 Rotor active and reactive powers control loops

Assuming that the power control is adopted, the reference active power is compared to the calculated rotor active to provide the error rotor active power. The rotor active power error is input to the outer PI controller. A similar approach is followed for the control of the reactive power.

4.2.1.2 Stator current control loops

In Figure 4.1, the outputs of the PI controllers from the outer control loops, for the rotor active and reactive powers, are the reference d-axis and q-axis

Stellenbosch University https://scholar.sun.ac.za

stator currents, respectively (i_{sd}^* and i_{sq}^*). The reference d-axis and q-axis stator currents are evaluated against the measured d-axis and q-axis stator currents in order to provide the error to be input to the respective inner PI controllers. The outputs of the inner control loops are associated with the compensation terms in order to provide the d-axis and q-axis stator voltages in the synchronous $dq0$-reference frame. Then, the d-axis and q-axis stator voltages are transformed into the stationary $\alpha\beta0$-reference frame, and then become the inputs to the SV-PWM function in order to provide actuating signals to the power switches of the stator side converter. The implementation of the SV-PWM function is presented in Appendix A.6.

4.2.1.3 Rotor angular speed control loop

If speed control is adopted, the reference rotor angular speed, ω_r^*, is compared to the estimated rotor angular speed, $\hat{\omega}_r = \hat{\omega}_s - \omega_g$ that is estimated from the slip speed estimator. The rotor reactive power is set to zero. Hence, only one PI controller is used. The output of the PI controller from the outer control loop for the rotor angular speed control is the reference d-axis stator current (i_{sd}^*). The reference q-axis stator current (i_{sq}^*) is set to zero. A similar strategy is followed for the inner control loops as that of the rotor active and reactive power control loops.

4.2.2 Grid side control strategy

The grid side control strategy also uses a cascaded structure, as shown in Figure 4.1. It can be seen that the grid side control strategy consists of the inner control loops and the outer control loops. The proposed grid-side control strategy uses the VOC technique. The outer control loops are dedicated to the indirect regulation of the DC-link voltage in order to allow a bidirectional power flow. The regulation of the DC-link voltage is done indirectly. Instead, the energy stored in the DC-link capacitor is controlled. Also, the outer control loops aims at regulating the converter reactive power. The inner control loops are dedicated to the control of the d-axis and q-axis converter currents. All quantities from the stator side in the abc reference frame are transformed into the synchronous $dq0$-reference frame using the grid angle, θ_g.

4.2.2.1 Outer control loops

From Figure 4.1, the energy stored in the DC-link capacitor and the converter reactive power are regulated using two PI controllers. The reference DC-link voltage, V_{dc}^*, is set according to the operating range of the power converter to be used. Then, the reference energy, W_{dc}^*, is calculated using (3.68). The same applies for the measured DC-link voltage, V_{dc}, in order to calculate the stored energy, W_{dc}. The stored energy error is then fed to an outer PI controller.

Stellenbosch University https://scholar.sun.ac.za

The reference reactive power, Q_c^*, is set to zero in order to reduce the amount of current going through the GSC. The measured converter reactive power, Q_c^*, is calculated using (3.76). The measured DC-link voltage compared with the reference DC-link voltage provides the error to be input to the outer PI controller.

4.2.2.2 Inner control loop

In Figure 4.1, the outputs of the outer PI controllers provide the reference d-axis and q-axis converter currents. The outputs of the inner PI controllers added to the compensation terms provide the reference d-axis and q-axis converter voltages. The reference d-axis and q-axis converter voltages are then transformed into the stationary $\alpha\beta 0$-reference frame, and input to the SV-PWM function in order to provide actuating signals to the power switches of the grid side converter.

4.3 Design of the stator side control strategy

The stator-side control strategy aims at controlling either the rotor active and reactive powers or the rotor angular speed of the RDFIG system. The proposed control strategy uses the voltage oriented control (VOC) technique. The phasor diagram of the VOC technique is depicted in Figure 4.2. Note the fact that, $\vec{v}_g$, is aligned to the d-axis of the synchronous reference frame. This control technique allows for the decoupled control of the active and reactive powers.

4.3.1 Inner current control loops

The functions of the inner current control loops are to regulate the d-axis and q-axis stator currents using the PI controllers in the synchronous $dq0$-reference frame. Based on (3.33), the rotor voltage space vector into the synchronous

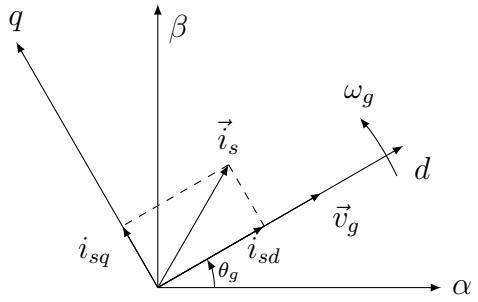

Figure 4.2: VOC scheme.

Stellenbosch University https://scholar.sun.ac.za

$dq0$-reference are given by

$$\begin{bmatrix} v_{rd} \\ v_{rq} \end{bmatrix} = \begin{bmatrix} R_r & 0 \\ 0 & R_r \end{bmatrix} \begin{bmatrix} i_{rd} \\ i_{rq} \end{bmatrix} + \frac{d}{dt} \begin{bmatrix} \lambda_{rd} \\ \lambda_{rq} \end{bmatrix} + \begin{bmatrix} 0 & -\omega_g \\ \omega_g & 0 \end{bmatrix} \begin{bmatrix} \lambda_{rd} \\ \lambda_{rq} \end{bmatrix}, \tag{4.1}$$

where v_{rd} and v_{rq} are the d-axis and q-axis rotor voltages, respectively; i_{rd} and i_{rq} are the d-axis and q-axis rotor current, respectively; λ_{rd} and λ_{rq} are the d-axis and q-axis stator flux linkages, respectively; and ω_g is the grid angular speed. It is assumed that the RDFIG is connected to the grid. Applying the VOC technique (or aligning the d-axis reference frame along the grid voltage space vector) yields

$$\begin{bmatrix} v_{rd} \\ v_{rq} \end{bmatrix} = \begin{bmatrix} |\vec{v}_g| \\ 0 \end{bmatrix} = \begin{bmatrix} v_{gd} \\ 0 \end{bmatrix}, \tag{4.2}$$

where v_{gd} is the d-axis grid voltage. The change in time of the rotor flux linkage space vector is negligible (or the RDFIG operates in steady state operating conditions) because the RDFIG is connected to a strong grid (infinite bus). Furthermore, the rotor resistance, R_r, is negligible and applying the voltage-oriented control technique to (4.1) yields

$$\begin{bmatrix} v_{rd} \\ \lambda_{rd} \end{bmatrix} \approx \begin{bmatrix} -\omega_g \lambda_{rq} \\ 0 \end{bmatrix}. \tag{4.3}$$

Based on (3.36), the stator space vector of a RDFIG in the synchronous $dq0$-reference is given by

$$\begin{bmatrix} v_{sd} \\ v_{sq} \end{bmatrix} = \begin{bmatrix} R_s & 0 \\ 0 & R_s \end{bmatrix} \begin{bmatrix} i_{sd} \\ i_{sq} \end{bmatrix} + \frac{d}{dt} \begin{bmatrix} \lambda_{sd} \\ \lambda_{sq} \end{bmatrix} + \begin{bmatrix} 0 & -\omega_s \\ \omega_s & 0 \end{bmatrix} \begin{bmatrix} \lambda_{sd} \\ \lambda_{sq} \end{bmatrix}, \tag{4.4}$$

where v_{sd} and v_{sd} are the d-axis and q-axis stator voltages, respectively; i_{sd} and i_{sq} are the d-axis and q-axis stator currents, respectively; λ_{sd} and λ_{sq} are the d-axis and q-axis rotor flux linkages, respectively; and, ω_s is the slip angular speed.

Based on (3.43) and (3.44), the rotor flux linkage space vector transformed into the synchronous $dq0$-reference frame is given by

$$\lambda_{rd} = L_r i_{rd} + L_m i_{sd} \tag{4.5}$$

and

$$\lambda_{rq} = L_r i_{rq} + L_m i_{sq} = L_m i_{rm}. \tag{4.6}$$

In (4.5), i_{rm} is the magnetising rotor current. Substituting (4.3) into (4.5) yields

$$i_{rd} = -\frac{L_m}{L_r} i_{sd}. \tag{4.7}$$

Based on (3.41) and (3.42), the stator flux linkage referred the synchronous $dq0$-reference is given by

$$\lambda_{sd} = L_s i_{sd} + L_m i_{rd} \tag{4.8}$$

Stellenbosch University https://scholar.sun.ac.za

and

$$\lambda_{sq} = L_s i_{sq} + L_m i_{rq}. \tag{4.9}$$

Substituting (4.7) into (4.8) yields

$$\lambda_{sd} = \sigma L_s i_{sd}, \tag{4.10}$$

where $\sigma = 1 - \frac{L_m^2}{L_s L_r}$ is a constant. Substituting (4.3) into (4.6) yields

$$i_{rq} = \frac{L_m}{L_r}(i_{rm} - i_{sq}), \tag{4.11}$$

where i_{rm} is assumed to be constant since the RDFIG is connected to the grid. Substituting (4.11) into (4.9) yields

$$\lambda_{sq} = \sigma L_s i_{sq} + \frac{L_m^2}{L_r} i_{rm}. \tag{4.12}$$

Substituting (4.10) and (4.12) into (4.4) together with replacing $\frac{d}{dt}$ with the Laplace operator, p, yields

$$\begin{bmatrix} v_{sd} \\ v_{sq} \end{bmatrix} = \underbrace{\begin{bmatrix} R_s + \sigma L_s \mathrm{p} & 0 \\ 0 & R_s + \sigma L_s \mathrm{p} \end{bmatrix} \begin{bmatrix} i_{sd} \\ i_{sq} \end{bmatrix}}_{\text{Plant}} + \underbrace{\hat{\omega}_s \begin{bmatrix} -\sigma L_s i_{sq} - \frac{L_m^2}{L_r} i_{rm} \\ \sigma L_s i_{sd} \end{bmatrix}}_{\text{compensation terms}}, \tag{4.13}$$

From (4.13), the plant and compensation terms can be deduced as indicated.

4.3.1.1 Inner PI gains design

The PI controller transfer function is given by

$$\mathrm{PI(p)} = \frac{K_{pi}(1 + T_{ii}\mathrm{p})}{T_{ii}\mathrm{p}}, \tag{4.14}$$

where K_{pi} and T_{ii} are the proportional gain and the integral time constant of the inner current control loop, respectively.

Based on (4.13), the transfer function of the plant is given by

$$\frac{i_{sdq}}{v_{sdq}} = \frac{K_{rl}}{1 + \mathrm{p}T_{rl}}, \tag{4.15}$$

where $K_{rl} = \frac{1}{R_s}$, $T_{rl} = \frac{\sigma L_s}{R_s}$ and the subscript, dq, denotes to both the d-axis and q-axis quantities. The delay introduced by the inverter is taken into consideration using the switching time. Based on Figure 4.3, the open loop transfer function is given by

$$H_{oi}(\mathrm{p}) = \frac{K_{pi}(1 + T_{ii}\mathrm{p})K_{\mathrm{pwm}}K_{rl}}{T_{ii}\mathrm{p}(1 + \mathrm{p}T_s)(1 + \mathrm{p}T_{rl})}, \tag{4.16}$$

Stellenbosch University https://scholar.sun.ac.za

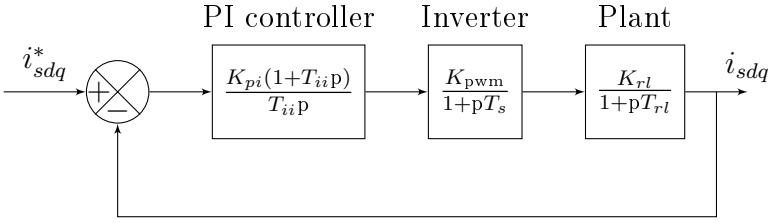

Figure 4.3: Block diagram of the inner stator current loop.

where $H_{oi}(\mathrm{p})$ is the open loop transfer function of the inner current control loop, where T_s is the sampling time and $K_{\mathrm{pwm}} = 1$. Using the Modulus Optimum tuning method for the open loop transfer function as shown in [123], the parameters of the PI controller are given by

$$T_{ii} = T_{rl} \tag{4.17}$$

and

$$K_{pi} = \frac{T_{rl}}{K_{rl}T_s}. \tag{4.18}$$

Substituting (4.17) and (4.18) into (4.16) yields that the closed loop transfer function is given by

$$H_{ci}(\mathrm{p}) = \frac{H_{oi}(\mathrm{p})}{1 + H_{oi}(\mathrm{p})} = \frac{1}{2T_s^2\mathrm{p}^2 + 2T_s\mathrm{p} + 1}. \tag{4.19}$$

In (4.19), given that the sampling time is very small, the first term of the denominator can be neglected ($T_s^2 \approx 0$). It follows that the closed loop transfer function of the inner current controller is given by

$$H_{ci}(\mathrm{p}) = \frac{1}{2T_s\mathrm{p} + 1}. \tag{4.20}$$

The closed loop transfer function of the inner current control loop is used in the design of the PI gains of the outer control loops.

4.3.2 Power control loops

The outer control loops are dedicated to the regulation of the rotor active and reactive powers. The reference generation of the rotor active power is done following an MPPT algorithm. In this thesis, the control technique is implemented in region II, as shown in Figure 4.4. Thus, no pitch control is activated. Based on (3.1), the reference rotor active power is the optimal mechanical power that can be extracted from the available wind power, that is

$$P_r^* = k_{opt}\hat{\omega}_r^3, \tag{4.21}$$

Stellenbosch University https://scholar.sun.ac.za

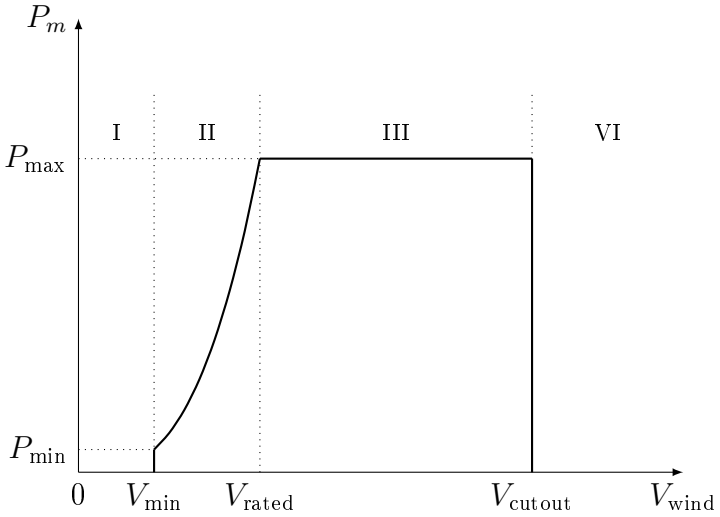

Figure 4.4: Mechanical power versus wind speed.

with

$$k_{opt} = \frac{1}{2}\rho_{\text{air}}\pi\frac{r^5 C_{pmax}(\varsigma,\beta)}{P^3\varsigma_{opt}^3 m^3}, \tag{4.22}$$

where $C_{pmax}(\varsigma,\beta)$ is the maximum power coefficient obtained at optimal tip-speed ratio ς_{opt}; ρ_{air} is the air density; r represents the turbine propeller radius; and, P and m are the pole-pairs and the gearbox ratio, respectively.

The estimated angular rotor speed is given by

$$\hat{\omega}_r = \hat{\omega}_s - \omega_g, \tag{4.23}$$

where $\hat{\omega}_s$ is obtained from the slip speed estimators to be addressed in Chapter 5, while ω_g is the grid angular speed. Based on (3.61), the rotor active power in the synchronous $dq0$-reference frame is given by

$$P_r = 3\big(v_{rd}i_{rd} + v_{rq}i_{rq}\big). \tag{4.24}$$

Substituting (4.2) and (4.7) into (4.24) yields

$$P_r = \underbrace{-3\frac{L_m}{L_r}v_{rd}}_{\text{plant}}\, i_{sd}. \tag{4.25}$$

It can be seen from (4.25) that the rotor active power can be controlled using the d-axis stator current.

On the other hand, the reference stator reactive power is deduced using the set rotor power factor. Hence the reference rotor reactive power is given by

$$Q_r^* = \frac{\sqrt{1-\cos^2\psi}}{\cos\psi}P_r^*, \tag{4.26}$$

Stellenbosch University https://scholar.sun.ac.za

where $\cos\psi$ is the rotor power factor. Based on (3.61), the rotor reactive power is given by

$$Q_r = 3\big(v_{rd}i_{rq} - v_{rq}i_{rd}\big). \tag{4.27}$$

Rewriting (4.6) in terms of the the q-axis stator current yields

$$i_{rq} = \frac{1}{L_r}\big(\lambda_{rq} - L_m i_{sq}\big). \tag{4.28}$$

Using the VOC technique, by substituting (4.2), (4.3) and (4.28) into (4.27), yields

$$Q_r = \underbrace{-3\frac{L_m}{L_r}v_{rd}}_{\text{plant}}\left(i_{sq} + \frac{v_{rd}}{\omega_g L_m}\right). \tag{4.29}$$

Based on (4.25) and (4.29), it can be seen that the rotor voltage-oriented control technique allows for the decoupled control of the rotor active and reactive powers. Also, it can be seen that the rotor reactive power can be regulated using the q-axis stator current while the rotor active power can be regulated using the d-axis stator current.

4.3.2.1 Outer PI gains design

From (4.25) and (4.29), the plant of the outer power control loop can be found to be

$$H_{pp}(\mathrm{p}) = \frac{P_r}{i_{rd}} = \frac{Q_r}{i_{rq}} = 3\frac{v_{rd}L_m}{L_r}. \tag{4.30}$$

The open loop transfer function is of the outer power control loops is given by

$$H_{op}(\mathrm{p}) = \frac{K_{pp}(1 + T_{ip}\mathrm{p})}{T_{ip}\mathrm{p}}\frac{1}{2T_s\mathrm{p} + 1}H_{pp}(\mathrm{p}). \tag{4.31}$$

Based on (4.31), the closed loop transfer function for the outer power control loops is presented in Figure 4.5. The similar technique used in Section 4.3.1 is also used for the tuning of parameters of the outer PI controller. However, the bandwidth of the outer control loop should at least be ten times slower than that of the inner control loops when designing the PI parameters in order to guarantee optimum control in the cascaded control structure.

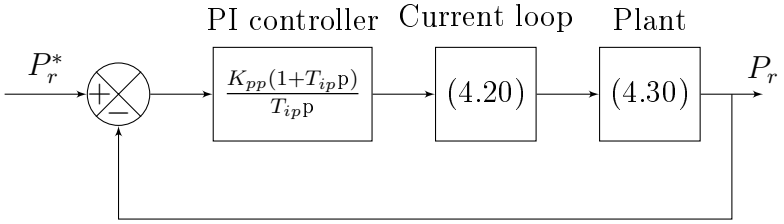

Figure 4.5: Block diagram of the outer power control loop.

Stellenbosch University https://scholar.sun.ac.za

4.3.3 Speed control loop

Based on (3.64) together with the assumption that the friction coefficient is negligible, the rotor angular speed is given by

$$J\frac{d\omega_r}{dt} = P(\tau_m - \tau_{em}), \tag{4.32}$$

where ω_r, τ_m and τ_{em} are the rotor angular speed, the mechanical torque and the electromechanical torque respectively; and, J and P are the inertia and the number of pole-pairs in the RDFIG, respectively. Based on (3.63), the electromagnetic torque is given by

$$\tau_{em} = 3P(\lambda_{rq}i_{rd} - \lambda_{rd}i_{rq}). \tag{4.33}$$

Substituting (4.33) into (4.32) yields

$$J\frac{d\omega_r}{dt} = P(\tau_m - 3P(\lambda_{rq}i_{rd} - \lambda_{rd}i_{rq})). \tag{4.34}$$

Substituting (4.3) into (4.34), yields

$$J\frac{d\omega_r}{dt} = P(\tau_m + 3P\frac{v_{rd}}{\omega_g}i_{rd}). \tag{4.35}$$

Substituting (4.7) into (4.35) and replacing the $\frac{d}{dt}$ by the Laplace operator, yields

$$\omega_r = \underbrace{\frac{-3v_{rd}L_mP^2}{\omega_g L_r J\mathrm{p}}}_{\text{plant}} i_{sd} + \underbrace{P\tau_m}_{\text{disturbance}}. \tag{4.36}$$

The transfer function of the plant for the outer speed control loop is given by

$$\frac{\omega_r}{i_{sd}} = \frac{K_\omega}{\mathrm{p}}, \tag{4.37}$$

where $K_\omega = \frac{3v_{rd}L_mP^2}{\omega_g L_r J}$.

4.3.3.1 Outer PI gains design

From Figure 4.6, the transfer function of the speed control loop is given by

$$H_{o\omega}(\mathrm{p}) = \frac{K_{p\omega}(1 + T_{i\omega}\mathrm{p})K_\omega}{T_{i\omega}\mathrm{p}(2T_s\mathrm{p} + 1)\mathrm{p}}. \tag{4.38}$$

Using the Symmetrical Optimum method, the PI controller of the outer speed control loop are given by

$$K_{p\omega} = \frac{1}{2aT_sK_\omega}, \tag{4.39}$$

and

$$T_{i\omega} = 2a^2T_s, \tag{4.40}$$

where $a = 2.4$ [123].

Stellenbosch University https://scholar.sun.ac.za

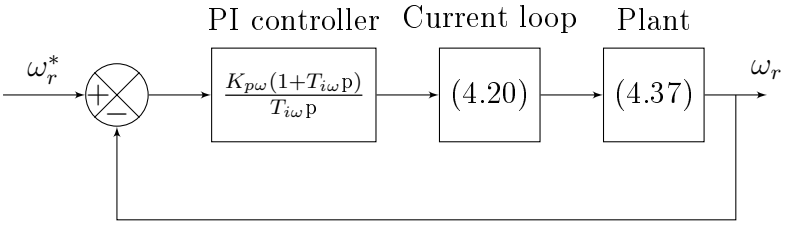

Figure 4.6: Block diagram of the outer speed loop.

4.4 Design of the grid side control strategy

In this control strategy, an L filter is used in order to filter the harmonics created by the switching components of the GSC. The DC-link voltage increases or decreases with the direction of the power flow. Hence, it is necessary to maintain the DC-link voltage constant to maximise the power flow and to allow for optimal operation of the RDFIG system. The DC-link voltage is controlled indirectly by controlling the energy stored in the DC-link capacitor. This approach has the advantage of eliminating the non-linearity in the expression of the DC-link voltage. A cascaded structure is adopted, as shown in Figure 4.1. The outer control loop is dedicated to the indirect regulation of the DC-link voltage while the inner control loop is dedicated to the regulation of the inner converter current.

4.4.1 Inner grid current control loop

Based on (3.65), the converter voltage equations into the synchronous $dq0$-reference frame are given by

$$\begin{bmatrix} v_{cd} \\ v_{cq} \end{bmatrix} = -\begin{bmatrix} R_f & 0 \\ 0 & R_f \end{bmatrix}\begin{bmatrix} i_{cd} \\ i_{cq} \end{bmatrix} - L_f\frac{d}{dt}\begin{bmatrix} i_{cd} \\ i_{cq} \end{bmatrix} + \begin{bmatrix} 0 & L_f\omega_g \\ -L_f\omega_g & 0 \end{bmatrix}\begin{bmatrix} i_{cd} \\ i_{cq} \end{bmatrix} + \begin{bmatrix} v_{gd} \\ 0 \end{bmatrix}, \tag{4.41}$$

where v_{cd} and v_{cq} are the d-axis and q-axis converter voltages, receptively; v_{gd} and $v_{gq} = 0$ are the d-axis and q-axis grid voltages, respectively; i_{cd} and i_{cq} are the d-axis and q-axis converter currents, respectively; and, R_f is the resistance of the L filter while L_f is the inductance of the L filter. Replacing $\frac{d}{dt}$ with the Laplace operator, p, yields that

$$\begin{bmatrix} v_{cd} \\ v_{cq} \end{bmatrix} = \underbrace{-\begin{bmatrix} R_f + L_f\mathrm{p} & 0 \\ 0 & R_f + L_f\mathrm{p} \end{bmatrix}\begin{bmatrix} i_{cd} \\ i_{cq} \end{bmatrix}}_{\text{plant}} + \underbrace{\begin{bmatrix} 0 & L_f\omega_g \\ -L_f\omega_g & 0 \end{bmatrix}\begin{bmatrix} i_{cd} \\ i_{cq} \end{bmatrix} + \begin{bmatrix} v_{gd} \\ 0 \end{bmatrix}}_{\text{compensation terms}}. \tag{4.42}$$

The transfer function of the plant is given by

$$\frac{v_{cdq}}{i_{cdq}} = \frac{\frac{1}{R_f}}{1 + \frac{L_f}{R_f}\mathrm{p}}. \tag{4.43}$$

Stellenbosch University https://scholar.sun.ac.za

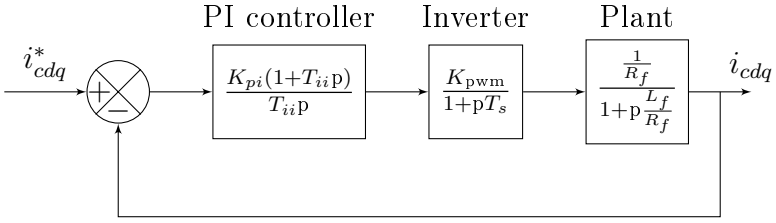

Figure 4.7: Block diagram of the inner converter current control loop.

The block diagram of the inner control loop is shown in Figure 4.7. Using the Optimum Modulus method as in Section 4.3.1, the parameters of the PI controllers are given by

$$T_{ii} = \frac{L_f}{R_f}, \tag{4.44}$$

and

$$K_{pi} = \frac{\frac{L_f}{R_f}}{\frac{1}{R_f}T_s}. \tag{4.45}$$

Using the designed parameters of the inner PI controller, the closed loop transfer function of the inner control loop is given by

$$H_{cl}(\mathrm{p}) = \frac{1}{2T_s\mathrm{p}+1}. \tag{4.46}$$

4.4.2 Outer control loops

The design of the energy control loop and that of the converter reactive power control loop is presented in this section.

4.4.2.1 Energy control loop

Based on (3.73), the power balance in the DC-link is given by

$$\frac{dW_{dc}}{dt} = P_c^{dc} - P_s^{dc}, \tag{4.47}$$

where W_{dc} is the energy in the DC-link; P_c^{dc} is the active converter power at the DC side of the GSC while P_s^{dc} is the stator active power at the DC side of the SSC. The active converter power at the DC side of the GSC is given by

$$P_c^{dc} = V_{dc}I_c, \tag{4.48}$$

where V_{dc} is the DC-link voltage while I_c is the DC converter current. Based on (3.75), the converter active power at the AC side is given by

$$P_c = 3(v_{gd}i_{cd} + v_{gq}i_{cq}), \tag{4.49}$$

Stellenbosch University https://scholar.sun.ac.za

where i_{cd} and i_{cq} are the d-axis and q-axis converter currents, respectively.

Assuming a lossless GSC, it yields that the converter active power at the AC side P_c is equal to the converter power at the DC side P_c^{dc}, that is

$$P_c = 3(v_{gd}i_{cd} + v_{gq}i_{cq}) = V_{dc}I_c. \tag{4.50}$$

Substituting (4.2) into (4.50) yields

$$P_c = 3v_{gd}i_{cd} = V_{dc}I_c. \tag{4.51}$$

Substituting (4.51) into (4.47), yields

$$\frac{dW_{dc}}{dt} = 3v_{gd}i_{cd} - P_s^{dc}. \tag{4.52}$$

Based on (4.52), the transfer function is given by

$$\frac{W_{dc}}{i_{cd}} = \frac{3v_{gd}}{\mathrm{p}}. \tag{4.53}$$

The power through the SSC is considered as a disturbance. The closed control loop is shown in Figure 4.8. The design of the parameters of the outer PI controller is conducted using the Symmetrical Optimum method. This implies that the proportional gain of the outer PI controller is given by

$$K_{pw} = \frac{1}{2aT_sK_w}, \tag{4.54}$$

where $K_w = 3v_{gd}$. Then, the integral time constant of the outer PI controller is given by

$$K_{pw} = 2a^2T_s. \tag{4.55}$$

where a=2.4 [123].

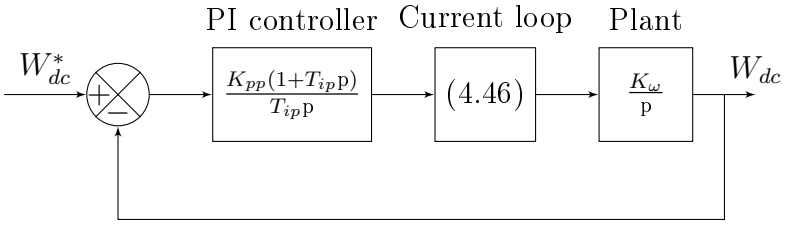

Figure 4.8: Block diagram of the DC-link voltage control loop.

Stellenbosch University https://scholar.sun.ac.za

4.4.2.2 Converter reactive power control loop

Based on (3.76), the converter reactive power is given by

$$Q_c = 3(v_{gq}i_{cd} - v_{gd}i_{cq}), \tag{4.56}$$

where Q_c is the converter reactive power. Substituting (4.2) into (4.56), yields

$$Q_c = \underbrace{-3v_{gd}}_{\text{plant}} i_{cq}. \tag{4.57}$$

From (4.57), it can be seen that the converter reactive power can be regulated using the q-axis converter current. Hence, the transfer function of the plant is given by

$$\frac{Q_c}{i_{cq}} = -3v_{gd}. \tag{4.58}$$

Hence by setting $i_{cq} = 0$, the GSC can be controller so that it operates at unity power factor. The design of the PI gains for the converter reactive power loop is the same as the approach that is discussed in Section 4.3.2.1.

4.5 Grid voltage angle calculation

The synchronous reference frame phase locked loop (SRF-PLL) is used to calculate the grid voltage angle. The grid voltage angle is necessary when the VOC technique is used. The SFR-PLL is largely discussed in [126]. Assume that the grid voltage space vector is given by

$$\vec{v}_g = |\vec{v}_g|e^{j\theta_g}, \tag{4.59}$$

where $\vec{v}_g$ is the grid voltage space vector; θ_g is the angle of the grid voltage; and, $|\vec{v}_g|$ is the magnitude of the grid voltage space vector. The phasor representation of grid voltage space vector is shown in Figure 4.9. Representing the grid voltage space vector into the synchronous $dq0$-reference frame as

$$\begin{bmatrix} v_{gd} \\ v_{gq} \end{bmatrix} = \begin{bmatrix} |\vec{v}_g|\cos(\theta_g - \theta_{dq}) \\ |\vec{v}_g|\sin(\theta_g - \theta_{dq}) \end{bmatrix}. \tag{4.60}$$

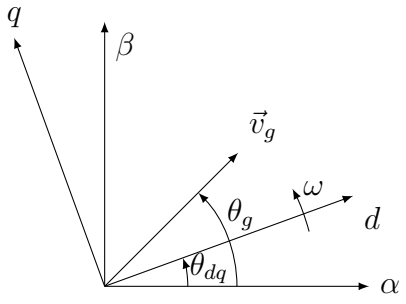

Figure 4.9: Phasor diagram of the grid voltage space vector.

Stellenbosch University https://scholar.sun.ac.za

A small approximation of (4.60) is

$$\begin{bmatrix} \delta v_{gd} \\ \delta v_{gq} \end{bmatrix} \approx \begin{bmatrix} |\vec{v}_g|(1 - \frac{\delta\theta^2}{2}) \\ |\vec{v}_g|(\delta\theta) \end{bmatrix}, \tag{4.61}$$

where $\delta\theta = \theta_g - \theta_{dq}$ is a small variation between the grid voltage angle and the angle of the synchronous $dq0$-reference frame. From (4.61), it can be seen that δv_{gq} is equal to zero when the grid voltage angle and the angle of the synchronous reference frame are the same ($\theta_g = \theta_{dq}$). Then, the synchronous $dq0$-reference frame is said to be aligned along grid voltage space vector. From (4.61), the small variation between the grid angular speed and the angular speed of the the synchronous $dq0$-reference frame is given by

$$\frac{\delta v_{gq}}{\delta t} = |\vec{v}_g|\omega, \tag{4.62}$$

where $\omega = \frac{\delta\theta}{\delta t}$. Equation (4.62) can be approximated as

$$\frac{dv_{gq}}{dt} = |\vec{v}_g|\omega. \tag{4.63}$$

From (4.63), the plant of the SFR-PLL is given by

$$\frac{v_{gq}}{\omega} = \frac{|\vec{v}_g|}{\mathrm{p}}. \tag{4.64}$$

From Figure 4.10, the open loop transfer function of the SRF-PLL is given by

$$H_{ol}(\mathrm{p}) = \Big(\frac{K_l(1 + \mathrm{p}T_l)}{\mathrm{p}T_l}\Big)\Big(\frac{1}{1 + \mathrm{p}T_s}\Big)\Big(\frac{|\vec{v}_g|}{\mathrm{p}}\Big), \tag{4.65}$$

where K_l and T_l are the proportional gain and the integral time constant of the PI controller. The parameters of the PI controller of the PLL are tuned using Symmetrical Optimum, as below [123];

$$T_l = a^2 T_s, \tag{4.66}$$

$$K_l = \frac{1}{a|\vec{v}_g|T_s}, \tag{4.67}$$

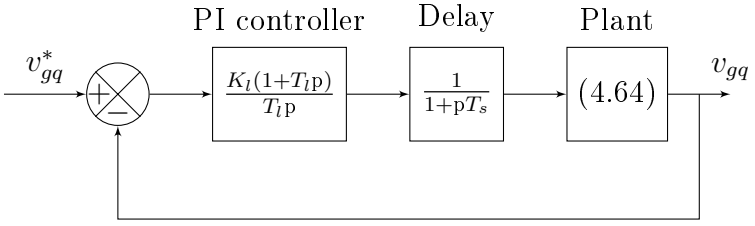

Figure 4.10: Block diagram of the SRF-PLL control loop.

Stellenbosch University https://scholar.sun.ac.za

and

$$\omega_c = \frac{1}{aT_s}. \tag{4.68}$$

In (4.68), ω_c is the cross-over frequency of the PI controller and a is the normalisation factor. It is advised that the cross-over frequency of the PI controller of the SRF-PLL should be close to the grid frequency [126]. The design of the PI controller should be done for a cross-over frequency value of $\omega_c \approx 314$ rad/s. The schematic of the SRF-PLL is presented in Figure 4.11.

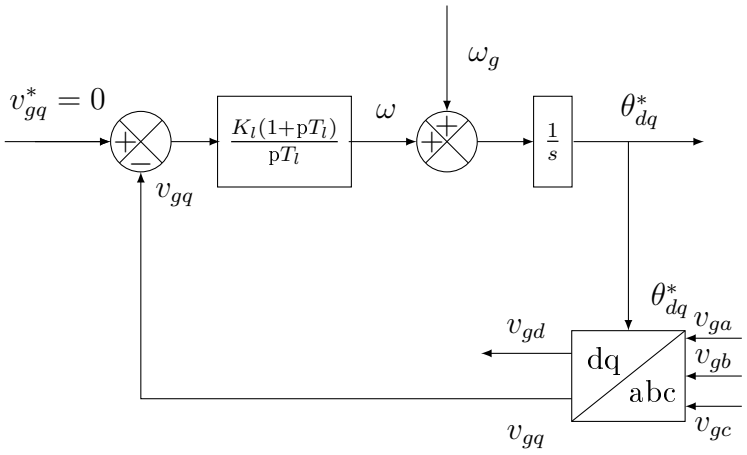

Figure 4.11: Schematic of the SRF-PLL.

4.6 Summary

In this Chapter, the proposed sensor-less control strategy for RDFIG-based WECS is discussed. The proposed control strategy consists of the stator side control strategy and the grid side control strategy. A cascaded structure is chosen. The voltage-oriented control technique is used. The design of the PI controllers is also discussed.

Stellenbosch University https://scholar.sun.ac.za

Chapter 5

Slip speed estimators for sensor-less control of RDFIGs

5.1 Introduction

In the previous Chapter, the sensor-less control of the RDFIG-based WECSs is provided. The sensor-less control strategy is implemented in the synchronous $dq0$-reference frame. It yields that the knowledge of the rotor angular speed, the slip angular speed and the slip angle are required. Hence, the slip speed estimators are discussed in this Chapter.

5.2 Second order sliding mode observer

In this section, the second order sliding mode observer (SMO) is presented. This section is adapted from [37].

5.2.1 Motivation

A performance analysis of the sensor-less vector control of the RDFIG systems is presented in [1]. The proposed sensor-less control strategy uses a slip speed/position estimator based on the association of the second order sliding mode observer and the PLL estimator. The proposed PLL estimator includes a judgement function in order to eliminate the phase shift of π that is introduced at super-synchronous operating conditions (when the slip speed is negative) [23,54]. Although, the proposed judgement function helps in avoiding the phase shift, around the transition from sub-synchronous to super-synchronous operating conditions, a large slip angle error can be seen. Hence, the slip speed estimator proposed in this section aims at eliminating the phase shift with known relationships between the slip speed and the rotor angular speed of the RDFIG system.

Stellenbosch University https://scholar.sun.ac.za

5.2.2 Design of the sliding mode observer

The SMO proposed in this section uses the stator current and the back-EMF of the RDFIG, as state variables. The estimation of the back-EMF can be done before the RDFIG is connected the load/grid. The proposed SMO uses the measured α-axis and β-axis stator currents ($i_{s\alpha}$ and $i_{s\beta}$) and the reference α-axis and β-axis stator voltages ($v^*_{s\alpha}$ and $v^*_{s\beta}$) as inputs. Based on the dynamic model of the RDFIG presented in (3.55), the proposed SMO is constructed as

$$\begin{bmatrix}\dot{\hat{i}}_{s\alpha}\\ \dot{\hat{i}}_{s\beta}\end{bmatrix} = \begin{bmatrix}-\frac{R_s}{L_s} & 0\\ 0 & -\frac{R_s}{L_s}\end{bmatrix}\begin{bmatrix}\hat{i}_{s\alpha}\\ \hat{i}_{s\beta}\end{bmatrix} + \frac{1}{L_s}\begin{bmatrix}v^*_{s\alpha}\\ v^*_{s\beta}\end{bmatrix} + \begin{bmatrix}0 & \hat{\omega}_r\\ -\hat{\omega}_r & 0\end{bmatrix}\begin{bmatrix}i_{s\alpha}\\ i_{s\beta}\end{bmatrix} + \begin{bmatrix}\frac{n_1}{L_s} & 0\\ 0 & \frac{n_2}{L_s}\end{bmatrix}\begin{bmatrix}Z_\alpha\\ Z_\beta\end{bmatrix} \tag{5.1}$$

where the superscript ($\dot{}$) denotes the derivative time of any quantity; $\hat{i}_{s\alpha}$ and $\hat{i}_{s\beta}$ are the estimated α-axis and β-axis stator currents, respectively; $i_{s\alpha}$ and $i_{s\beta}$ are the α-axis and β-axis stator currents, respectively; Z_α and Z_β are the sliding mode control functions; and, n_1 and n_2 are the sliding observer gains to be designed. L_s is the stator inductance. In this section the signum function is used. However, the signum function introduced a chattering effect on the estimated back-EMF space vector. It can also be noticed from (5.1) that the constructed sliding mode observer does not take into consideration the dynamics of the back EMF space vector.

Assume that the reference stator voltages ($v^*_{s\alpha}$ and $v^*_{s\beta}$) are equal to the measured stator voltages ($v_{s\alpha}$ and $v_{s\beta}$). Then, subtracting (3.55) from (5.1) yields,

$$\begin{bmatrix}\dot{\tilde{i}}_{s\alpha}\\ \dot{\tilde{i}}_{s\beta}\end{bmatrix} = -\frac{R_s}{L_s}\begin{bmatrix}\tilde{i}_{s\alpha}\\ \tilde{i}_{s\beta}\end{bmatrix} + \begin{bmatrix}0 & \tilde{\omega}_r\\ -\tilde{\omega}_r & 0\end{bmatrix}\begin{bmatrix}i_{s\alpha}\\ i_{s\beta}\end{bmatrix} + \frac{1}{L_s}\begin{bmatrix}e_\alpha\\ e_\beta\end{bmatrix} - \begin{bmatrix}\frac{n_1}{L_s} & 0\\ 0 & \frac{n_2}{L_s}\end{bmatrix}\begin{bmatrix}Z_\alpha\\ Z_\beta\end{bmatrix}, \tag{5.2}$$

where ($\tilde{}$) denotes the difference between the actual and the estimated quantities; and, e_α and e_β are the α-axis and β-axis back-EMFs, respectively. $\tilde{\omega}_r = \omega_r - \hat{\omega}_r$ is the rotor speed error. In the following section the design of the sliding gains is presented.

5.2.3 Stability analysis

From (3.86), the Lyapunov function for the proposed sliding mode observer is described as

$$V(x) = \frac{1}{2}(\tilde{i}^2_{s\beta} + \tilde{i}^2_{s\alpha}), \tag{5.3}$$

where $V(x)$ is the Lyapunov function. From (3.85), the Lyapunov stability criteria is fulfilled when

$$\begin{cases} V(x) > 0 \\ \dot{V}(x) < 0 \end{cases}. \tag{5.4}$$

Stellenbosch University https://scholar.sun.ac.za

On one hand, It can be seen that the chosen Lyapunov function $V(x)$ in (5.3) is strictly positive. Hence, the Lyapunov stability criteria is partly satisfied. As previously stated, the expression of the time derivative of the chosen Lyapunov function $\dot{V}(x)$ for the proposed sliding mode observer is given by (from (3.87))

$$\dot{V}(x) = -\frac{R_s}{L_s}(\tilde{i}_{s\beta}^2+\tilde{i}_{s\alpha}^2)+\tilde{i}_{s\alpha}[\frac{1}{L_s}e_\alpha+\tilde{\omega}_r i_{s\beta}]+\tilde{i}_{s\beta}[\frac{1}{L_s}e_\beta-\tilde{\omega}_r i_{s\alpha}]-\frac{n_2}{L_s}|\tilde{i}_{s\beta}|-\frac{n_1}{L_s}|\tilde{i}_{s\alpha}| \tag{5.5}$$

with

$$\begin{bmatrix} Z_\alpha \\ Z_\beta \end{bmatrix} = \begin{bmatrix} \text{sgn}(\tilde{i}_{s\alpha}) \\ \text{sgn}(\tilde{i}_{s\beta}) \end{bmatrix} \tag{5.6}$$

where sgn denotes the signum function. From (5.5), it can be seen that the first term will always be negative. Furthermore, n_1 and n_2 should be large enough to ensure that $\dot{V}(x)$ satisfies the Lyapunov stability criteria. Hence, at least (from (3.88))

$$\begin{bmatrix} n_1 \\ n_2 \end{bmatrix} > \begin{bmatrix} |e_\alpha + L_s\tilde{\omega}_r i_{\beta s}| \\ |e_\beta - L_s\tilde{\omega}_r i_{\alpha s}| \end{bmatrix}. \tag{5.7}$$

Once the Lyapunov stability criteria is fulfilled, the robustness and the convergence of the proposed SMO is ensured in a finite time. When $V(x)$ converges to zero it implies that $\tilde{i}_{s\alpha}$ and $\tilde{i}_{s\beta}$ are controlled to zero. Then, it can be seen from (5.2) that if the estimated speed is accurate enough, when the sliding motion occurs, the back-EMF can be estimated using the sliding control functions, that is,

$$\begin{bmatrix} \hat{e}_\alpha \\ \hat{e}_\alpha \end{bmatrix} \approx \begin{bmatrix} n_1 & 0 \\ 0 & n_2 \end{bmatrix} \begin{bmatrix} Z_\alpha \\ Z_\beta \end{bmatrix}, \tag{5.8}$$

where $\hat{e}_\alpha$ and $\hat{e}_\beta$ are the estimated α-axis and β-axis back EMFs, respectively. It was shown in (3.56), that the back-EMF includes the slip angle. Hence, through the estimation of the back-EMF, the estimated slip angle can be extracted.

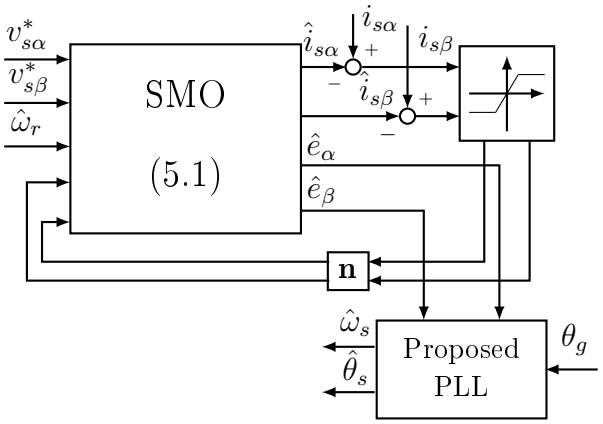

Figure 5.1: Schematic of the proposed SMO and the PLL estimator.

Stellenbosch University https://scholar.sun.ac.za

The estimated slip angle from the estimated back-EMF includes noise introduced by the sliding mode control functions (signum function). The noise is usually filtered by using a low pass filters (LPF) [16, 17]. However, the use of the LPFs can deteriorate the performance/accuracy of the estimated angle by introducing phase delays. Hence, a PLL estimator is proposed in order to enhance the estimation performance.

The well-known impacts of the non-linear effects on the estimated rotor position with the use of reference voltages are avoided by the use of the proposed PLL estimator. The proposed PLL estimator is discussed in Section 5.6. The schematic of the proposed sliding mode observer is portrayed in Figure 5.1.

5.3 Adaptive sliding mode observer

In this section, an adaptive sliding mode observer (ASMO) for sensor-less control of the RDFIG system is presented. The motivation for the proposition of the ASMO for the sensor-less control of the RDFIG system is presented together with the design of the ASMO are presented. The design of the adaptive control gains is discussed and the stability analysis of the ASMO are presented.

5.3.1 Motivation

Generally, the SMOs designed for sensor-less operations of RDFIG systems make use of constant control gains. This lead to undesirable chattering while the system trajectories have already reached the sliding surface. Further, The design of the sliding gains is complex because of the fact that it is difficult to measure the parameter variations of a system in practical applications. Also, the chattering effect due to the switching function of the sliding mode observer may be caused by the tuned gains [56]. Hence, an adaptive tune of the sliding gains is necessary to avoid the above-mentioned issues.

5.3.2 Design of the adaptive sliding mode observer

The proposed ASMO aims at estimating the back-EMF space vector. The proposed ASMO uses the α-axis and β-axis stator currents and the reference α-axis and β-axis stator voltages, as inputs. The design of the ASMO is conducted in such a way that a fast response with low chattering is guaranteed. In line with the expression of the RDFIG mathematical model shown in (3.55), the adaptive sliding mode observer is chosen as

$$\begin{bmatrix} \dot{\hat{i}}_{s\alpha} \\ \dot{\hat{i}}_{s\beta} \end{bmatrix} = \begin{bmatrix} -\frac{R_s}{L_s} & 0 \\ 0 & -\frac{R_s}{L_s} \end{bmatrix} \begin{bmatrix} \hat{i}_{s\alpha} \\ \hat{i}_{s\beta} \end{bmatrix} + \frac{1}{L_s} \begin{bmatrix} v^*_{s\alpha} \\ v^*_{s\beta} \end{bmatrix} + \begin{bmatrix} 0 & \hat{\omega}_r \\ -\hat{\omega}_r & 0 \end{bmatrix} \begin{bmatrix} i_{s\alpha} \\ i_{s\beta} \end{bmatrix} + \frac{K(t)}{L_s} \begin{bmatrix} \text{sgn}(S_\alpha) \\ \text{sgn}(S_\beta) \end{bmatrix} \tag{5.9}$$

Stellenbosch University https://scholar.sun.ac.za

where $K(t)$ denotes the adaptive gain, while (sgn) refers to the signum function; and,

$$\boldsymbol{S} = \begin{bmatrix} S_\alpha \\ S_\beta \end{bmatrix} = \begin{bmatrix} i_{s\alpha} - \hat{i}_{s\alpha} \\ i_{s\beta} - \hat{i}_{s\beta} \end{bmatrix}. \tag{5.10}$$

The design of the parameters of the adaptive law are based on the necessary and the sufficient conditions for the existence of the sliding surface. The sufficient condition consists of guaranteeing the reduction of the chattering effect and the gain overestimation together with improving the system response. The schematic of the ASMO is shown in Figure 5.2. The dynamics of the stator current errors is obtained by subtracting the expression of the proposed adaptive sliding mode observer in (5.9) from (3.55). Assuming that the reference and the measured stator voltages are equal, then that the stator current error is given by

$$\begin{bmatrix} \dot{\tilde{i}}_\alpha \\ \dot{\tilde{i}}_\beta \end{bmatrix} = -\frac{R_s}{L_s}\begin{bmatrix} \tilde{i}_\alpha \\ \tilde{i}_\beta \end{bmatrix} + \begin{bmatrix} 0 & \tilde{\omega}_r \\ -\tilde{\omega}_r & 0 \end{bmatrix}\begin{bmatrix} \tilde{i}_\alpha \\ \tilde{i}_\beta \end{bmatrix} + \frac{1}{L_s}\begin{bmatrix} e_\alpha \\ e_\beta \end{bmatrix} - \frac{K(t)}{L_s}\begin{bmatrix} \mathrm{sgn}(\tilde{i}_\alpha) \\ \mathrm{sgn}(\tilde{i}_\beta) \end{bmatrix} \tag{5.11}$$

5.3.3 Design of the adaptive gain

In order to design the parameters of the adaptive gains, let us rewrite (5.11) as

$$\dot{\boldsymbol{S}} = \boldsymbol{\Psi} - \boldsymbol{\Gamma}\boldsymbol{u}, \tag{5.12}$$

with

$$\boldsymbol{u} = K(t)\mathrm{sgn}(\boldsymbol{S}), \tag{5.13}$$

where the functions $\boldsymbol{\Psi}$ and $\boldsymbol{\Gamma}$ are deduced from the expression in (5.11) and they are bounded. The ASMO gains are mostly designed such that the control

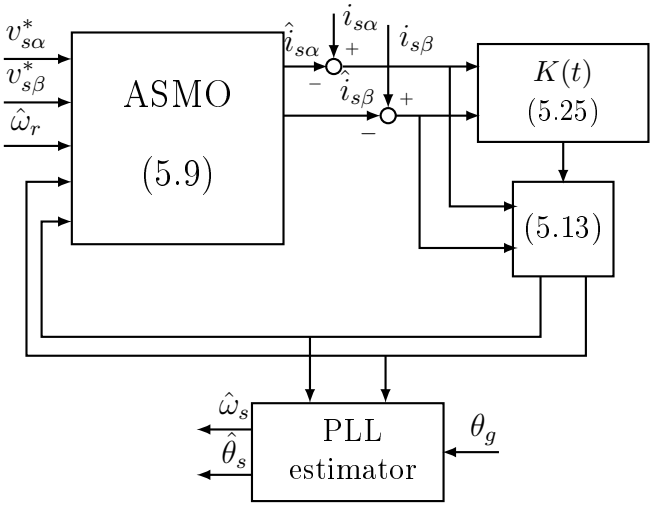

Figure 5.2: The diagram of the adaptive sliding mode observer.

Stellenbosch University https://scholar.sun.ac.za

$\boldsymbol{u}$ compensates for any bounded perturbation $\frac{\boldsymbol{\Psi}\text{sgn}(\boldsymbol{S})}{\boldsymbol{\Gamma}}$ and for the dynamics displayed in (5.13). $\boldsymbol{S}$ is the designed sliding surface. The aim of the adaptive sliding control is that the system trajectory reach and stays on the sliding surface $\boldsymbol{S} = \dot{\boldsymbol{S}} = 0$ in a finite time (which corresponds to the desired performance). Substituting (5.13) into (5.12) yields

$$\dot{\boldsymbol{S}} = \boldsymbol{\Psi} - \boldsymbol{\Gamma} K(t)\text{sgn}(\boldsymbol{S}) \tag{5.14}$$

The necessary and sufficient conditions for the existence of the sliding mode surface to be guaranteed using the adaptive sliding mode control is given by

$$K(t) \geq \frac{\boldsymbol{\Psi}\text{sgn}(\boldsymbol{S})}{\boldsymbol{\Gamma}} + \varepsilon \tag{5.15}$$

where $\varepsilon > 0$ is small.

The ideal adaptive law of the sliding gains is given by

$$K(t) = d \int_{t_0}^{t} |\boldsymbol{S}| d\tau, \tag{5.16}$$

where d is a positive constant while t_0 and t are the time variables; and, $|\boldsymbol{S}| = \sqrt{S_\alpha^2 + S_\beta^2}$ is the magnitude of the sliding surface. It can be seen that the expression in (5.16) will allow the system trajectory to keep increase while $\boldsymbol{S} \neq 0$. Further, it provides the ability to compensate for uncertainties with unknown bounds and force the sliding variable to converge to the desired sliding surface.

Also, the tuning of these parameters should allow the adaptive sliding mode observer to satisfy the Lyapunov stability criteria. The stability analysis of the ASMO is discussed in Section 5.3.4.

5.3.4 Stability analysis

Apart from providing high accuracy and reducing low chattering effect as seen in Section 5.3.3, the ASMO is also designed such that the Lyapunov stability criteria is fulfilled in order to guarantee the convergence of the adaptive sliding mode observer in a finite time. The aim is that the system trajectory of the adaptive sliding mode observer should reach and remain on the designed sliding surface.

In order to guarantee the convergence of the ASMO, its parameters are also designed such that the expressions in (5.4) are satisfied. The Lyapunov function for the ASMO is constructed as

$$V(x) = \frac{1}{2}\boldsymbol{S}^T\boldsymbol{S} + \frac{1}{2}(\bar{K} - K(t))^2, \tag{5.17}$$

with

$$\bar{K} = \max(K(t)), \tag{5.18}$$

Stellenbosch University https://scholar.sun.ac.za

where $\bar{K}$ is unknown and bounded. It can be seen that the expression in (5.17) is positive definite and the first expression of the Lyapunov stability criteria in (5.4), is satisfied. The time derivative of the constructed Lyapunov function displayed in (5.17) is given by

$$\dot{V}(x) = i_{s\alpha}\dot{i}_{s\alpha} + i_{s\beta}\dot{i}_{s\beta} - \dot{K}(t)(\bar{K} - K(t)) \tag{5.19}$$

Substituting the expressions of the time derivative of the estimated α-axis and β-axis stator currents from (5.9) into (5.19) yields,

$$\begin{aligned}\dot{V}(x) = &-\frac{R_s}{L_s}(\tilde{i}_{s\alpha}^2 + \tilde{i}_{s\beta}^2) - \tilde{i}_{s\alpha}[\frac{1}{L_s}(e_\alpha - K(t)\text{sgn}(\tilde{i}_{s\alpha})) + \tilde{\omega}_r i_{s\beta}] \\ &+ \tilde{i}_{s\beta}[\frac{1}{L_s}(e_\beta - K(t)\text{sgn}(\tilde{i}_{s\beta})) - \tilde{\omega}_r i_{s\alpha}] - d(\bar{K} - K(t))\sqrt{\tilde{i}_{s\alpha}^2 + \tilde{i}_{s\beta}^2}.\end{aligned} \tag{5.20}$$

From (5.17), it can be seen that the first term will always be negative. Then, the adaptive sliding gain should be large enough so that the system trajectory converge in a finite time to the sliding surface (in other words in order to meet the Lyapunov stability criteria), that is,

$$K(t) > \max(e_\alpha, e_\beta) \tag{5.21}$$

and assuming that estimated rotor speed is accurate enough as

$$\omega_r \approx \hat{\omega}_r, \tag{5.22}$$

the sliding motion on the designed sliding surface and the Lyapunov stability is guaranteed. When the system trajectory reaches the sliding surface, it yields

$$\dot{\boldsymbol{S}} = \boldsymbol{S} = 0. \tag{5.23}$$

Substituting (5.22) and (5.23) into (5.11) yields

$$\begin{bmatrix}\hat{e}_\alpha \\ \hat{e}_\beta\end{bmatrix} \approx K(t) \begin{bmatrix}\text{sgn}(i_{s\alpha} - \hat{i}_{s\alpha}) \\ \text{sgn}(i_{s\beta} - \hat{i}_{s\beta})\end{bmatrix} \tag{5.24}$$

where $\hat{e}_\alpha$ and $\hat{e}_\beta$ are the α-axis and β-axis estimated back-EMFs, respectively. The estimated back-EMF are used in order to estimate the slip speed/angle. The proposed estimator is depicted in Figure 5.2.

However, the adaptive gain, $K(t)$, displayed in (5.16) will continue to increase and could become unbounded even when the sliding surface is reached by the system trajectory. This implies that it will lead to more chattering effects. Also, in practical applications this adaptive law shows slow response to disturbance. In [56], this drawback is solved by adding an exponential term

Stellenbosch University https://scholar.sun.ac.za

in the adaptive gain which disappears when the system trajectory is reached. The new adaptive gain is given by

$$K(t) = d\int_{t_0}^{t} |\boldsymbol{S}|d\tau + \gamma_0(e^{\gamma_1|\boldsymbol{S}|^p} - 1), \tag{5.25}$$

where γ_0, γ_1 and p are strictly positive integers. The design process of the adaptive law in (5.25) is presented in [56]. The added exponential term provides an extra high gain only when the state trajectory is far from the sliding surface ($\boldsymbol{S} \neq 0$ and is very large). The exponential term helps the system trajectory to reach the desired sliding surface quicker than the gain with the integral only. When the state trajectory leaves the designed sliding surface, it can be seen that the exponential term will turn the state trajectory around to head back to the designed sliding surface. When $S \to 0$, the exponential term reduces its value rapidly until it disappears. After reaching the sliding surface, the overall gain in (5.25), is reduced. Therefore, this helps in reducing the chattering effect.

The tuning of p affects the response of system trajectory leaving or trying to reach the desired sliding surface. A large p will speed up the response while increasing the accuracy. A proper design of γ_0, γ_1 and p yields to lower chattering and high accuracy of adaptive sliding mode control. It was also shown in [56], that the use of the adaptive gain in (5.25) guarantees the stability of the ASMO.

5.4 Super-twisting sliding mode observer

In this Section, the super-twisting sliding mode observer (STSMO) for sensor-less control of RDFIG systems is discussed. The motivation of the STSMO is presented together with the design and the stability analysis of the proposed STSMO are also presented. This section is adapted from [38].

5.4.1 Motivation

The super-twisting algorithm (STA) for the SMO is considered to be an excellent solution to alleviate the chattering behavior. It also increases the dynamic performance of the SMO [59–67]. The super-twisting sliding mode observer uses the super-twisting algorithm instead of the standard sliding mode control functions (the saturation, sigmoid or signum functions). Although the super-twisting algorithm-based SMO (STSMO) for the sensor-less control of the induction machine drive is proposed in [62] and recently similar work on permanent magnet synchronous machine drives in [63] have been presented, the STSMO for sensor-less control of RDFIG systems is still missing in the literature. Also, the improvement on its effectiveness under various operating

Stellenbosch University https://scholar.sun.ac.za

conditions, that is; the improvement of their robustness to parameter variations, the efficiency of the overall system and the dynamic performance of the system, still needs to be investigated.

5.4.2 Design of the STSMO

The STSMO is constructed based on (3.55). The super-twisting sliding mode observer (STSMO) uses the stator current and the back-EMFs as state variables. Further, the STA is also used to enforce the system trajectory to reach and remain on the predefined sliding surface in a finite time. The STSMO is constructed as,

$$L_s \begin{bmatrix} \dot{\hat{i}}_{s\alpha} \\ \dot{\hat{i}}_{s\beta} \end{bmatrix} = \begin{bmatrix} -R_s & 0 \\ 0 & -R_s \end{bmatrix} \begin{bmatrix} \hat{i}_{s\alpha} \\ \hat{i}_{s\beta} \end{bmatrix} + \begin{bmatrix} v^*_{s\alpha} \\ v^*_{s\beta} \end{bmatrix} + L_s \begin{bmatrix} 0 & \hat{\omega}_r \\ -\hat{\omega}_r & 0 \end{bmatrix} \begin{bmatrix} i_{s\alpha} \\ i_{s\beta} \end{bmatrix} + \begin{bmatrix} z_\alpha \\ z_\beta \end{bmatrix}, \quad (5.26)$$

where the superscript $(\hat{})$ denotes the estimated value, while z_α and z_β are the outputs of the super-twisting sliding mode control functions. The estimation error is obtained by subtracting (5.26) from (3.55), that is,

$$L_s \begin{bmatrix} \dot{\tilde{i}}_{s\alpha} \\ \dot{\tilde{i}}_{s\beta} \end{bmatrix} = \begin{bmatrix} -R_s & 0 \\ 0 & -R_s \end{bmatrix} \begin{bmatrix} \tilde{i}_{s\alpha} \\ \tilde{i}_{s\beta} \end{bmatrix} + L_s \begin{bmatrix} 0 & \tilde{\omega}_r \\ -\tilde{\omega}_r & 0 \end{bmatrix} \begin{bmatrix} i_{s\alpha} \\ i_{s\beta} \end{bmatrix} + \begin{bmatrix} e_\alpha - z_\alpha \\ e_\beta - z_\beta \end{bmatrix}, \quad (5.27)$$

where $(\dot{})$ and $(\tilde{})$ denotes the time derivative value and the error value between the estimated and the real values.

According to [59–61, 64, 65, 67], the super-twisting sliding mode control function can be expressed as,

$$\begin{bmatrix} z_\alpha \\ \dot{\psi}_1 \\ z_\beta \\ \dot{\psi}_2 \end{bmatrix} = \begin{bmatrix} k_1 \sqrt{|\tilde{i}_{s\alpha}|}\mathrm{sgn}(\tilde{i}_{s\alpha}) - \psi_1 \\ -k_2 \mathrm{sgn}(\tilde{i}_{s\alpha}) \\ k_3 \sqrt{|\tilde{i}_{s\beta}|}\mathrm{sgn}(\tilde{i}_{s\beta}) - \psi_2 \\ -k_4 \mathrm{sgn}(\tilde{i}_{s\alpha}) \end{bmatrix}, \quad (5.28)$$

where k_1, k_2, k_3 and k_4 are the STSMO gains to be determined. Thus, the schematic of the proposed STSMO for the RDFIG is shown in Figure 5.3. The STSMO gains, from (5.28), are designed such that the Lyapunov stability criteria is fulfilled. Also, the choice of the STSMO gains should provide fast enough response. Substituting (5.28) into (5.27) yields

$$L_s \begin{bmatrix} \dot{\tilde{i}}_{s\alpha} \\ \dot{\tilde{i}}_{s\beta} \end{bmatrix} = \begin{bmatrix} -k_1 \sqrt{|\tilde{i}_{s\alpha}|}\mathrm{sgn}(\tilde{i}_{s\alpha}) + \psi_1 + e_\alpha + f_1 \\ k_2 \sqrt{|\tilde{i}_{s\beta}|}\mathrm{sgn}(\tilde{i}_{s\beta}) + \psi_2 + e_\beta + f_2 \end{bmatrix}, \quad (5.29)$$

where

$$\begin{bmatrix} f_1 \\ f_2 \end{bmatrix} = \begin{bmatrix} -R_s \tilde{i}_{s\alpha} + L_s \tilde{\omega}_r i_{s\beta} \\ -R_s \tilde{i}_{s\beta} - L_s \tilde{\omega}_r i_{s\alpha} \end{bmatrix} \quad (5.30)$$

Stellenbosch University https://scholar.sun.ac.za

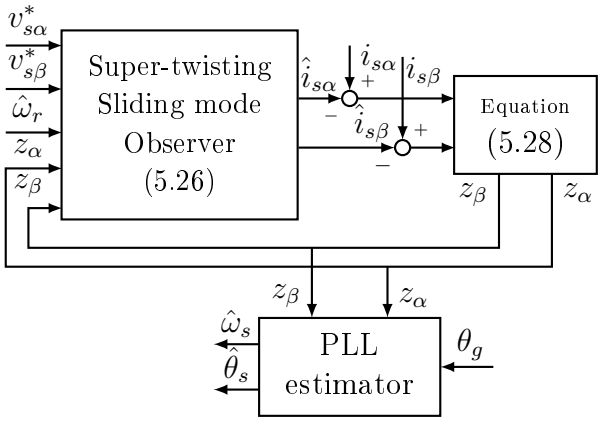

Figure 5.3: The PLL-based STSMO estimator.

Assuming that all the expressions in (5.30) are globally bounded, (f_1 and f_2 are globally bounded), then,

$$\begin{bmatrix} |-R_s\tilde{i}_{s\alpha} + L_s\tilde{\omega}_r i_{s\beta}| \\ |-R_s\tilde{i}_{s\beta} - L_s\tilde{\omega}_r i_{s\alpha}| \end{bmatrix} \leq \begin{bmatrix} \sigma_1|\tilde{i}_{s\alpha}|^{0.5} \\ \sigma_2|\tilde{i}_{s\beta}|^{0.5} \end{bmatrix} \tag{5.31}$$

with σ_1 and σ_2 being chosen large enough so that the inequalities in (5.31) are satisfied.

5.4.3 Stability analysis

The design of the STSMO gains is conducted such that the Lyapunov stability criteria is fulfilled and that the system trajectory reaches and remains on the predefined sliding surface in a finite time. To this end, a strong Lyapunov function is constructed.

$$\boldsymbol{\psi}_\alpha = \begin{bmatrix} \sqrt{|\tilde{i}_{s\alpha}|}\text{sgn}(\tilde{i}_{s\alpha}) & \psi_1 \end{bmatrix}^T, \tag{5.32}$$

and

$$\boldsymbol{\psi}_\beta = \begin{bmatrix} \sqrt{|\tilde{i}_{s\beta}|}\text{sgn}(\tilde{i}_{s\beta}) & \psi_2 \end{bmatrix}^T, \tag{5.33}$$

then, similar to [64, 66], the Lyapunov function is chosen as,

$$V(x) = \frac{1}{2}\boldsymbol{\psi}_\alpha^T\mathbf{P}_\alpha\boldsymbol{\psi}_\alpha + \frac{1}{2}\boldsymbol{\psi}_\beta^T\mathbf{P}_\beta\boldsymbol{\psi}_\beta, \tag{5.34}$$

where $\mathbf{P}_\alpha$ and $\mathbf{P}_\beta$ are given by,

$$\mathbf{P}_\alpha = \begin{bmatrix} 4k_2 + k_1^2 & -k_1 \\ -k_1 & 2 \end{bmatrix} \tag{5.35}$$

and

$$\mathbf{P}_\beta = \begin{bmatrix} 4k_4 + k_3^2 & -k_3 \\ -k_3 & 2 \end{bmatrix}. \tag{5.36}$$

Stellenbosch University https://scholar.sun.ac.za

Substituting (5.35) and (5.36) into(5.31), the constructed Lyapunov function becomes,

$$\begin{aligned} V(x) = {} & 2k_2|\tilde{i}_{s\alpha}| + 0.5\psi_1^2 + 0.5(k_1|\tilde{i}_{s\alpha}|^{0.5}\mathrm{sgn}(\tilde{i}_{s\alpha}) - \psi_1)^2 \\ & + 2k_4|\tilde{i}_{s\beta}| + 0.5\psi_2^2 + 0.5(k_3|\tilde{i}_{s\beta}|^{0.5}\mathrm{sgn}(\tilde{i}_{s\beta}) - \psi_2)^2. \end{aligned} \tag{5.37}$$

The time derivatives of $\boldsymbol{\psi}_\alpha$ and $\boldsymbol{\psi}_\beta$ are given by,

$$\dot{\boldsymbol{\psi}}_\alpha = \begin{bmatrix} \frac{1}{2\sqrt{|\tilde{i}_{s\alpha}|}}\Big(- k_1\sqrt{|\tilde{i}_{s\alpha}|}\mathrm{sgn}(\tilde{i}_{s\alpha}) + \psi_1 + f_1\Big) \\ -k_2\mathrm{sgn}(\tilde{i}_{s\alpha}) \end{bmatrix} \tag{5.38}$$

and

$$\dot{\boldsymbol{\psi}}_\beta = \begin{bmatrix} \frac{1}{2\sqrt{|\tilde{i}_{s\beta}|}}\Big(- k_1\sqrt{|\tilde{i}_{s\beta}|}\mathrm{sgn}(\tilde{i}_{s\beta}) + \psi_2 + f_2\Big) \\ -k_4\mathrm{sgn}(\tilde{i}_{s\beta}) \end{bmatrix}. \tag{5.39}$$

From (5.38), (5.39) and (5.31), the time derivative of the constructed Lyapunov function is given by,

$$\dot{V}(x) = -\frac{k_1}{|\tilde{i}_{s\alpha}|^{0.5}}\boldsymbol{\psi}_\alpha^T\mathbf{X}_\alpha\boldsymbol{\psi}_\alpha - \frac{k_3}{|\tilde{i}_{s\beta}|^{0.5}}\boldsymbol{\psi}_\beta^T\mathbf{X}_\beta\boldsymbol{\psi}_\beta \tag{5.40}$$

where,

$$\mathbf{X}_\alpha = \begin{bmatrix} 2k_2 + k_1^2 - (k_1 + \frac{4k_2}{k_1})\sigma_1 & -k_1 + 2\sigma_2 \\ -k_1 + 2\sigma_1 & 1 \end{bmatrix} \tag{5.41}$$

and,

$$\mathbf{X}_\beta = \begin{bmatrix} 2k_4 + k_3^2 - (k_3 + \frac{4k_4}{k_3})\sigma_2 & -k_3 + 2\sigma_2 \\ -k_3 + 2\sigma_2 & 1 \end{bmatrix}. \tag{5.42}$$

Therefore, it can be seen that, the conditions necessary to fulfil the Lyapunov criterion are, $\boldsymbol{X_\alpha} > 0$ and $\boldsymbol{X_\beta} > 0$. Hence, the STSMO gains are chosen as,

$$\begin{bmatrix} k_1 \\ k_2 \\ k_3 \\ k_4 \end{bmatrix} > \begin{bmatrix} 2\sigma_1 \\ k_1\frac{\sigma_1 k_1 - k_1^2}{2k_1 - 4\sigma_1} \\ 2\sigma_2 \\ k_3\frac{\sigma_2 k_3 - k_3^2}{2k_3 - 4\sigma_2} \end{bmatrix} \tag{5.43}$$

Higher values of STSMO gains provide fast enough response of the observer but could lead to noise and harmonics in the estimation signal. Hence, there is a trade off between fast response and signal quality when it comes to designing STSMO gains. A proper design leads to fast enough response and good signal quality of the estimation. By enforcing the sliding motion, the sliding surface, $\tilde{i}_{s\alpha} = \tilde{i}_{s\beta} = 0$ and $\dot{\tilde{i}}_{s\alpha} = \dot{\tilde{i}}_{s\beta} = 0$, and with the assumption that $\omega_r = \hat{\omega}_r$, then (5.27), the estimated back-EMF space vector becomes equal to the outputs of the super-twisting sliding mode control functions ($z_\alpha = \hat{e}_\alpha$ and $z_\beta = \hat{e}_\beta$). Given that the back-EMF space vector contains the information of the slip angle, as it can be seen in (3.56), the slip speed/angle can be extracted from the outputs of the super-twisting sliding mode control functions.

Stellenbosch University https://scholar.sun.ac.za

5.5 High order sliding mode observer

In this section, a high order sliding mode observer (HOSMO) for sensor-less control of the rotor-tied doubly-fed induction generator (RDFIG) systems is presented. This section is adapted from [39].

5.5.1 Motivation

In the different sliding mode observers presented from Section 5.2 to Section 5.4, the dynamics of the back-EMF has been neglected. This implies that the estimation performance is limited. In this Section, a high order sliding mode observer, in which the dynamics of the back EMFs are taken into consideration, is proposed. Hence, the proposed HOSMO improves the estimation performance.

5.5.2 Design of the high-order sliding mode observer

Compared to SMOs proposed for sensor-less control of RDFIG system, the proposed high order sliding mode observers in this Section takes into account the dynamics of the estimated back-EMF space vector ($\dot{\boldsymbol{e}} \neq 0$). Hence, the dynamic performance of the estimation is enhanced.

Based on (3.58), the HOSMO is constructed as

$$\begin{bmatrix} \dot{\hat{\mathbf{i}}} \\ \dot{\hat{\mathbf{e}}} \end{bmatrix} = \begin{bmatrix} \boldsymbol{\hat{A}_{11}} & \boldsymbol{A_{12}} \\ 0 & \boldsymbol{\hat{A}_{22}} \end{bmatrix} \begin{bmatrix} \mathbf{i} \\ \hat{\mathbf{e}} \end{bmatrix} + \begin{bmatrix} \boldsymbol{B_{11}} \\ 0 \end{bmatrix} \mathbf{v} - \frac{1}{L_s}\mathbf{M}\text{sgn}(\mathbf{S}), \tag{5.44}$$

where $\hat{\mathbf{e}} = \begin{bmatrix} \hat{e}_\alpha & \hat{e}_\beta \end{bmatrix}^T$, $\hat{\mathbf{i}} = \begin{bmatrix} \hat{i}_{s\alpha} & \hat{i}_{s\beta} \end{bmatrix}^T$, $\mathbf{S} = \begin{bmatrix} \hat{i}_{s\alpha} - i_{s\alpha} & \hat{i}_{s\beta} - i_{s\beta} \end{bmatrix}^T$, $\boldsymbol{\hat{A}_{11}} = -\frac{R_s}{L_s}\mathbf{I} - \hat{\omega}_r\mathbf{J}$, $\boldsymbol{\hat{A}_{22}} = \hat{\omega}_s\mathbf{J}$, $\boldsymbol{B_{11}} = \frac{1}{L_s}\mathbf{I}$ and $\mathbf{M} = \begin{bmatrix} m_1 & 0 & m_3 & 0 \\ 0 & m_2 & 0 & m_4 \end{bmatrix}^T$, where m_1, m_2, m_3 and m_4 are the HOSMO gains. The schematic of the proposed HOSMO is depicted in Figure 5.4.

The difference between (3.58) and (5.44) yields that the stator current error is given by

$$\begin{bmatrix} \dot{\tilde{i}}_{s\alpha} \\ \dot{\tilde{i}}_{s\beta} \end{bmatrix} = \begin{bmatrix} -\tilde{\omega}_r i_{s\beta} - \frac{m_1}{L_s}\text{sng}(\hat{i}_{s\alpha} - i_{s\alpha}) + \frac{1}{L_s}\tilde{e}_\alpha \\ \tilde{\omega}_r i_{s\alpha} - \frac{m_2}{L_s}\text{sng}(\hat{i}_{s\beta} - i_{s\beta}) + \frac{1}{L_s}\tilde{e}_\beta \end{bmatrix}, \tag{5.45}$$

where the superscript ($\tilde{}$) denotes the difference between the estimated value and the real value.

5.5.3 Stability analysis

The sliding mode observer gains are determined such that the observer converge. The Lyapunov function is given by

$$V(x) = \frac{1}{2}(\tilde{i}_{s\alpha}^2 + \tilde{i}_{s\beta}^2). \tag{5.46}$$

Stellenbosch University https://scholar.sun.ac.za

The time derivative of the Lyapunov function is given by

$$\begin{aligned}\dot{V}(x) = &-\tilde{i}_{s\alpha}\Big[\tilde{\omega}_r i_{s\beta} - \frac{1}{L_s}\tilde{e}_\alpha\Big] - \tilde{i}_{s\beta}\Big[-\tilde{\omega}_r i_{s\alpha} - \frac{1}{L_s}\tilde{e}_\beta\Big] \\ &- \frac{m_1}{L_s}|\tilde{i}_{s\alpha}| - \frac{m_2}{L_s}|\tilde{i}_{s\beta}|,\end{aligned} \tag{5.47}$$

where, m_1 and m_2 should be at least

$$\begin{bmatrix} m_1 \\ m_2 \end{bmatrix} > \begin{bmatrix} |L_s\tilde{\omega}_r i_{s\beta} - \tilde{e}_\alpha| \\ |-L_s\tilde{\omega}_r i_{s\alpha} - \tilde{e}_\beta| \end{bmatrix}, \tag{5.48}$$

so that the robustness of the HOSMO to disturbance and parameter mismatch is ensured.

When $V(x)$ converge to zero, $\tilde{i}_{s\alpha}$ and $\tilde{i}_{s\alpha}$ will be controlled to zero. If the speed estimation is accurate enough ($\omega_r \approx \hat{\omega}_r$), when the sliding motion occurs, the back EMF errors are given by

$$\begin{bmatrix} \tilde{e}_\alpha \\ \tilde{e}_\beta \end{bmatrix} = \begin{bmatrix} m_1 \mathrm{sgn}(\hat{i}_{s\alpha} - i_{s\alpha}) \\ m_2 \mathrm{sgn}(\hat{i}_{s\beta} - i_{s\beta}) \end{bmatrix}. \tag{5.49}$$

Differentiating (3.58) and (5.44) with the assumption that the estimated slip speed ($\omega_s \approx \hat{\omega}_s$) is accurate enough, yields that the dynamic errors of the back-EMF space vector can be expressed as

$$\begin{bmatrix} \dot{\tilde{e}}_\alpha \\ \dot{\tilde{e}}_\beta \end{bmatrix} = \begin{bmatrix} -\tilde{e}_\beta\hat{\omega}_s - \frac{m_3}{L_s}\mathrm{sgn}(\hat{i}_{s\alpha} - i_{s\alpha}) \\ \tilde{e}_\alpha\hat{\omega}_s - \frac{m_4}{L_s}\mathrm{sgn}(\hat{i}_{s\beta} - i_{s\beta}) \end{bmatrix}. \tag{5.50}$$

Substituting (5.49) into (5.50) yields

$$\begin{bmatrix} \dot{\tilde{e}}_\alpha \\ \dot{\tilde{e}}_\beta \end{bmatrix} = \begin{bmatrix} -\frac{m_3}{m_1 L_s} & -\hat{\omega}_s \\ \hat{\omega}_s & \frac{m_4}{m_2 L_s} \end{bmatrix} \begin{bmatrix} \tilde{e}_\alpha \\ \tilde{e}_\beta \end{bmatrix}. \tag{5.51}$$

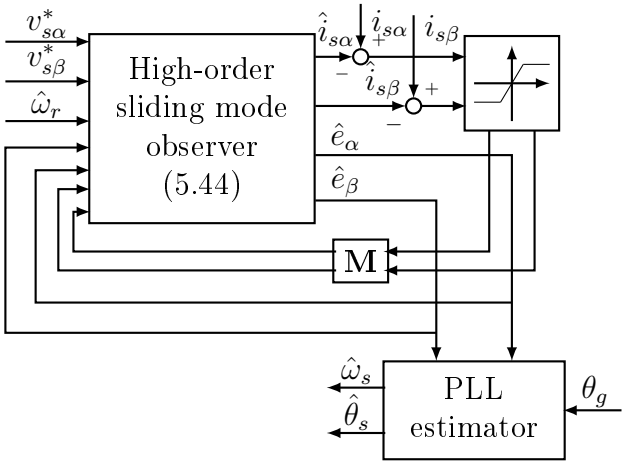

Figure 5.4: Proposed PLL-based HOSMO estimator scheme.

Stellenbosch University https://scholar.sun.ac.za

In (5.51), the time derivative of the slip speed $\dot{\hat{\omega}}_s$ is negligible since the mechanical time constant is far greater than electrical time constant. Hence, the back-EMF space vector is considered the only time varying quantity. Therefore, the analysis using second-order differential equation with constant coefficients applies for the dynamic error displayed in (5.51).

The characteristic equation of (5.51) can be written as

$$\mathrm{p}^2 + (\frac{m_3}{m_1 L_s} + \frac{m_4}{m_2 L_s})\mathrm{p} + (\hat{\omega}_s^2 + \frac{m_3 m_4}{m_1 m_2 L_s^2}) = 0, \tag{5.52}$$

where p is the Laplace operator. Solving (5.52) yields that the eigenvalues are given by

$$\mathrm{p}_{1,2} = \frac{-(\frac{m_3}{m_1} + \frac{m_4}{m_2}) \pm \sqrt{(\frac{m_3}{m_1} + \frac{m_4}{m_2})^2 - 4(L_s^2\hat{\omega}_s^2 + \frac{m_3 m_4}{m_1 m_2})}}{2L_s}. \tag{5.53}$$

Given that

$$|\frac{m_3}{m_1} + \frac{m_4}{m_2}| > \sqrt{(\frac{m_3}{m_1} + \frac{m_4}{m_2})^2 - 4(L_s^2\hat{\omega}_s^2 + \frac{m_3 m_4}{m_1 m_2})}, \tag{5.54}$$

it can be seen that (5.53) has a negative real part which means that the system is asymptotically stable. The observer gains can be designed based on (5.53), that is expressed as

$$\mathrm{p}^2 + 2\xi\omega_n \mathrm{p} + \omega_n^2 = 0, \tag{5.55}$$

with the natural frequency $\omega_n = \sqrt{\hat{\omega}_s^2 + m_3 m_4/(m_1 m_2 L_s^2)}$ and the damping ratio $\xi = \frac{\frac{m_3}{m_1} + \frac{m_4}{m_2}}{2\sqrt{L_s^2\hat{\omega}_s^2 + m_3 m_4/(m_1 m_2 L_s^2)}}$. The convergence rate of $\tilde{e}_\alpha$ and $\tilde{e}_\beta$ depends on the product of $\omega_n\xi$. The bigger $\omega_n\xi$ is, the more rapidly the dynamic errors of the back-EMF will converge. By tuning properly ξ and ω_n a good dynamic performance can be achieved.

The estimated slip speed $\hat{\omega}_s$ is extracted from the estimated back-EMF space vector using a PLL estimator. However, if the estimated slip speed is not accurate enough the estimated back-EMF will not converge to the real one accurately. But, through proper design of m_3 and m_4, the back-EMF errors $\tilde{e}_\alpha$ and $\tilde{e}_\beta$ can settle to the desired vicinity. As m_3 and m_4 get larger, the size of the vicinity gets smaller. Hence through a proper design of m_3 and m_4, the estimated back-EMF can converge approximately to the real one.

5.6 Phase locked loop

From (3.56), it was shown that the back-EMF includes the slip speed and position information. The aim of the PLL estimator is to track the angle of the estimated back-EMF space vector. Given that the back-EMF space

Stellenbosch University https://scholar.sun.ac.za

vector is estimated using the sliding mode control functions. And, that the sliding mode control functions include high frequency switching functions, the estimated back-EMF includes noise and harmonic components. The estimated back-EMF is given by,

$$\begin{bmatrix}\hat{e}_\alpha \\ \hat{e}_\beta\end{bmatrix} = \frac{L_m}{L_s}|\vec{i}_r^s|\omega_g \begin{bmatrix}\sin\hat{\theta}_k + N_1(t) \\ \cos\hat{\theta}_k + N_2(t)\end{bmatrix} \tag{5.56}$$

where $\hat{\theta}_k = \hat{\theta}_s + \hat{\phi}_k$ is the estimated angle and $N_1(t)$ and $N_2(t)$ are the total noise and harmonic components. The detailed schematic of the PLL estimator is presented in Figure 5.5. Based on Figure 5.5, the position error, ϵ, is deduced as

$$\epsilon = \frac{L_m|\vec{i}_r^s|\omega_g}{\sqrt{\hat{e}_\alpha^2 + \hat{e}_\beta^2}}\Big(\underbrace{\big(\sin\hat{\theta}_k\cos\bar{\theta}_k - \cos\hat{\theta}_k\sin\bar{\theta}_k\big)}_{\text{Low-frequency terms}} + \underbrace{N_1(t)\cos\bar{\theta}_k - N_2(t)\sin\bar{\theta}_k}_{\text{High-frequency terms}}\Big), \tag{5.57}$$

where $\bar{\theta}_k = \bar{\theta}_s + \bar{\phi}_k$ is the tracking angle and $|\hat{\vec{e}}| = L_m|\vec{i}_r^s|\omega_g$. Rewriting (5.57), yields

$$\epsilon = \frac{L_m|\vec{i}_r^s|\omega_g}{\sqrt{\hat{e}_\alpha^2 + \hat{e}_\beta^2}}\Big(\underbrace{sin(\hat{\theta}_k - \bar{\theta}_k)}_{\text{Low-frequency terms}} + \underbrace{N_1(t)\cos\bar{\theta}_k - N_2(t)\sin\bar{\theta}_k}_{\text{High-frequency terms}}\Big). \tag{5.58}$$

It can be seen from (5.58) that the position error consists of a lower frequency term and two-high frequency terms. The rotor position information is obtained from the first low frequency term and thus, the two high frequency terms can be suppressed easily by a loop filter [127]. With the two high frequency terms suppressed, and the angle difference in the first term assumed to be very small, the error position can be simplified to,

$$\epsilon \approx \frac{L_m|\vec{i}_r^s|\omega_g}{\sqrt{\hat{e}_\alpha^2 + \hat{e}_\beta^2}}\big(\hat{\theta}_k - \bar{\theta}_k\big). \tag{5.59}$$

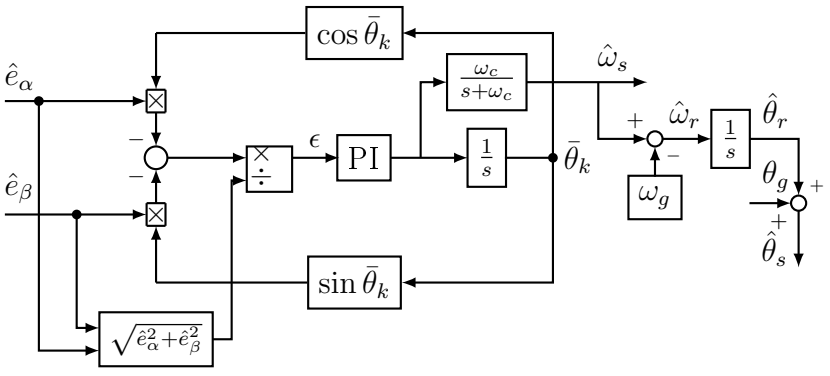

Figure 5.5: A detailed schematic of the proposed PLL estimator.

Stellenbosch University https://scholar.sun.ac.za

In contrast to the PLL estimator proposed in [1], here the proposed PLL estimator does not include a judgement function. Instead, based on the estimated slip speed equation, an estimated rotor angular speed is deduced as

$$\hat{\omega}_r = \hat{\omega}_s - \omega_g \tag{5.60}$$

where $\hat{\omega}_r$ is the estimated rotor angular speed, ω_g, is the grid angular speed and $\hat{\omega}_s$ is the output of the proposed PLL estimator. The estimated slip speed, $\hat{\theta}_s$, is calculated by deducing the estimated rotor angle, $\hat{\theta}_r$, from $\hat{\omega}_r$. It is important to note that the initial estimated rotor angle should be the actual rotor angle in order to improve the stability of the PLL estimator. Hence the estimated slip angle is calculated as,

$$\hat{\theta}_s = \hat{\theta}_r + \theta_g. \tag{5.61}$$

The estimated slip angle estimator proposed here allows for a smooth transition from sub-synchronous to super-synchronous or vice versa of the slip angle.

5.6.1 Design of Parameters

The PLL estimator gains are designed based on the consideration of the anti-disturbance performance [10]. Based on small signal analysis, the PLL's transfer function based on Figure 5.5 is described by,

$$\frac{\hat{\theta}_k}{\bar{\theta}_k} = \frac{K_p s + K_i}{s^2 + K_p s + K_i}, \tag{5.62}$$

where K_p and K_i are the proportional and integral gains of the PI controller.

The PI gains are designed using the pole placement method such that $K_p = 2\rho$ and $K_i = \rho^2$. ρ is to be determined based on the anti-disturbance performance. The estimated slip speed and the estimated acceleration are described by,

$$\begin{bmatrix} \dot{\hat{\theta}}_k \\ \dot{\hat{\omega}}_s \end{bmatrix} = \begin{bmatrix} \hat{\omega}_s \\ g \end{bmatrix} \tag{5.63}$$

where g is the acceleration. The acceleration is given by,

$$g = \frac{P\Delta\tau}{J}, \tag{5.64}$$

where P, $\Delta\tau$ and J are the number of pole pairs, the torque change and J is the inertia. The expression of the tracking slip speed and tracking slip acceleration are described by,

$$\begin{bmatrix} \dot{\bar{\theta}}_k \\ \dot{\bar{\omega}}_s \end{bmatrix} = \begin{bmatrix} \bar{\omega}_s + K_p\epsilon \\ K_i\epsilon \end{bmatrix} \tag{5.65}$$

Stellenbosch University https://scholar.sun.ac.za

Differentiating (5.63) to (5.65) yields,

$$\begin{bmatrix} \dot{\hat{\theta}}_k - \dot{\bar{\theta}}_k \\ \dot{\hat{\omega}}_s - \dot{\bar{\omega}}_s \end{bmatrix} = \begin{bmatrix} \hat{\omega}_s - \bar{\omega}_s - K_p\epsilon \\ g - K_i\epsilon \end{bmatrix} \tag{5.66}$$

Assuming that $\dot{\hat{\omega}}_s - \dot{\bar{\omega}}_s = 0$ and $\dot{\hat{\theta}}_k - \dot{\bar{\theta}}_k = 0$, then the solution to (5.66) is given by,

$$\begin{bmatrix} \hat{\omega}_s - \bar{\omega}_s \\ \epsilon \end{bmatrix} = \begin{bmatrix} \frac{2g}{\rho} \\ \frac{g}{\rho^2} \end{bmatrix} \tag{5.67}$$

Hence, from (5.67) it can be seen that the selection of ρ can be determined by,

$$\rho = \sqrt{\frac{g}{\epsilon_{\max}}}, \tag{5.68}$$

where $\epsilon_{\max}$ is the expected maximum value of the slip position error. Also, it can be seen from (5.67), that with higher values of ρ, the error between the estimated and tracking slip angular speed is reduced. With $\epsilon_{\max} = \frac{\pi}{12}$ and based on the machine data, ρ can be determined and from which K_p and K_i are also determined. For this thesis, the tuned PLL gains were $K_p = 240$ and $K_i = 14400$.

5.7 Summary

In this Chapter, the slip speed estimators for sensor-less control of the RDFIG systems are presented. The slip speed estimators uses the association of the sliding mode observers and the PLL estimators. The sliding mode observers discussed in this Chapter are the SMO, the ASMO, the STSMO and the HOSMO. The gains of the proposed sliding mode observers are design such that the Lyapunov stability criteria is satisfied. And, the sliding mode observers converge in a finite time. The proposed sliding mode observers use the back-EMF space vector and the stator current space vector, as state variables. This implies that the estimation can start even before the machine is connected to the grid. The PLL estimator is used in order to improve the estimation performance.

Stellenbosch University https://scholar.sun.ac.za

Chapter 6

Experimental results and discussions

6.1 Introduction

In Chapter 4 and Chapter 5, the proposed sensor-less control of the RDFIG system and the proposed slip speed estimators are provided, respectively. In this Chapter, the experimental setup, the performance of the proposed sensor-less control strategy and the comparative study of the proposed slip speed estimators are provided

6.2 Experimental set-up

The test-bed on which the experimental tests of the proposed sensor-less control strategies discussed in the thesis is portrayed in Figure 6.1. The core of the test-bench is the National Instrument (NI) PXIe-8115 embedded real-time controller. The proposed sensor-less control strategy is implemented in LabVIEW. The test-bench also includes two NI 7841R FPGA modules that input or output signals into or from the PXIe-8115. A three-phase 5.5-kW custom-designed rotor-tied DFIG is coupled to a three-phase 22-kW induction machine. The parameters of the 5.5-kW custom-designed rotor-tied DFIG are given in the Appendix. The test-bench is also composed of two 8.7-kVA custom-modified commercially available SEW power converters connected in the back-to-back configuration. The data of 8.7-kVA custom-modified commercially available SEW power converters are given in Appendix A. The measurement of the three-phase voltages and that of the three-phase currents are conducted using LEM LV25-P and LA55-P sensors, respectively. A GI341 BAUMER incremental encoder, mounted on the rotor shaft, is only used for the measurement of the actual rotor shaft speed/angle in order to compare with the estimated quantities. The carrier switching frequency of the PWM is 5 kHz. An L filter is used for the filtering of the harmonics generated by the

Stellenbosch University https://scholar.sun.ac.za

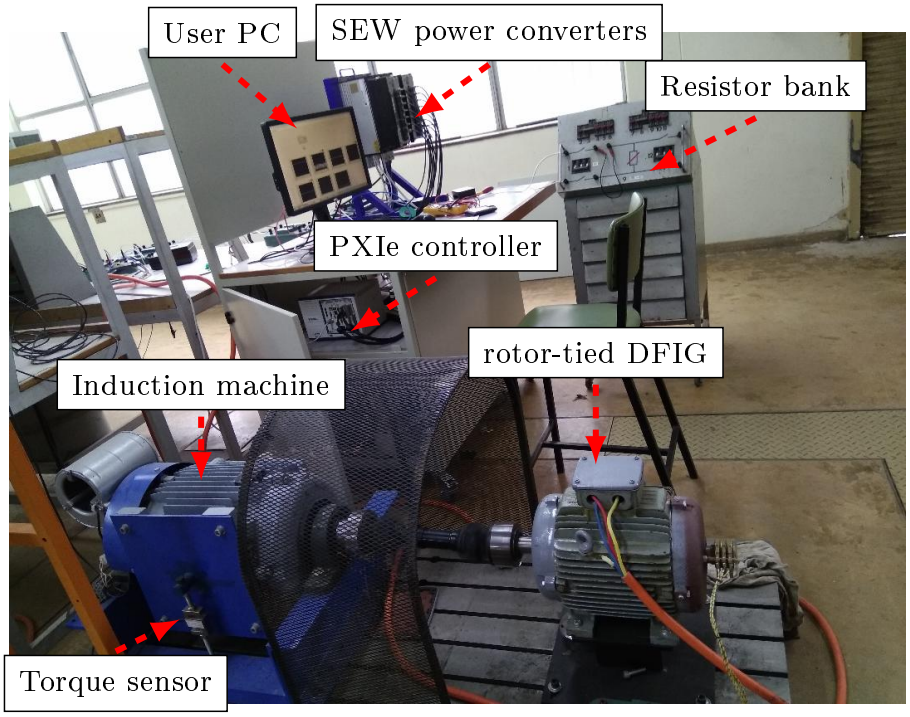

Figure 6.1: An image of the test-bench set-up.

grid side converter. The data of the L filter is shown in Appendix A. Further details on the test-bench is discussed in Appendix A.

6.3 Start-up of the RDFIG system

In this section, the start up procedure of the grid-connected RDFIG system is presented. The GSC is activated first. To start with, the three-phase grid voltage is measured and the grid angle, θ_g, is calculated using the SRF-PLL discussed in Section 4.5. The parameters of the PI controller of the SRF-PLL are chosen as $T_l = 0.051$ and $K_l = 1.001$. The calculated grid angle is used for the transformation of the three-phase grid voltage into the synchronous $dq0$-reference frame.

In Figure 6.2(a), the phase A grid voltage and the calculated grid angle are displayed. It can be seen that the SRF-PLL helps in tracking the grid voltage angle. It should be noted that if the line-to-line three-phase grid voltage is measured, then either the addition or subtraction of $\frac{\pi}{6}$ on the calculated grid angle is necessary. The addition or subtraction of of $\frac{\pi}{6}$ depends on the sequence of the measured three-phase grid voltage. The PI gains of the grid side converter control strategy are designed as discussed in Section 4.4. The inner PI gains are $K_{pi} = 30$ and $T_{ii} = 0.003$, and the outer PI gains are chosen as are $K_{pv} = 0.73$ and $T_{iv} = 0.03$.

Stellenbosch University https://scholar.sun.ac.za

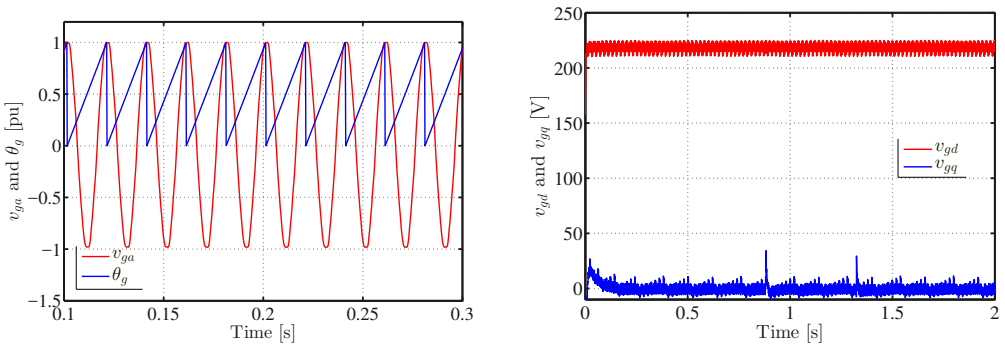

(a) (b)

Figure 6.2: Measurement of the grid voltage and the grid angle: (a) v_{gd}, and θ_g, in per unit and (b) d-axis and q-axis grid voltages.

In Figure 6.2(b), the d-axis and q-axis grid voltages are presented. It can be seen that the q-axis grid voltage is zero while the d-axis grid voltage is equal to the magnitude of the grid voltage space vector ($|\vec{v}_g| = v_{gd}$).

Once the grid angle is tracked, the grid side control strategy is activated. The performance of the grid side control strategy is displayed in Figure 6.3. The d-axis and q-axis grid currents, the three-phase grid current and the DC-link voltage are shown in Figure 6.3(a), Figure 6.3(b) and Figure 6.3(c), respectively. Once the SEW power converter is powered, the initial DC-link voltage is 540 V with the power switches not yet activated. The grid side control strategy is activated with the DC-voltage set to 600 V, as it can be seen from Figure 6.3(c). Hence, the d-axis grid current is increased in order to raise the DC link voltage from 540 V to 600 V as shown in Figure 6.3(a). Once the DC-link voltage reaches 600 V, the d-axis grid current is then reduced to a value that helps to maintain the DC-link voltage to 600 V. A similar surge can be seen in the three-phase grid current, as shown in Figure 6.3(b). On the other hand, the q-axis is maintained to zero to allow the GSC to operate under unity power factor, as shown in Figure 6.3(a).

Once the DC-link voltage reaches the reference DC-link voltage, the stator side control strategy can be activated. The performance of the stator side control strategies are discussed in Section 6.4 to Section 6.7.

The synchronisation process of the RDFIG system is conducted using synchronisation lights. The rotor voltage magnitude is adjusted by magnetising the stator side of the RDFIG using the q-axis stator current. Once all conditions for synchronisation are met, a switch helps in connecting the rotor side of the RDFIG to the grid. The performance of the proposed slip speed estimators for the sensor-less control of RDFIG-based WECSs is presented in the following sections.

Stellenbosch University https://scholar.sun.ac.za

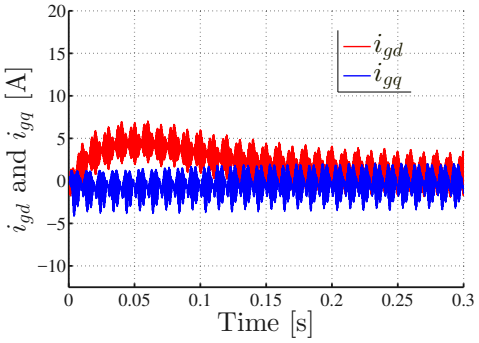

(a)

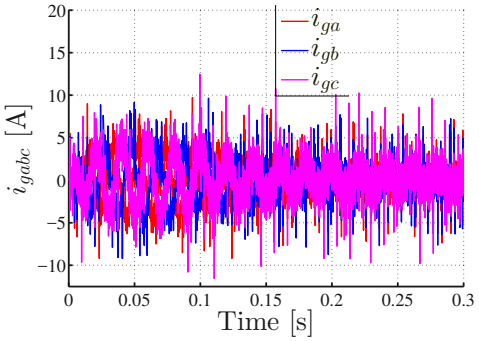

(b)

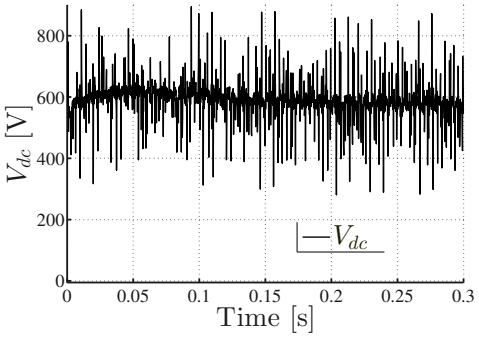

(c)

Figure 6.3: Measurement of the grid-side converter: (a) the d-axis and q-axis grid currents; (b) the three-phase grid current, and (c) the DC-link voltage.

6.4 PLL-based sliding mode observer for the sensor-less control of RDFIG systems

In this section, the experimental results of the proposed sensor-less control strategy based on the association of the SMO and the proposed PLL estimator are presented. The speed control of the RDFIG system is conducted. The slip speed estimator used in this section is composed of the SMO presented in Section 5.2 and the PLL estimator presented in Section 5.6. From the design

Stellenbosch University https://scholar.sun.ac.za

process presented in Section 5.2, the gains of the SMO are chosen as $n_1 = n_2 = 2000$ and the gains of the outer PI controller of the PLL estimator are $K_p = 240$ and $K_i = 14400$. Also, form the design process of the stator side control strategy presented in Chapter 4, the parameters of both inner PI controllers are $k_p = 35$ and $k_i = 500$ while those of the outer PI controller are $k_p = 0.2$ and $k_i = 20$.

6.4.1 Steady state performance

In Figure 6.4 and Figure 6.5, the performance of the proposed sensor-less control strategy during sub-synchronous operating conditions (speed of 219.8 rad/s) is presented. As shown in Figure 6.4(a), the estimated rotor speed closely matches the actual rotor speed and the rotor speed error is less than 1 rad/s as shown in Figure 6.4(b). The accuracy of the estimation is further demonstrated in Figure 6.4(c) and Figure 6.4(d), whereby the slip speed error is also found to be less than 1 rad/s. The actual and estimated slip angles are shown in Figure 6.5(a) while the slip angle error is shown in Figure 6.5(b). From Figure 6.5(a) and Figure 6.5(b), a marginal slip angle error below 0.1 rad (5.73°) is shown which demonstrate the effectiveness of the proposed sensor-less control strategy, under sub-synchronous operating conditions.

Similar performance characteristics are observed under super-synchronous operating conditions, as shown in Figure 6.6 and Figure 6.7. In fact, in Figure 6.6, the performance of the proposed sensor-less control strategy at super-synchronous speed (346 rad/s) is presented. It can be seen that the maximum value of the rotor angular speed error is less that 1 rad/s. The estimated and the real slip speeds and the slip speed error are shown in Figure 6.6(c) and Figure 6.6(d), respectively. One can notice the same pattern in Figure 6.6(d). The real and the estimated slip angle are shown in Figure 6.7(a). It can be seen that the real and estimated slip angles converge perfectly. On the other hand, the slip angle error is shown in Figure 6.7(b). It can be seen that at this particular operating conditions the slip angle error is less than 0.1 rad (0.1 rad is equivalent to 5.73 °).

6.4.2 Transient performance under varying rotor angular speed

In Figure 6.8, the performance of the proposed control strategy is shown during a gradual increase in rotor speed from sub-synchronous operating conditions to super-synchronous operating conditions (from 282 rad/s to 355 rad/s). The actual and the estimated angular rotor speeds, the real and estimated slip speeds and the slip speed error are shown in Figure 6.8(a), Figure 6.8(b) and Figure 6.8(c), respectively. It can be observed that the error throughout the

Stellenbosch University https://scholar.sun.ac.za

speed transition is less than 2.5 rad/s (11.95 rpm) while at constant speed conditions the slip error is almost zero, as shown Figure 6.8(c).

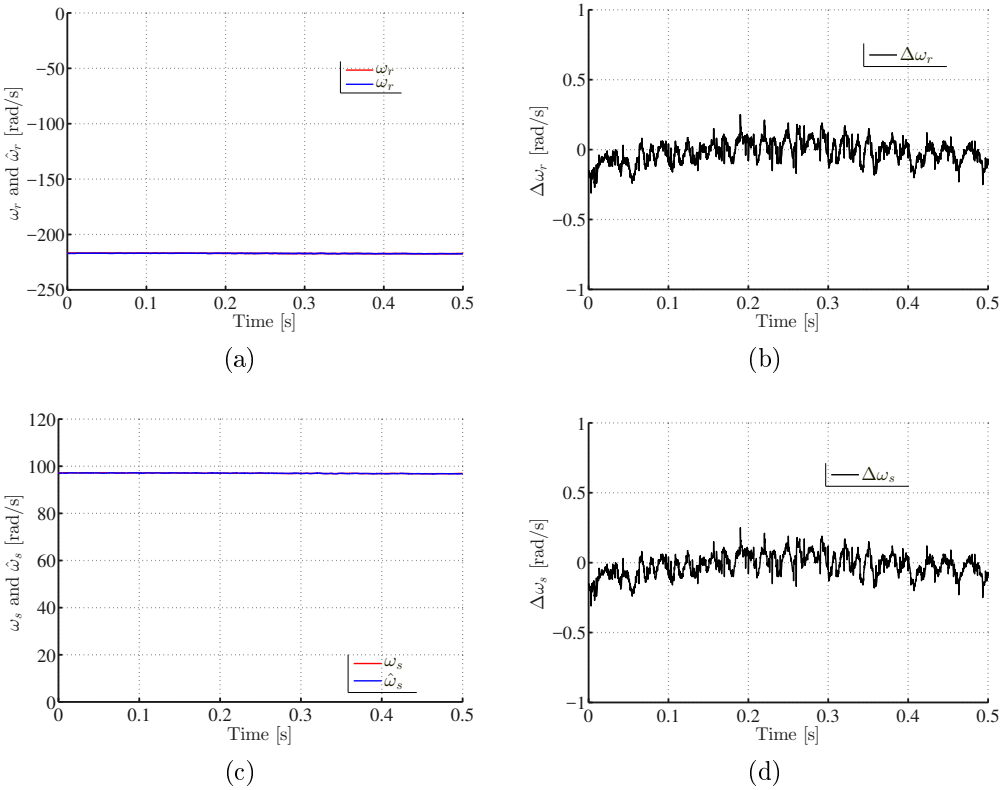

Figure 6.4: Experimental results during sub-synchronous operating conditions with the reference speed $\omega_r^\star$=-219 rad/s: (a) the measured and estimated electrical rotor speeds; (b) the electrical rotor speed error; (c) the estimated and the actual slip speeds; (d) and, the slip speed error.

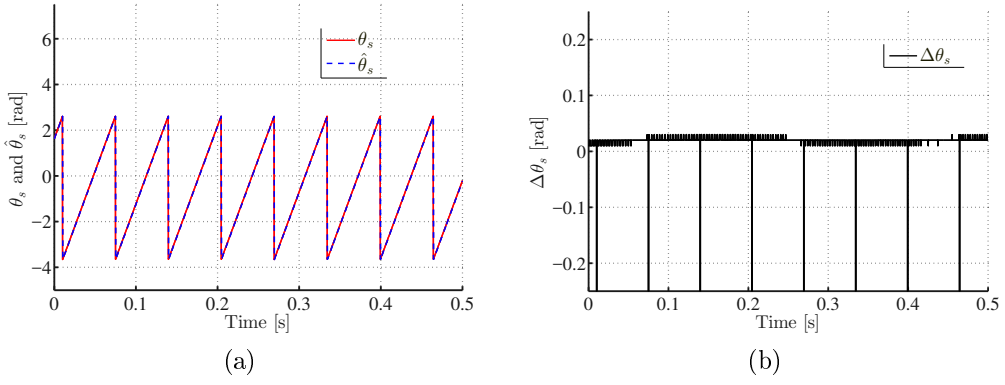

Figure 6.5: Experimental results during sub-synchronous operating conditions with the reference speed $\omega_r^\star$=-219 rad/s: (a) the estimated and the actual slip angles, and (b) the slip angle error.

Stellenbosch University https://scholar.sun.ac.za

The performance of the proposed sensor-less control strategy during rotor

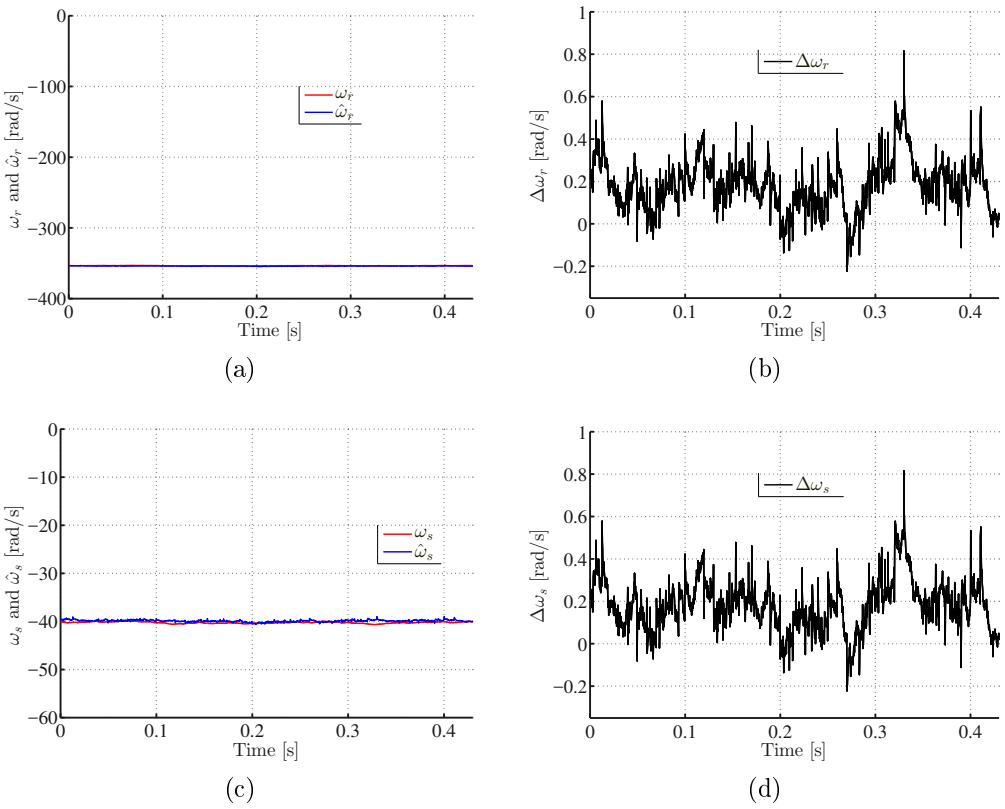

Figure 6.6: Experimental results during super-synchronous operating conditions with the reference speed $\omega_r^\star$=- 346 rad/s: (a) the measured and estimated electrical rotor speeds; (b) electrical rotor speed error; (c) the estimated and the actual slip speeds; (d) and, the slip speed error.

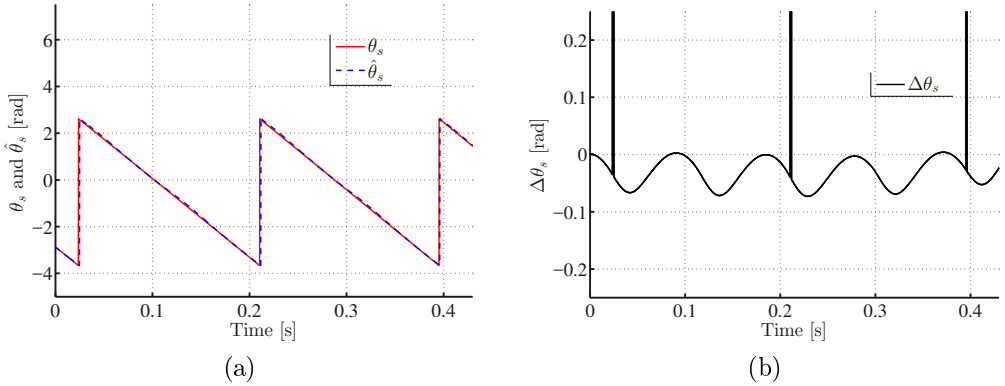

Figure 6.7: Experimental results during super-synchronous operating conditions with the reference speed $\omega_r^\star$=- 346 rad/s: (a) the estimated and the actual slip angles, and (b) the slip angle error.

Stellenbosch University https://scholar.sun.ac.za

speed transition from super-synchronous to sub-synchronous operating conditions is shown in Figure 6.9. The estimated and the measured rotor speeds are shown in Fig 6.9(a). It can be seen that the estimated rotor angular speed closely tracks the actual rotor speed. The actual and the estimated slip angular speeds are shown in Figure 6.9(b) from which a similar pattern can be noticed, as in Figure 6.9(a). Similar to Figure 6.8(c), the slip speed error is less than 2.5 rad/s as shown in Figure 6.9(c).

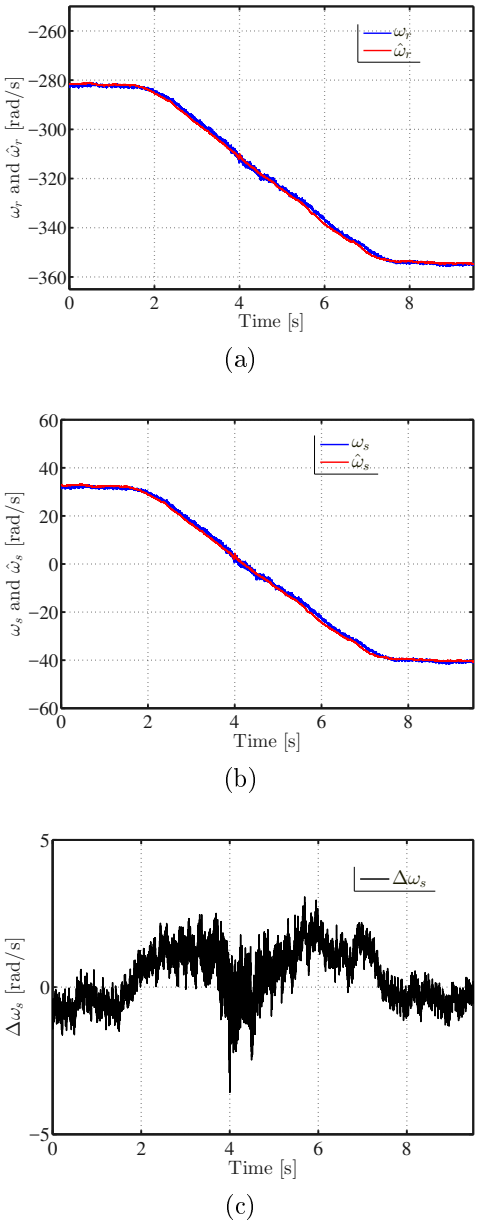

Figure 6.8: Experimental results during change in rotor speed from sub-synchronous to super-synchronous operating conditions: (a) the measured and estimated rotor speed; (b) the measured and the estimated slip speed; and (c) the slip speed error.

Stellenbosch University https://scholar.sun.ac.za

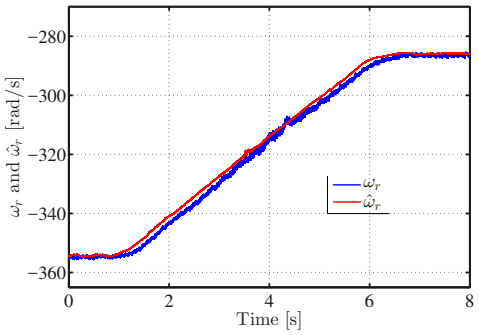

(a)

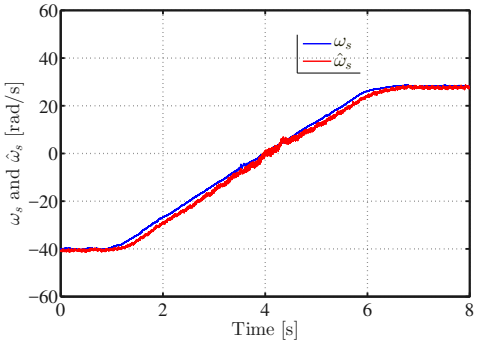

(b)

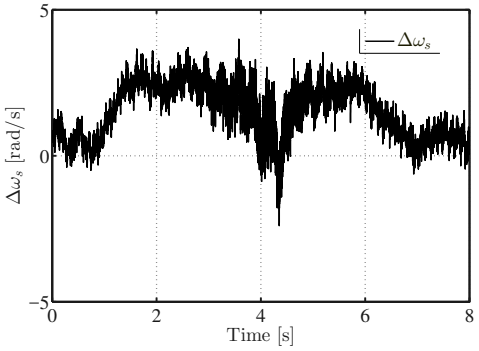

(c)

Figure 6.9: Experimental results during change in rotor speed from super-synchronous to sub-synchronous operating conditions: (a) the measured and estimated rotor speed; (b) the measured and the estimated slip speed; and (c) the slip speed error.

6.4.3 Transient performance during sudden changes in the stator current magnitude

The performance of the proposed slip speed estimator for the sensor-less control strategy during changes in stator current magnitude from 1.7 A to 4 A and then from 4 A to 1.7 A, is shown in Figure 6.10 and in Figure 6.11. The d-axis and q-axis stator currents are shown in Figure 6.10(a) while the corresponding

Stellenbosch University https://scholar.sun.ac.za

effect on the three-phase stator currents is shown in Figure 6.10(b). It can be seen that at t = 1 s the d-axis stator current is kept at zero while the magnitude of the q-axis stator current is step increased to 4 A. At t = 5.8 s, the q-axis stator current magnitude is reduced to its original value of 1.7 A. The estimated and actual rotor speed are shown in Figure 6.10(c) and the rotor speed error is shown in Figure 6.10(d). It can be seen from Figure 6.10(d) that at about t = 1 s the maximum error is about 4 rad/s and at t = 5.8 s the same maximum error can be seen and this corresponds to the same instances when the magnitude of the q-axis current is changed. A similar patter can be seen from Figure 6.11 with regards to the slip speed error.

6.4.4 Transient performance under inaccurate machine parameters

In Figure 6.12, the performance of the proposed control strategy is evaluated when considering changes in rotor speed whilst having an inaccurate stator inductance valued at 1.3 times the stator actual inductance. The slip speed

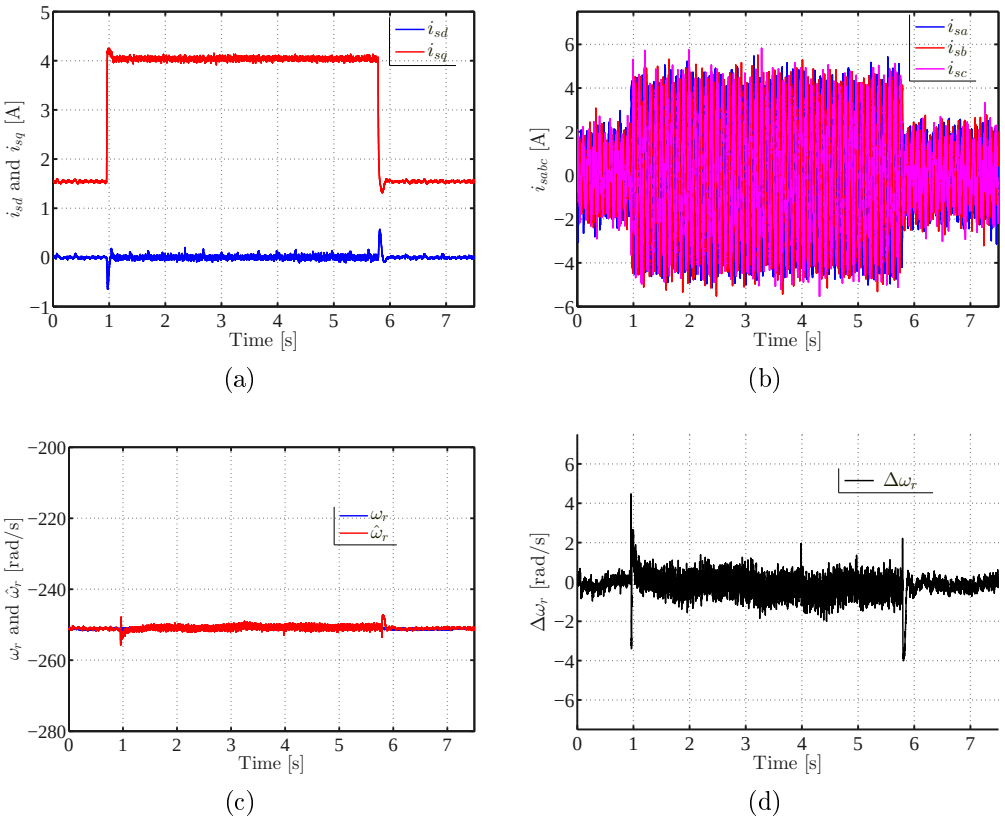

Figure 6.10: Experimental results during changes in stator current magnitude: (a) the d-axis and q-axis stator current; (b) the three-phase stator current; (c) the measured and estimated electrical rotor speeds; (d) the electrical rotor speed error.

Stellenbosch University https://scholar.sun.ac.za

error is shown in Figure 6.13(b), where it can be seen that during the changes in slip speed the maximum slip error is less than 4 rad/s. Also, during steady operating conditions the slip error is almost zero.

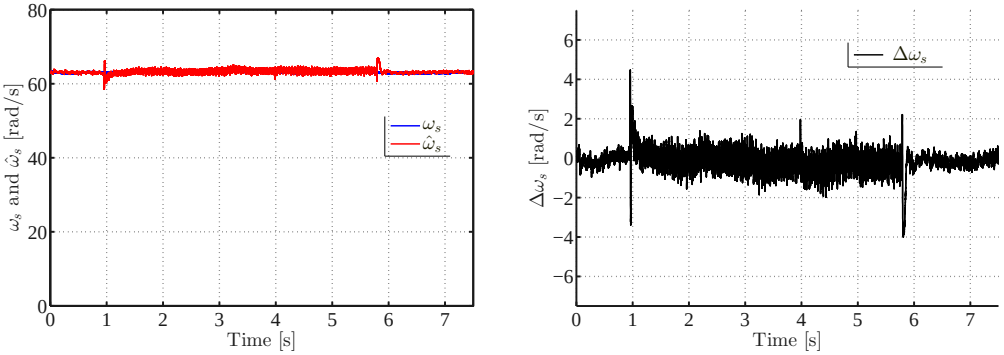

(a) (b)

Figure 6.11: Experimental results during changes in stator current magnitude: (a) the estimated and the actual slip speeds, and; (b) the slip speed error.

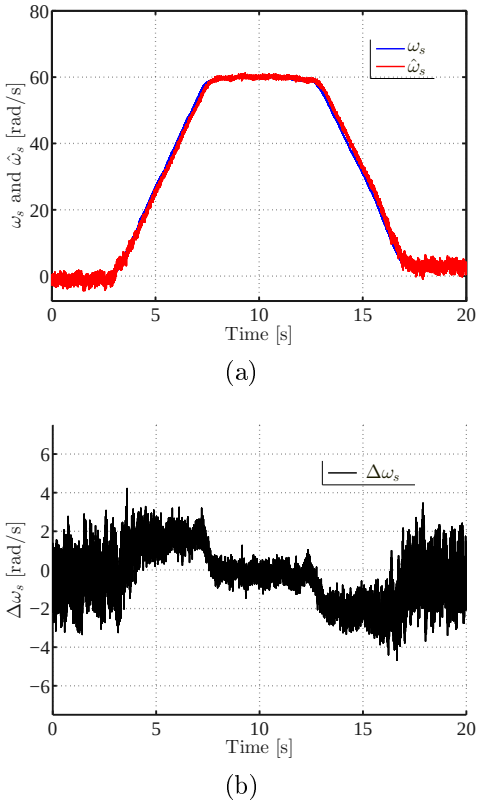

(a)

(b)

Figure 6.12: Experimental results during change in rotor speed from synchronous to sub-synchronous operating conditions with inaccurate stator inductance $1.3L_s$: (a) the measured and estimated slip speed; (b) the slip speed error.

Stellenbosch University https://scholar.sun.ac.za

In Figure 6.13, the performance of the proposed control strategy is further evaluated under changes in rotor speed whilst having an inaccurate stator inductance and also inaccurate stator resistance. From Figure 6.13(b), it can be seen that the maximum slip error is 3 rad/s. The performances shown in Figure 6.13 and Figure 6.12 validate the robustness of the proposed control strategy against parameter variations.

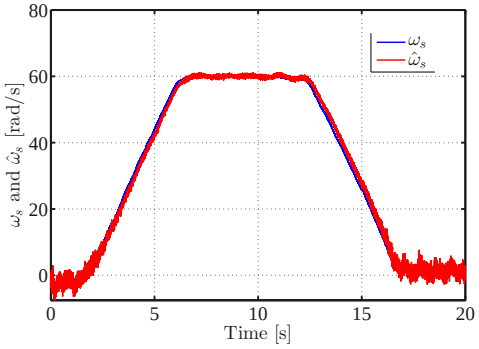

(a)

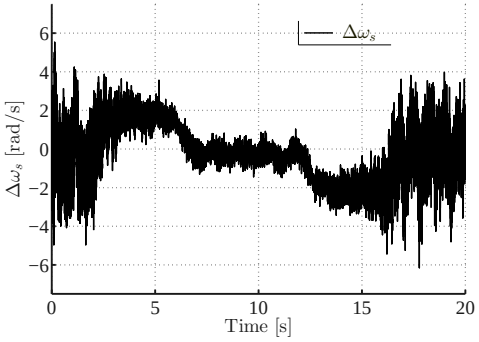

(b)

Figure 6.13: Experimental results during change in rotor speed from synchronous to sub-synchronous operating conditions with inaccurate stator inductance $1.3L_s$ and stator resistance $1.3R_s$: (a) the measured and estimated slip speed; (b) the slip speed error.

6.4.5 Transient performance under steady changes rotor speed

In Figure 6.14, the performance of the proposed sensor-less control strategy is presented during a change in speed from sub-synchronous to super-synchronous operating conditions as shown in Figure 6.14(a). From Figure 6.14(b), it can be seen that at about t = 1 s, the frequency at which the three-phase stator currents pulsate at almost 0 Hz. Furthermore, it can also be seen from Figure 6.14(a) that the slip angular speed approaches zero at t = 1 s. Also, it can

Stellenbosch University https://scholar.sun.ac.za

be clearly seen that at super-synchronous operating conditions the sequence of the three-phase stator current has reversed.

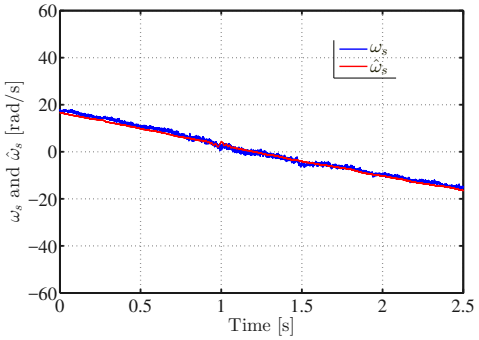

(a)

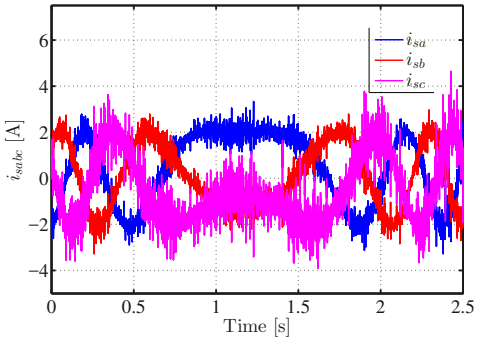

(b)

Figure 6.14: Experimental results during change in rotor speed from super-synchronous to sub-synchronous operating conditions: (a) the measured and estimated slip speed; (b) the three-phase stator current.

6.5 PLL-based adaptive sliding mode observer estimator for the sensor-less control of RDFIG systems

In this Section, the experimental results of the sensor-less control strategy based on the association of the ASMO and the PLL estimator are presented and analysed. The speed control is adopted for the stator side control strategy. The PI gains of the stator side control strategy and those of the PLL estimator are the same as those chosen in Section 6.4. From the design of the ASMO gains presented in Section 5.3, the gains of the ASMO are chosen as $d = 200$, $\gamma_0 = 1$, $\gamma_1 = 1$ and $p = 1$.

Stellenbosch University https://scholar.sun.ac.za

6.5.1 Steady state performance

In Figure 6.15, the effectiveness of the sensor-less control strategy based on the ASMO estimator during sub-synchronous operating conditions with the RDFIG running at -900 rpm is presented. The estimated slip speed and the actual slip speed converge, as shown in Figure 6.15(a), while the same pattern can be observed between the estimated slip angle and the actual slip angle from Figure 6.15(c). In Figure 6.15(b), it can be seen that the slip speed error is very small and from Figure 6.15(d), it is observed that the slip speed error is negligible.

In Figure 6.16, the effectiveness of the ASMO estimator during super-synchronous operating conditions with the RDFIG running at -1650 rpm is presented. It is observed that the estimation error is very small.

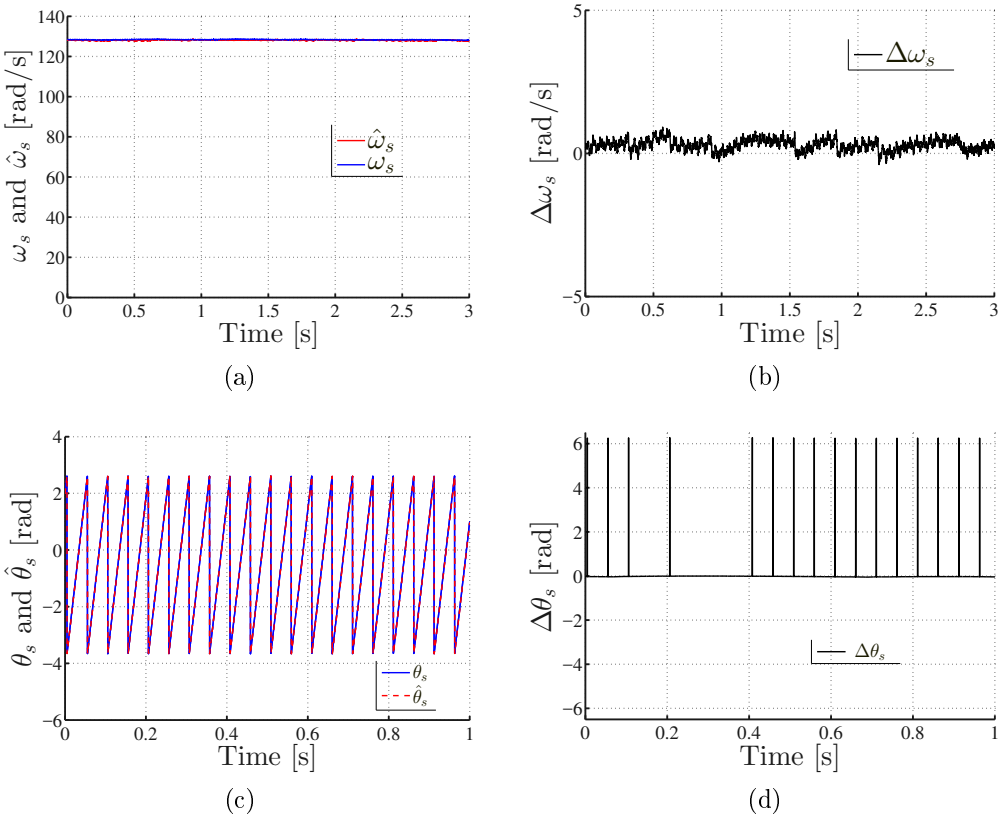

Figure 6.15: The performance of the ASMO during sub-synchronous operating conditions: (a) The measured slip speed, ω_s and estimated slip speed, $\hat{\omega}_s$; (b) The slip speed error, $\Delta\omega_s$; (c) The measured slip angle, θ_s and the estimated slip angle, $\hat{\theta}_s$; and (d) The slip angle error, $\Delta\theta_s$.

Stellenbosch University https://scholar.sun.ac.za

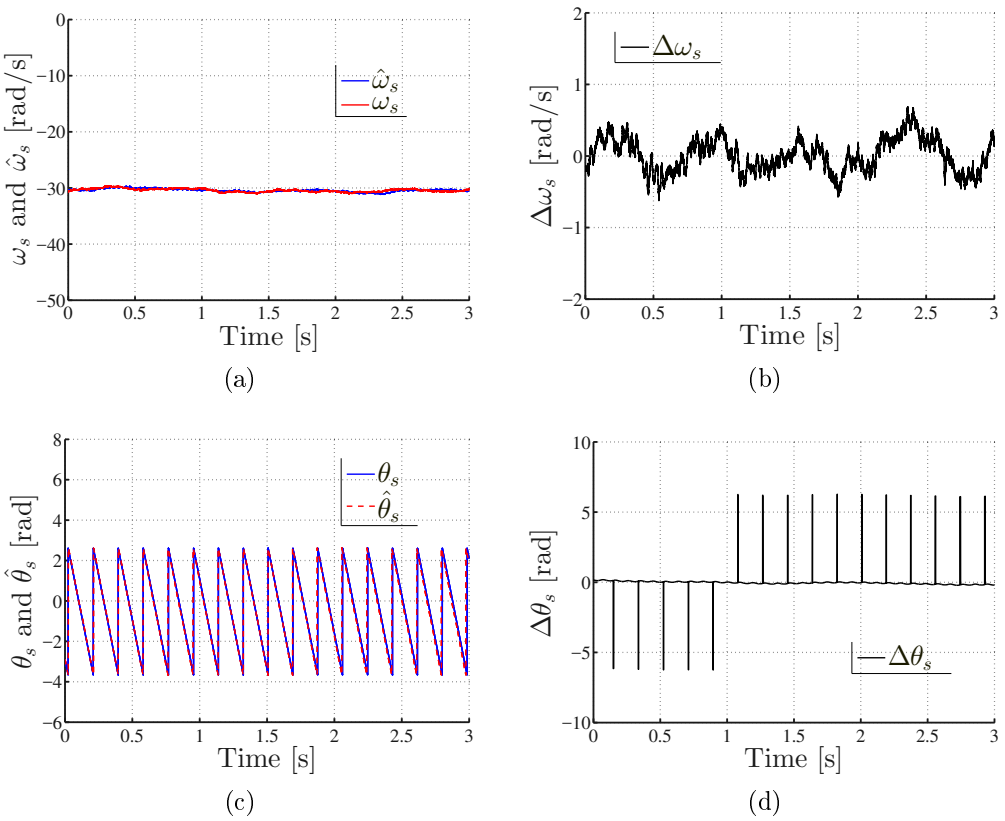

Figure 6.16: The performance of the ASMO during super-synchronous operating conditions: (a) The measured slip speed, ω_s and estimated slip speed, $\hat{\omega}_s$; (b) The slip speed error, $\Delta\omega_s$; (c) The measured slip angle, θ_s and the estimated slip angle, $\hat{\theta}_s$; and (d) The slip angle error, $\Delta\theta_s$.

6.5.2 Performance under rotor speed transition

The robustness of the proposed sensor-less control strategy based on the association of the ASMO and PLL estimator during a change in rotor speed is presented in Figure 6.17. During the speed transitions, from t = 0 s to t = 5 s, and from t = 38 s to t = 45 s, it can be seen that the actual and estimated slip speeds coincide as in Figure 6.17(a), while in Figure 6.17(b), the slip speed error is very small. From Figure 6.17(b), it can be seen that the maximum slip speed error is 2.5 rad/s.

In Figure 6.18, the performance of the proposed control strategy during speed transition when considering inaccurate machine parameters (resistance and inductance) is shown. From Figure 6.17 and Figure 6.18, the same controller performance pattern can be observed. Even though the increase in the chattering effect is clearly shown, the presented performance demonstrates that the proposed control strategy is immune to parameter variations.

Stellenbosch University https://scholar.sun.ac.za

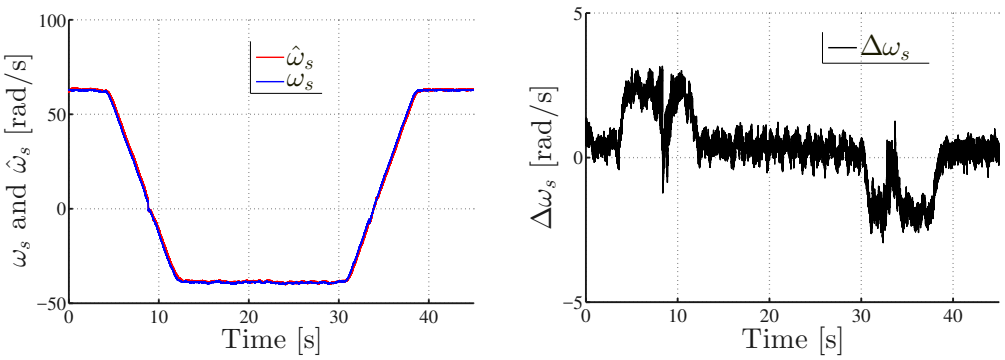

(a) (b)

Figure 6.17: The transient performance of the proposed control strategy during speed transition: (a) The measured slip speed, ω_s and estimated slip speed, $\hat{\omega}_s$ and (b) The slip speed error, $\Delta\omega_s$.

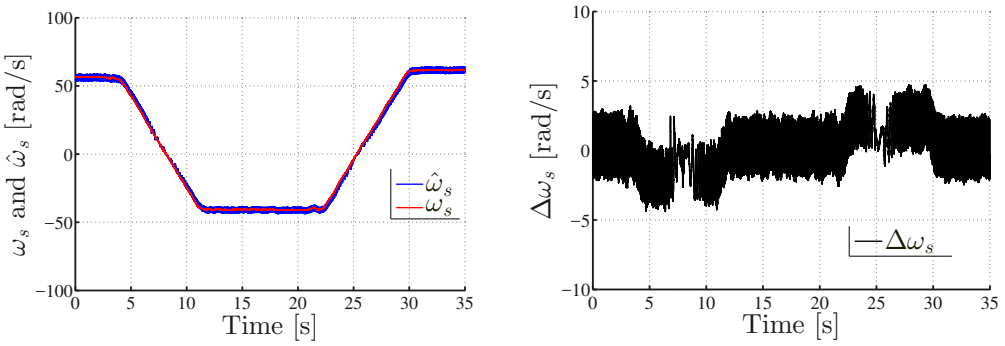

(a) (b)

Figure 6.18: The transient performance during change in speed with inaccurate machine parameters ($1.3L_s$ and $1.3R_s$): (a) The measured slip speed, ω_s and estimated slip speed, $\hat{\omega}_s$; and (b) The slip speed error, $\Delta\omega_s$.

6.5.3 Performance under sudden changes in the stator current magnitude

In Figure 6.19, the performance of the proposed slip speed estimator for the sensor-less control strategy is presented. In this experiment, the RDFIG is rotating at 1050 rpm which is equivalent to about 92 rad/s of the slip speed, as shown in Figure 6.19(a). Between t=0 s and t=0.8 s, it can be seen that the actual and estimated slip speed are aligned perfectly during steady operating conditions. And, the slip speed error is close to zero, as shown in Figure 6.19(b).

At about t=0.8 s, a sudden increase in the stator current magnitude, as shown in Figure 6.19(c). The maximum slip speed error for the ASMO estimator is less than 10 rad/s, and is satisfactory. Also, during the stator current

Stellenbosch University https://scholar.sun.ac.za

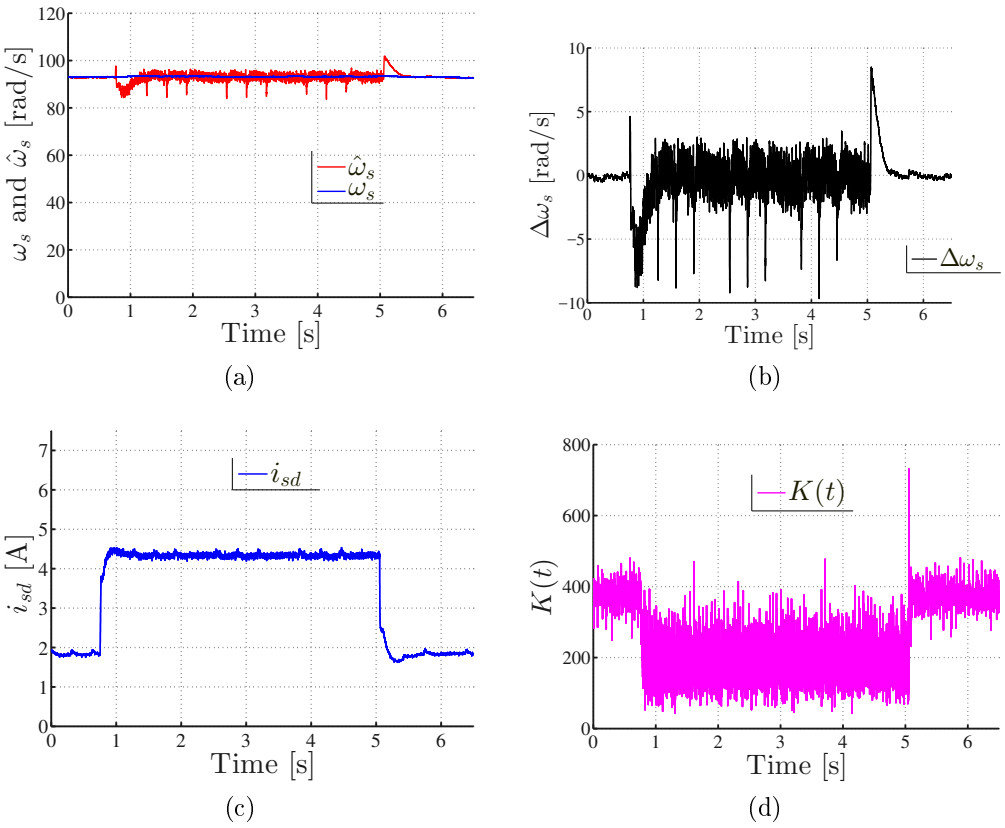

Figure 6.19: The transient performance during change in stator current magnitude: (a) The actual slip speed, ω_s and the estimated slip speed, $\hat{\omega}_s$; (b) The slip speed error, $\Delta\omega_s$; (c) The d-axis stator current, i_{sd}; and (d) The adaptive gain, $K(t)$.

change, it can be seen that the adaptive gain is adjusted on-line in order to reduce the chattering effect, as it can be seen in Figure 6.19(d). However, it can be seen that the slip speed waveform includes spikes which are mostly due to the fact that the adaptive gain is a function of the sliding surface. Although, the PLL-based ASMO estimator is very sensitive to the dynamics of the stator current the spikes in the slip speed waveform does not affect the sensor-less operations. At about t=5.2 s, the stator current magnitude is decreased to its initial value. The adaptive gain is also adjusted on-line, as shown in Figure 6.19(d).

6.5.4 Performance in rotor speed changes

In Figure 6.20, the performance of the sensor-less control strategy is presented during change in speed from super-synchronous to sub-synchronous operating conditions. The estimated and actual slip speeds, the slip speed error and the phase A and phase B stator currents, are displayed in Figure 6.20(a), Figure 6.20(b) and Figure 6.20(c), respectively. From Figure 6.20(a), it can be seen that the estimated slip speed tracks the actual slip speed during

Stellenbosch University https://scholar.sun.ac.za

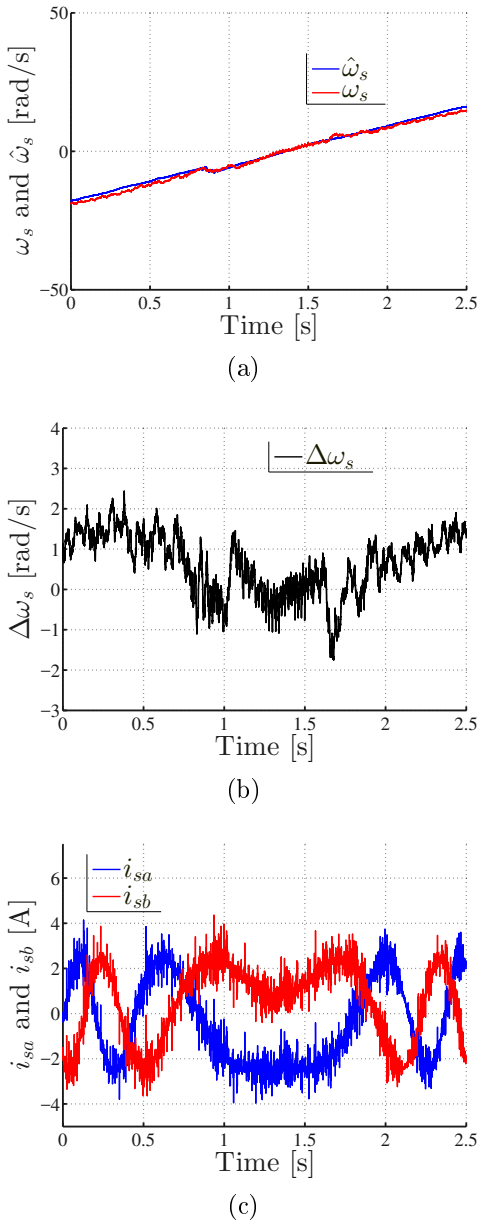

Figure 6.20: The performance during change from super-synchronous to sub-synchronous operating conditions: (a) The actual slip speed, ω_s and the estimated slip speed$\hat{\omega}_s$; (b) The slip speed error $\Delta\omega_s$; and (c) i_{sa} and i_{sb}.

the change of operating conditions. The maximum slip speed error during the recorded sensor-less operation is 2.5 rad/s, as displayed in Figure 6.20(b). Also, at t=1.35 s, the slip speed error is close to zero because both the estimated and actual speeds are close to zero, as shown in Figure 6.20(b). At the same time, it is also shown that the stator current becomes almost DC in Figure 6.20(c). From, Figure 6.20(c) a change in current sequence can be observed as the sign of slip speed also changes.

Stellenbosch University https://scholar.sun.ac.za

6.6 PLL-based super-twisting sliding mode observer estimator for the sensor-less control of RDFIG systems

In this section, the experimental results on the sensor-less control strategy for the RDFIG system, that is based on the association of the STSMO with the PLL estimator is presented. Here, the power control is adopted of the stator side control strategy. The proposed sensor-less control strategy is discussed in Chapter 4. The parameters of the STSMO gains are chosen to be $k_1 = k_3 = 5000$ and $k_2 = k_4 = 250$. The PLL gains are similar to those chosen in Section 6.4. The parameters of both PI controllers of the inner control loop are $k_p = 35$ and $k_i = 500$, while those of the outer control loop are $k_p = 0.03$ and $k_i = 0.737$, respectively.

6.6.1 Steady state performance

In Figure 6.21 and Figure 6.22, the measurement results showing the effectiveness of the proposed sensor-less control strategy during sub-synchronous operating conditions are given. It can be seen that the estimated values of the angular rotor speed, slip speed and slip angle are very close to their corresponding measured values.

In Figure 6.23 and Figure 6.24, the performance of the proposed control strategy is shown during super-synchronous operating conditions with the rotor running at -345.4 rad/s (corresponding to -1650 rpm), as shown in Figure 6.23(a). It can be seen from the figure that the estimated angular rotor speed, slip speed and slip angle closely matches their corresponding actual values.

6.6.2 Performance under varying rotor angular speed

In Figure 6.25, the performance of the proposed sensor-less control strategy is presented during a gradual decrease in speed from super-synchronous operating conditions to sub-synchronous operating conditions (from -350 rad/s to -219.8 rad/s). The estimated and actual slip angular speeds are shown in Figure 6.25(b) while the slip speed error is shown in Figure 6.25(c). It can be seen from Figure 6.25(c) that during the steady state operating conditions (in both super-synchronous and sub-synchronous operating conditions), the slip speed error averages at zero while during the speed transition, the maximum slip speed error averages above zero but less than 2 rad/s (which is equivalent to about 9.55 rpm). It is worth noticing that at synchronous operating conditions, and with a slip speed of zero, the proposed PLL-based STSMO performs well with a slip speed error of about zero as shown in Figure 6.25(c).

Stellenbosch University https://scholar.sun.ac.za

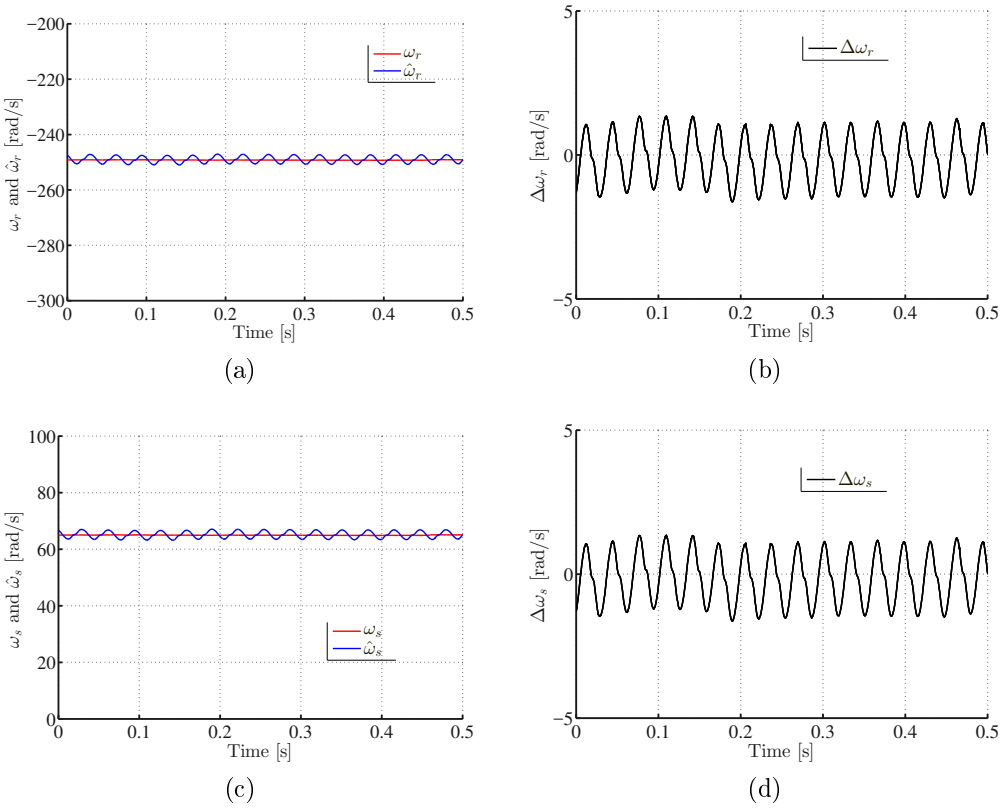

Figure 6.21: Experimental results during sub-synchronous operating conditions (ω_r =-248.8 rad/s): (a) ω_r and $\hat{\omega}_r$; (b) the rotor speed error, $\Delta\omega_r$; (c) ω_s and $\hat{\omega}_s$; (d) the slip speed error, $\Delta\omega_s$;

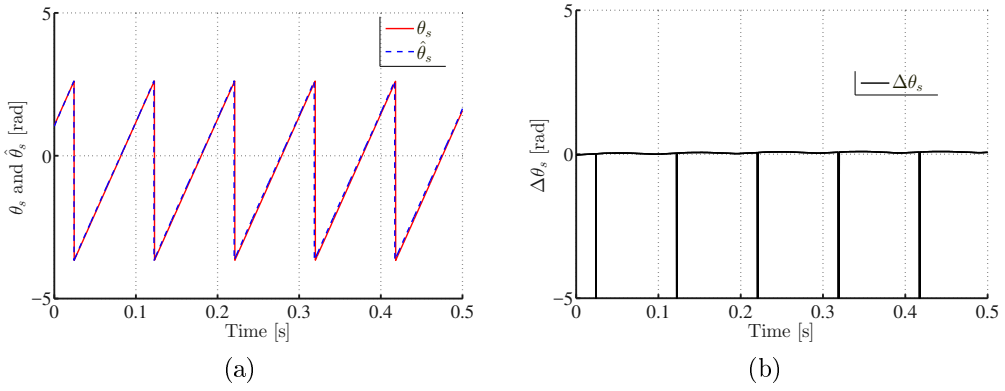

Figure 6.22: Experimental results during sub-synchronous operating conditions (ω_r =-248.8 rad/s): (a) θ_s and $\hat{\theta}_s$, and (b) the slip angle error, $\Delta\theta_s$.

The effectiveness of the proposed control strategy during a speed transition from sub-synchronous to super-synchronous operating conditions (from -219.8 rad/s to -350 rad/s) is shown in Figure 6.26. The estimated and actual

Stellenbosch University https://scholar.sun.ac.za

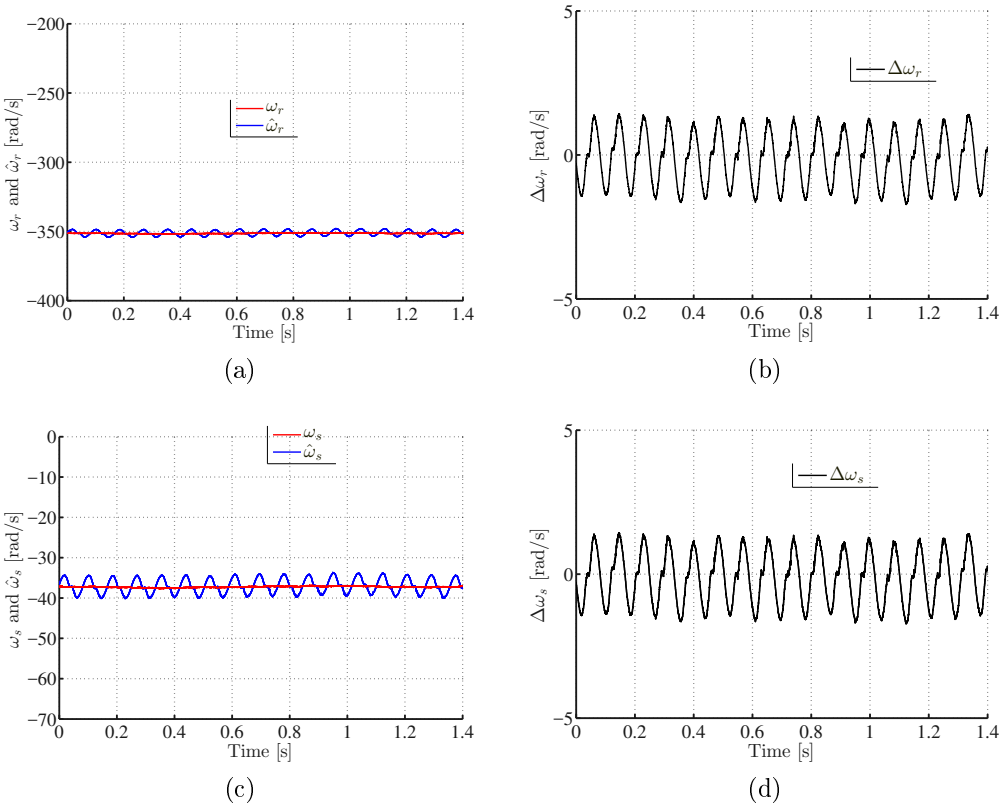

Figure 6.23: Experimental results during super-synchronous operating conditions (ω_r =-345.4 rad/s): (a) ω_r and $\hat{\omega}_r$; (b) the rotor speed error, $\Delta\omega_r$; (c) ω_s and $\hat{\omega}_s$; (d) the slip speed error, $\Delta\omega_s$;

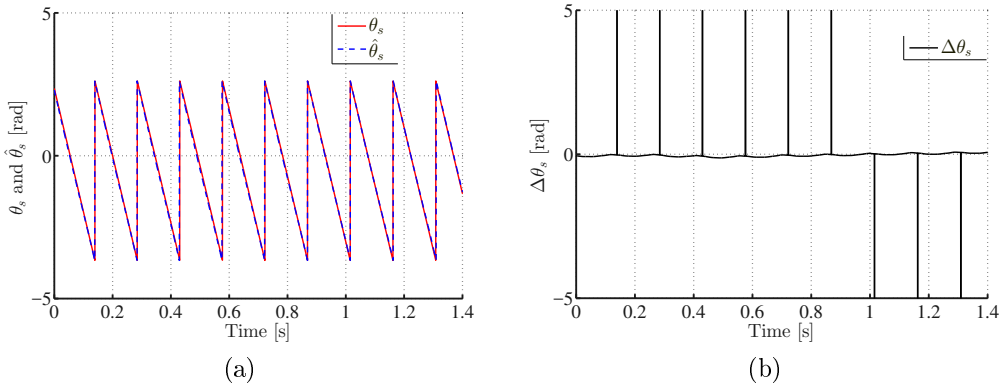

Figure 6.24: Experimental results during super-synchronous operating conditions (ω_r =-345.4 rad/s): (a) θ_s and $\hat{\theta}_s$, and (b) the slip angle error, $\Delta\theta_s$.

rotor angular speeds are shown in Figure 6.26(a) while the estimated and actual slip angular speeds are displayed in Figure 6.26(b). From Figure 6.26(a) and Figure 6.26(b), it can be seen that all the estimated quantities compare

Stellenbosch University https://scholar.sun.ac.za

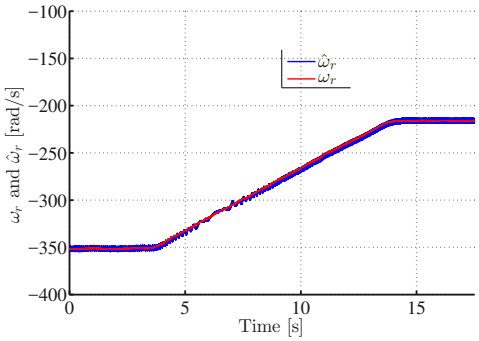

(a)

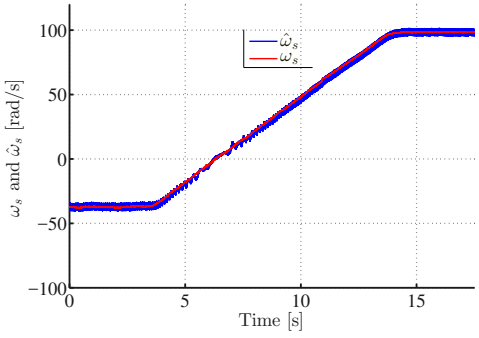

(b)

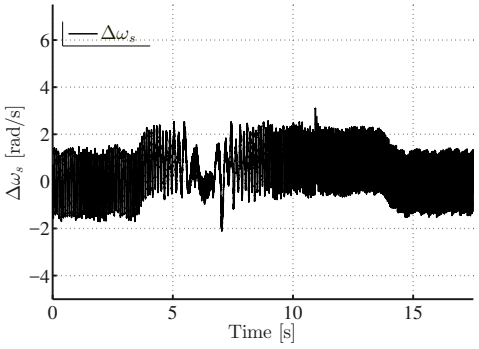

(c)

Figure 6.25: Experimental results during variation in rotor speed from super-synchronous synchronous to sub-synchronous operating conditions (from -350 rad/s to -219.8 rad/s): (a) ω_r and $\hat{\omega}_r$; (b) ω_s and $\hat{\omega}_s$; and (c) $\Delta\omega_s$.

very well with the actual quantities. In Figure 6.26(c), the slip speed error is shown. It can be seen that,during the transition in speed, the maximum slip speed error is -2 rad/s while it is zero during the steady state operating conditions. It is worth noticing that at synchronous operating conditions, the slip speed is zero, the proposed PLL-based STSMO performs well with a slip speed error of about zero as shown in Figure 6.26(c).

Stellenbosch University https://scholar.sun.ac.za

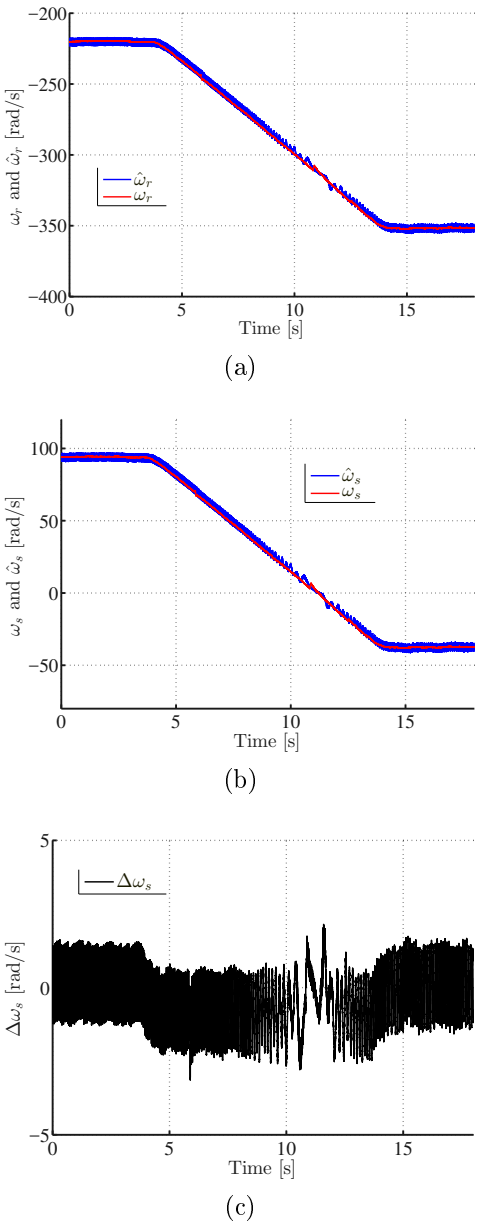

Figure 6.26: Experimental results during variation in rotor speed from sub-synchronous synchronous to super-synchronous operating conditions (from -219.8 rad/s to -350 rad/s): (a) ω_r and $\hat{\omega}_r$; (b) ω_s and $\hat{\omega}_s$; and (c) $\Delta\omega_s$.

6.6.3 Performance during sudden changes of the stator current magnitude

In Figure 6.27, the measurement results of the proposed sensor-less control strategy during changes in the stator current magnitude from 1.7 A to 4.1 A and from 4.1 A to -1.7 A, with the rotor rotating at -1200 rpm, are shown. It can be seen that the maximum slip speed error during the stator current

Stellenbosch University https://scholar.sun.ac.za

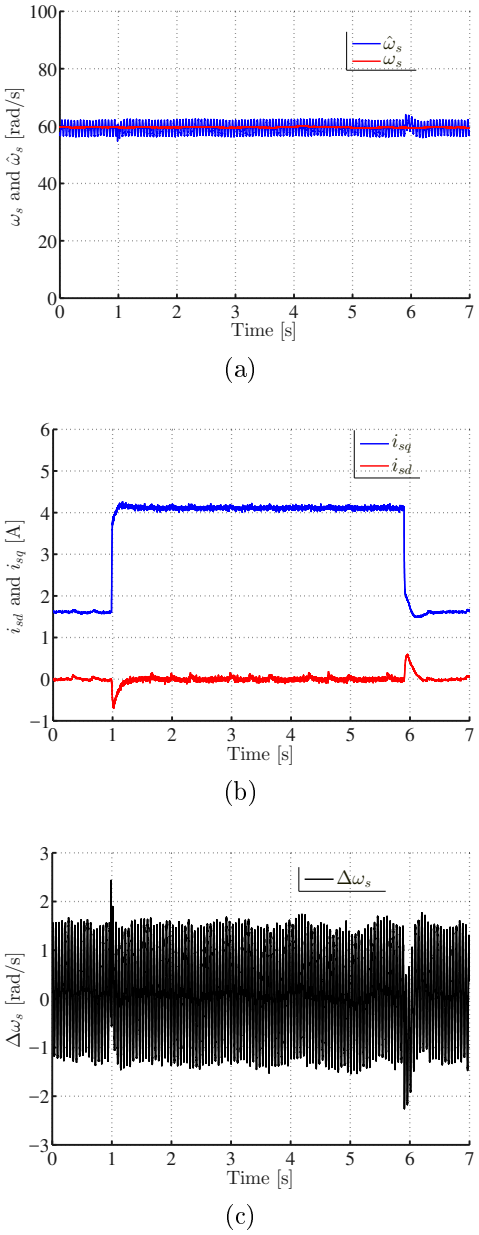

Figure 6.27: Experimental results during changes in the stator current magnitude from 1.7 A to 4.1 A and from 4.1 A to -1.7 A (with the rotor rotating at -1214 rpm): (a) ω_s and $\hat{\omega}_s$; (b) i_{sd} and i_{sq}; and (c) $\Delta\omega_s$.

magnitude changes is 2.5 rad/s at t=1 s and t=6 s while the slip speed error is zero during constant stator current magnitude, as shown in Figure 6.27(c).

6.6.4 Performance under machine parameter variations

The robustness of the proposed sensor-less control strategy under parameter variations is presented in Figure 6.28 and Figure 6.29. In Figure 6.28, the re-

Stellenbosch University https://scholar.sun.ac.za

sults of the proposed control strategy when tested during a gradual speed change (with change in slip speed from 94 rad/s to 30 rad/s) with an inaccurate inductance of 1.3 L_s, are shown. It can be seen that, during the speed change, the maximum slip speed error is less than 2.5 rad/s while at steady state operating conditions, the slip speed error averages at zero as shown in Figure 6.28(b) which is a proof that the proposed control strategy is immune to parameter variations.

In Figure 6.29, the effectiveness of the proposed control strategy is shown during a change in rotor speed (with change in slip speed from 94 rad/s to 30 rad/s) with both inaccurate stator inductance and stator resistance. It can be seen that during the speed change, the maximum slip speed error is less than 2.5 rad/s while at steady state operating conditions, the slip speed error averages at zero as shown in Figure 6.28(b) which is evidence that the proposed control strategy is robust to parameter variations.

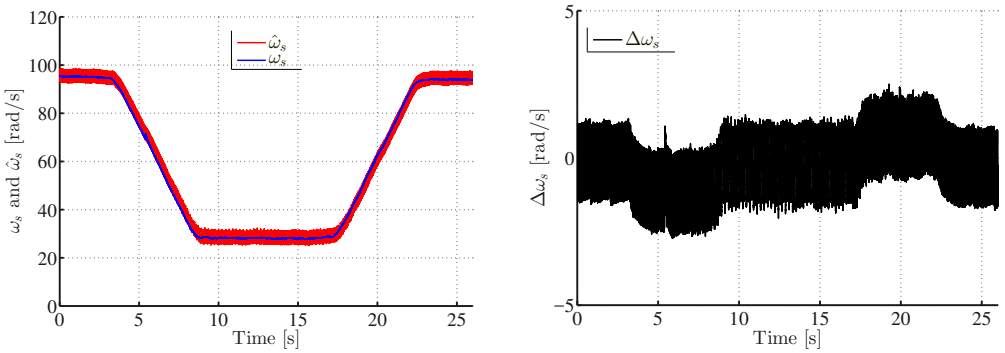

(a) (b)

Figure 6.28: Experimental results during a change in rotor speed with inaccurate stator inductance at 1.3 L_s: (a) ω_s and $\hat{\omega}_s$; and, (b) $\Delta\omega_s$.

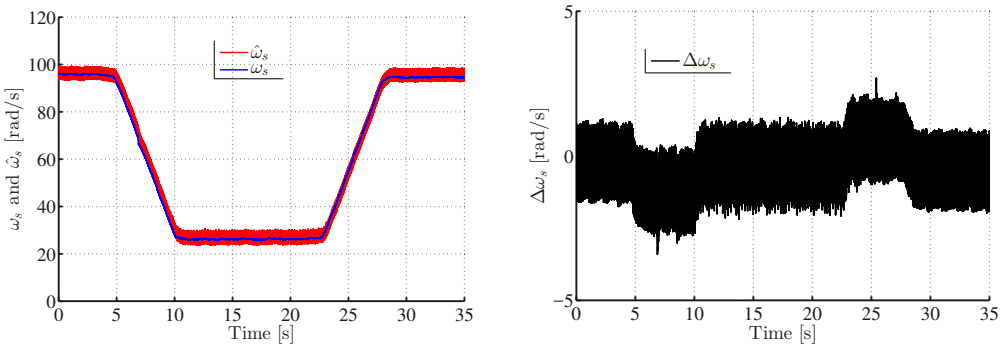

(a) (b)

Figure 6.29: The experimental results during a change in rotor speed with inaccurate stator inductance $1.3L_s$ and stator resistance $1.3R_s$: (a) ω_s and $\hat{\omega}_s$; and, (b) $\Delta\omega_s$.

Stellenbosch University https://scholar.sun.ac.za

6.6.5 Performance under varying rotor angular speed

The performance of the proposed slip speed estimator for sensor-less control strategy during a gradual change in rotor speed from super-synchronous operating condition to sub-synchronous operating conditions is shown in Figure 6.30. In Figure 6.30(a), the estimated and actual slip speeds are shown. It can be seen that the estimated slip speed tracks the actual slip speed in all the operating conditions. In Figure 6.30(b), the phase A and Phase B stator currents are shown. The phase sequence changes when the machine operates from super-synchronous operating conditions to sub-synchronous operating conditions can be seen from the figure.

6.6.6 Performance under sudden changes in rotor active power

In Figure 6.31, the effectiveness of the proposed control strategy is presented with the rotor rotating at -1200 rpm (which is equivalent to $\hat{\omega}_s$ =60 rad/s). At t=3.8 s, the active power output at the rotor side is changed from -2000 W to -2600 W while the reactive power output at the rotor side remains constant at 1300 VAR, as shown in Figure 6.31(c). At this instance, the slip speed error averages at zero, as shown in Figure 6.31(b) and the magnitude of the stator current is increased up to 5.1 A, as shown in Figure 6.31(d). At t=11.1 s, the active power output at the rotor side is decreased suddenly to -800 W while the reactive power output is still kept at 1300 VAR, as shown in Figure 6.31(c). As a consequence, the stator current magnitude also drops suddenly to 2 A, as shown in Figure 6.31(d) while the maximum slip speed error is less than 3 rad/s, as shown in Figure 6.31(b).

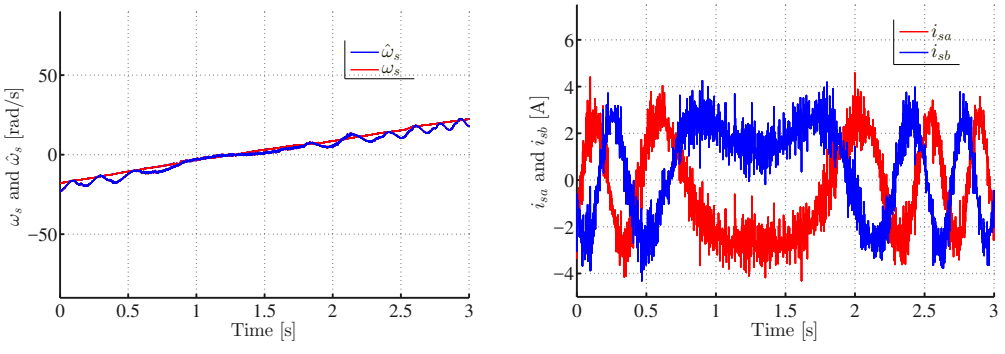

Figure 6.30: The transient performance during change from super-synchronous to sub-synchronous operating conditions: (a) ω_s and $\hat{\omega}_s$, and (b) i_{sa} and i_{sb}.

Stellenbosch University https://scholar.sun.ac.za

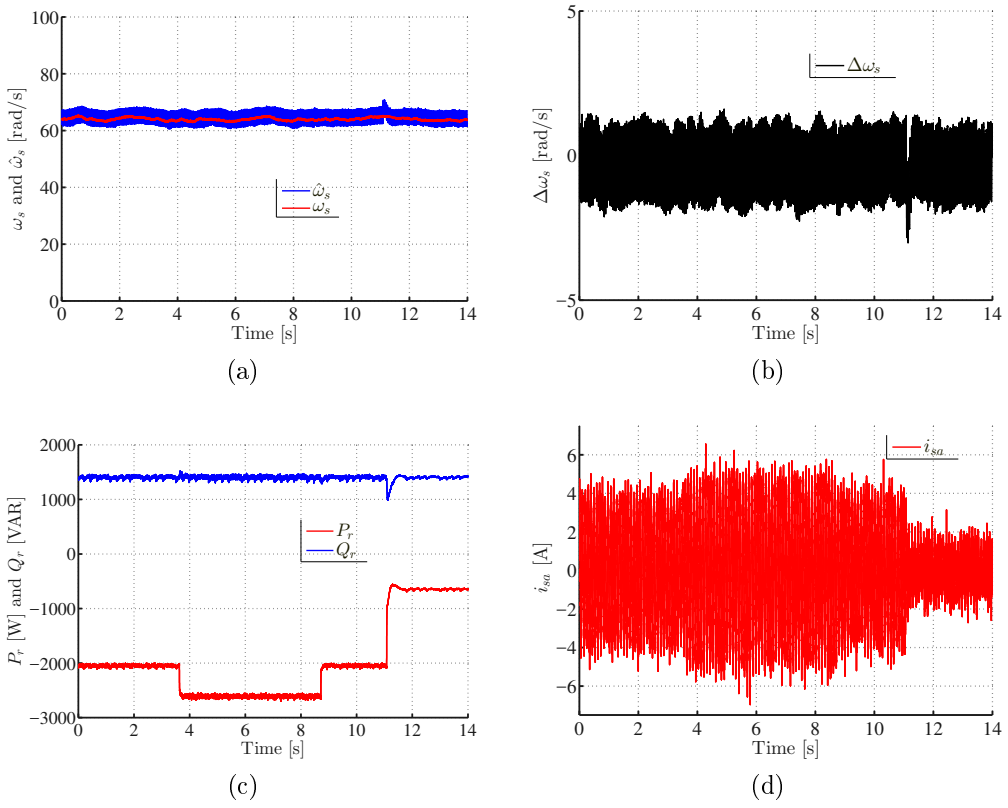

Figure 6.31: The transient performance of the overall control strategy recoded during change in the active rotor power: (a) ω_s and $\hat{\omega}_s$; (b) $\Delta\omega_s$; (c) P_r and Q_r, and (d) the phase A stator current.

6.7 PLL-based high order sliding observer estimator for sensor-less control of RDFIG systems

In this section, the experimental results of the sensor-less control strategy based on the association of the HOSMO and the PLL estimator is discussed. Also a comparative study with the sesnor-less control strategy presented in [1], is also presented. The HOSMO is discussed in Section 5.5. The parameters of the HOSMO are $m_1 = m_2 = 500$ and $m_3 = m_4 = 20000$ while the parameters of the PI controller of the PLL estimator are $k_p = 70$ and $k_i = 2300$. The design procedure for the PLL gains. The parameters for both PI controllers of the inner control loop are $k_p = 35$ and $k_i = 500$, whilst those for the PI controller of the outer loop are $k_p = 0.2$ and $k_i = 20$. The design method of the PI gains in the inner control loop is based on the well-known Modulus Optimum method while for the outer control loop the design is conducted based on the Symmetrical Optimum method.

Stellenbosch University https://scholar.sun.ac.za

6.7.1 Steady state performance

In Figure 6.32, the performance of the PLL-based HOSMO estimator during sub-synchronous operating conditions with the change in magnitude of the α-axis stator is shown. The rotor of the rotor-tied DFIG rotates at 1050 rpm which leads to an angular slip speed of about 94.2 rad/s, as shown in Figure 6.32(a). During the steady state operating conditions, it can be seen that the estimated and the actual slip speeds converge while the slip speed error is close to zero, as shown in Figure 6.32(b). Also, the estimated and measured α-axis stator currents converge, as shown in Figure 6.32(c) whilst the α-axis stator current error converges to zero, as depicted in Figure 6.32(d). It can be seen that the estimated and measured α-axis stator currents converge and the α-axis stator current error is less than 0.25 A as it can be seen in Figure 6.32(d). At about t=0.42 s, there is a change in the α-axis stator current from 1.9 A to 4.2 A as depicted in Figure 6.32(c). At that time it can be seen that there is a slight surge in the the estimated slip speed as shown

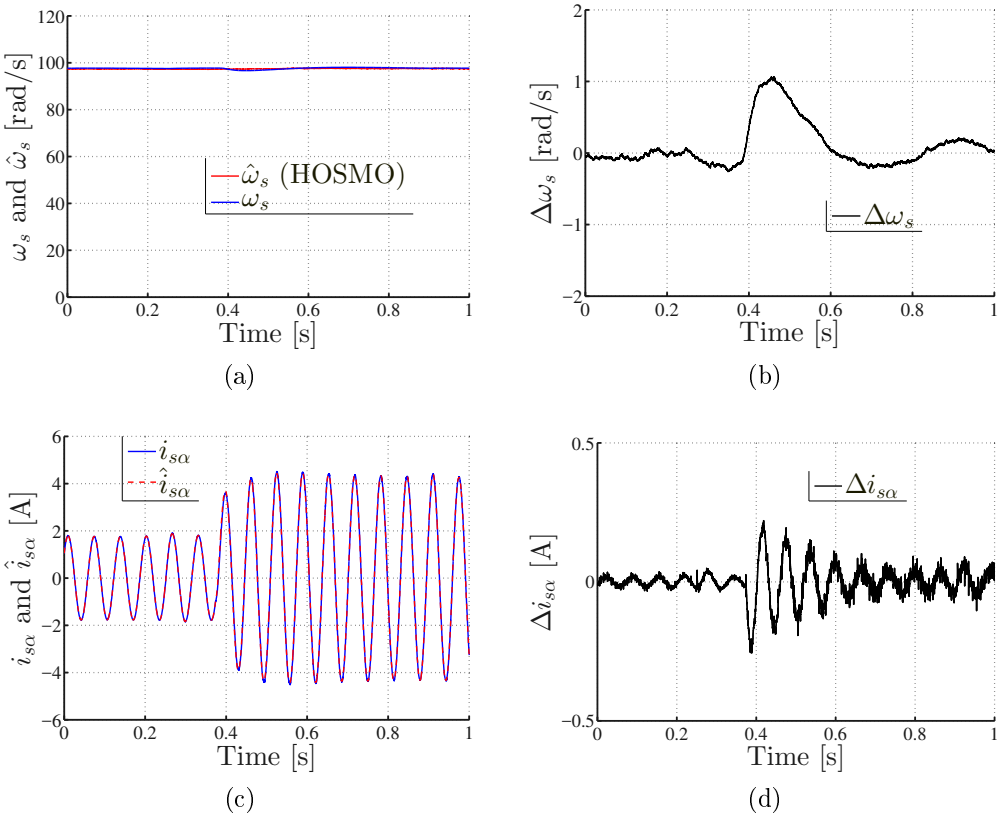

Figure 6.32: Experimental performance of the PLL-based HOSMO estimator during sub-syncrhounous operating conditions: (a) the actual and estimated slip speeds; (b) the slip speed errors, (c) the measured and estimated α-axis stator currents, and (d) the α-axis stator current errors.

Stellenbosch University https://scholar.sun.ac.za

in Figure 6.32(a). Hence, the slip speed error increases up to a maximum of 1.2 rad/s, as shown Figure 6.32(b). Meanwhile in Figure 6.32(d), the α-axis stator current error increases to a maximum 0.25 rad/s.

In Figure 6.33, the performance of the PLL-based HOSMO estimator during super-synchronous operating conditions when the rotor-tied DFIG is running at 1650 rpm is presented. The estimated and actual slip speeds are presented in Figure 6.33(a). The slip speed error is shown in Figure 6.33(b) and it can be observed to converge around zero with the maximum error value being 1.2 rad/s during steady state operating conditions. Thus, it can be seen that the estimated slip speed value converge to the actual slip speed. The estimated and the actual α-axis stator currents and the α-axis stator current error are shown in Figure 6.33(c) and Figure 6.33(d), respectively. It can be seen estimated α-axis current converge to the actual one. At t=0.6 s, there is a sudden change in the α-axis current which creates a surge in the slip speed error of about 0.6 rad/s, as shown in Figure 6.33(b). In addition, a surge is also caused in the α-axis stator current error of just under 0.5 A. The per-

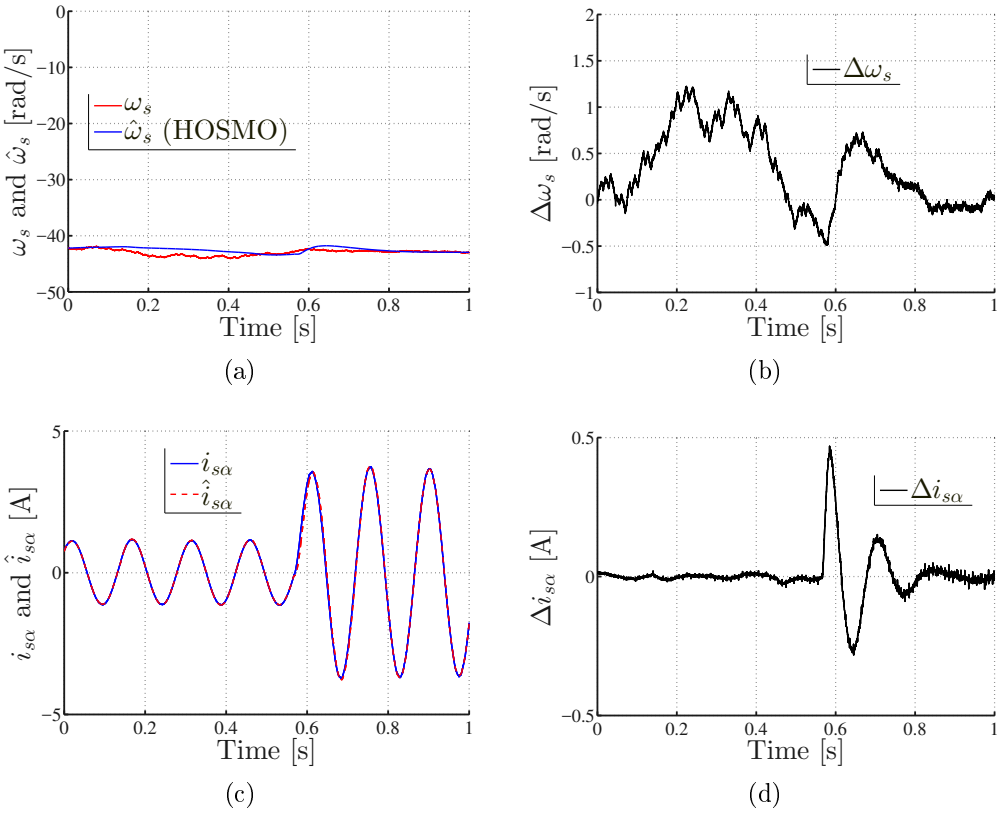

Figure 6.33: Experimental performance of the PLL-based SMO estimator during super-synchronous operating conditions: (a) the actual and estimated slip speeds; (b) the slip speed errors, (c) the measured and estimated α-axis stator currents, and (d) the α-axis stator current errors.

Stellenbosch University https://scholar.sun.ac.za

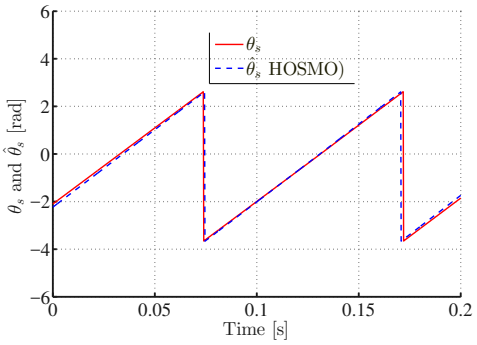

Figure 6.34: Experimmental Illustration of the estimated and actual slip angle estimated using the PLL-based HOSMO estimator during sub-synchronous operating conditions

formance presented in Figure 6.32 and Figure 6.33, validates the robustness of the proposed PLL-based HOSMO estimator under sudden change in stator current.

In Figure 6.34, the estimated slip angle calculated using the PLL-based HOSMO estimator and the actual slip angle during sub-synchronous operating conditions are illustrated. It can be seen that when the rotor-tied DFIG operates at a rotor speed of 1050 rpm, the estimated slip speed converge with the actual slip speed value. In Figure 6.35, the estimated slip speed using the PLL-based HOSMO estimator and the actual slip speed during super-synchronous operating conditions are shown. It can be seen that when the rotor-tied DFIG operates at a rotor speed of 1650 rpm, the estimated slip speed converge with the actual slip speed value. Hence, based on Figure 6.34 and Fig 6.35, it can be concluded that the performance of the PLL-based HOSMO estimator is satisfactory.

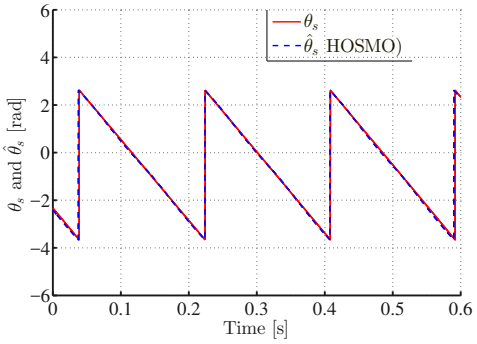

Figure 6.35: Experimental Illustration of the estimated and actual slip angle estimated using the PLL-based HOSMO estimator during super-synchronous operating conditions

Stellenbosch University https://scholar.sun.ac.za

6.7.2 Comparative performance under sudden change in the stator current magnitude

In Figure 6.36, the experimental performance of PLL-based SMO estimator during change in stator current magnitude is illustrated. From top to bottom, the estimated and measured slip speeds, the d-axis and q-axis stator currents

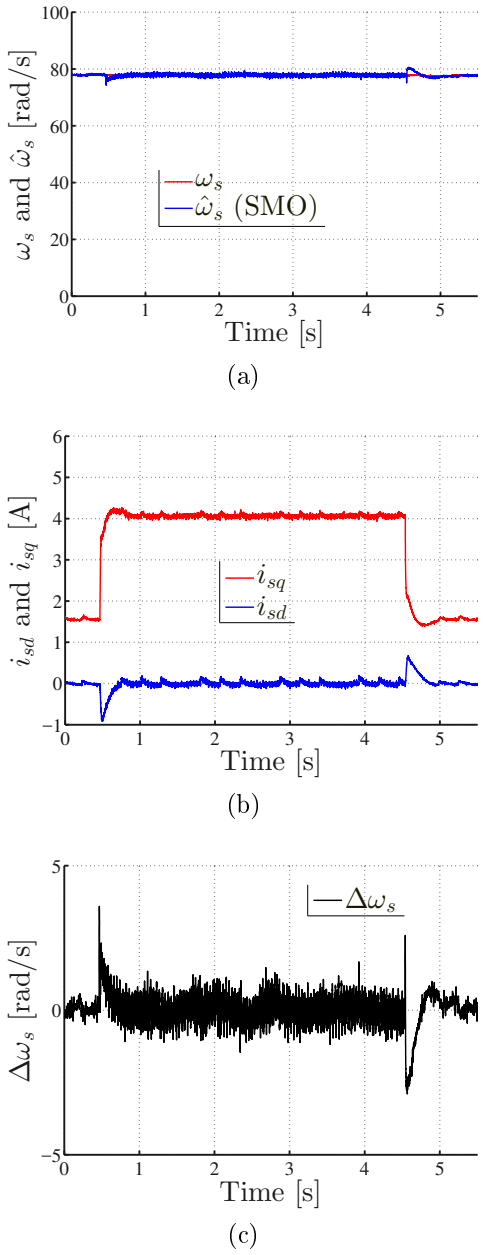

Figure 6.36: Experimental performance the PLL-based SMO observer during change in stator current magnitude from 1.5 A to 4.2 A to 1.5 A: (a) the actual and estimated slip speeds; (b) the d-axis and q-axis stator currents, and (c) the slip speed error.

Stellenbosch University https://scholar.sun.ac.za

and the slip speed error are depicted in Figure 6.36(a), Figure 6.36(b) and Figure 6.36(c), respectively. The RDFIG operates at 1140 rpm which is correlated to a slip speed of about 75.36 rad/s. The estimated and the actual slip speeds are shown in Figure 6.36(a). At t=0.4 s a change in stator current magnitude from 1.5 A to 4.1 A occurs as shown in Figure 6.36(b). At the same time, it can be seen from Figure 6.36(a) there is a surge in the estimated slip speed which is acceptable while at steady state the slip speed converge to zero, as shown in Figure 6.36(c). At t=4.5 s, the stator current magnitude suddenly decrease to 1.5 A. This implies a surge of about 3 rad/s in the estimated slip speed, as shown in Figure 6.36(c). However, for the PLL-based SMO estimator signal quality is deter with high values of the stator current as shown in Figure 6.36(c) between t=0.5 s and t=4.5 s.

In Figure 6.37, the experimental performance of the PLL-based HOSMO estimator during change in stator current magnitude from 1.5 A to 4.2 A to 1.5 A are shown. The actual and estimated slip speeds, the d-axis and q-axis stator currents and the slip speed error, are presented in Figure 6.37(a), Figure 6.37(b) and Figure 6.37(c), respectively. Comparing the transient performance of the PLL-based HOSMO estimator shown in Figure 6.37 and that of Figure 6.36, the error $\Delta\omega_s$ are reduced and improved. Also, the signal quality of the slip speed for the PLL-based HOSMO is better compared to that of the PLL-based SMO estimator. At t=0.5 s, compared to the performance depicted in Figure 6.36(c), the slip speed error is less than 1 rad/s which is very satisfactory and the signal quality is improved even with high values of the stator current. At t=4.5 s, the maximum slip speed error is less than 1 rad/s which is better than the performance of the PLL-based SMO estimator shown in Figure 6.36(c).

6.7.3 Comparative performance under varying rotor angular speed

In Figure 6.38, the experimental performance of PLL-based SMO estimator under change in speed from sub-synchronous operating conditions to super-synchronous operating conditions and then from super-synchronous operating conditions to sub-synchronous are shown. The estimated and the actual slip speeds are illustrated in Figure 6.38(a) while the slip speed error is shown in Figure 6.38(b). During the change from sub-synchronous to super-synchronous operating conditions as shown in Figure 6.38(a) between t=4 s and t=14 s, it can be seen that the maximum slip speed error is less than 2.5 rad/s which is very satisfactory. At around the synchronous speed both the estimated actual speed approaches zero at which implies the change in the value of the slip error reduces to zero, as it can be seen from Figure 6.38(b). A similar pattern can be seen from t=37 s to t=47 s, as it can be seen from Figure 6.38(a) and Figure 6.38(b).

Stellenbosch University https://scholar.sun.ac.za

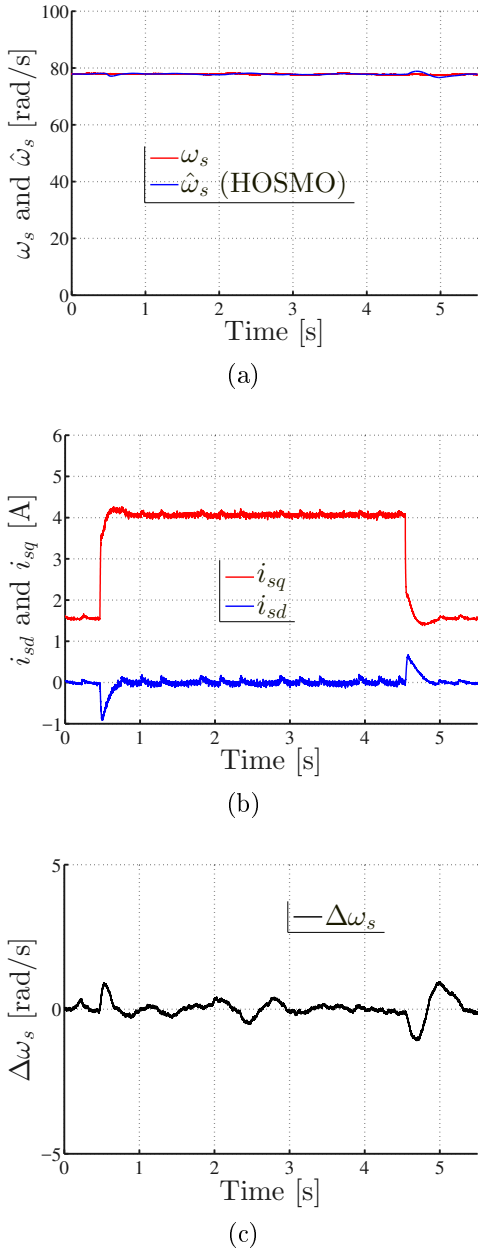

Figure 6.37: Experimental performance of the PLL-based HOSMO observer during change in stator current magnitude from 1.5 A to 4.2 A to 1.5 A: (a) the actual and estimated slip speeds; (b) the d-axis and q-axis stator currents, and (c) the slip speed errors.

On the other hand, the experimental performance of the PLL-based HOSMO estimator during change from sub-synchronous operating to super-synchronous operating conditions and vice versa is illustrated in Figure 6.39. The estimated and actual slip speeds and the slip speed error are illustrated in Figure 6.39(a) and Figure 6.39(b), respectively. At first glance compared to the experimen-

Stellenbosch University https://scholar.sun.ac.za

tal performance illustrated in Figure 6.38(a), one can see that the slip speed error is less than 2.5 rad/s for most of the interval time of the change in speed t=4 s and t=14 s which is almost similar to the performance shown in Figure 6.38(b). Also, the signal quality of the PLL-based HOSMO estimator is better compared to that of the PLL-based SMO estimator. A similar pattern can be seen from t=37 s to t=47 s as it can be seen from Figure 6.39(a) and Figure 6.39(b). The experimental performance of the PLL-based HOSMO estimator is very satisfactory with a maximum slip speed error of 2.5 rad/s which equivalent to 11.67 rpm.

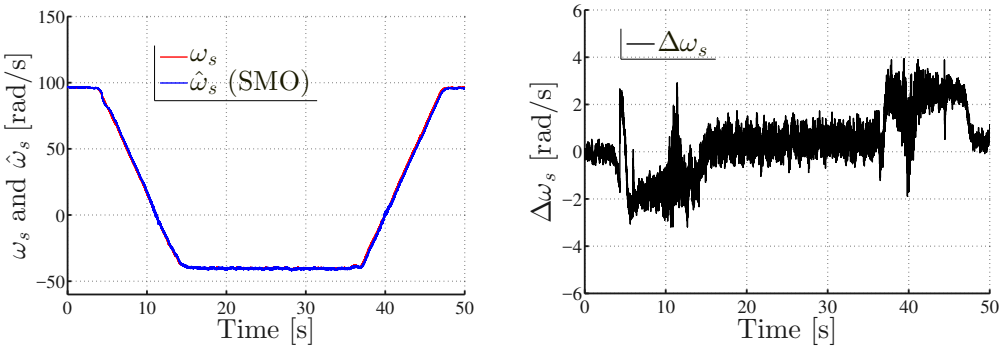

(a) (b)

Figure 6.38: Experimental performance of the PLL-based SMO estimator during change in speed: (a) the actual and estimated slip speeds; (b) the slip speed errors.

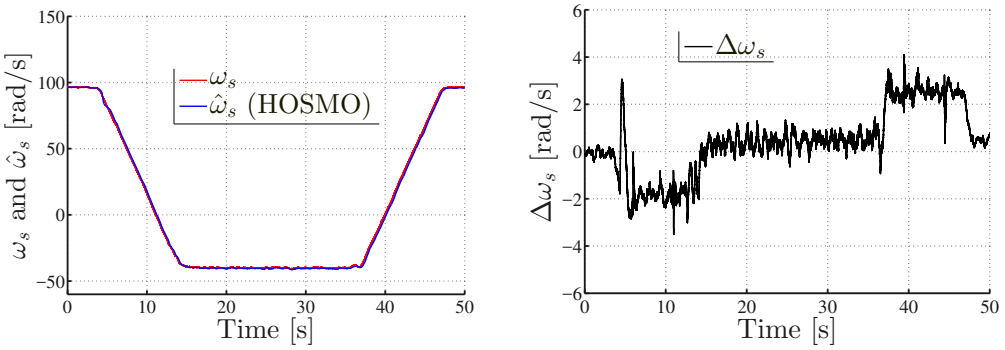

(a) (b)

Figure 6.39: Experimental performance of the PLL-based HOSMO estimator during change in speed: (a) the actual and estimated slip speeds; (b) the slip speed errors.

Stellenbosch University https://scholar.sun.ac.za

6.7.4 Comparative performance under inaccurate machine parameters

In Figure 6.40, the experimental performance of the PLL-based SMO estimator under change in speed with inaccurate stator resistance and inductance is presented. The estimated and actual slip speed are shown in Figure 6.40(a) while the slip speed error is depicted in Figure 6.40(b). It can be seen that the inaccuracy in machine parameter affects not only the signal quality of the estimated slip speed, but also the maximum slip error. It can be seen that the maxim slip speed error during the whole operating conditions is about 4 rad/s.

In Figure 6.41, the experimental performance of the PLL-based HOSMO estimator during change in speed with inaccurate machine parameter (stator

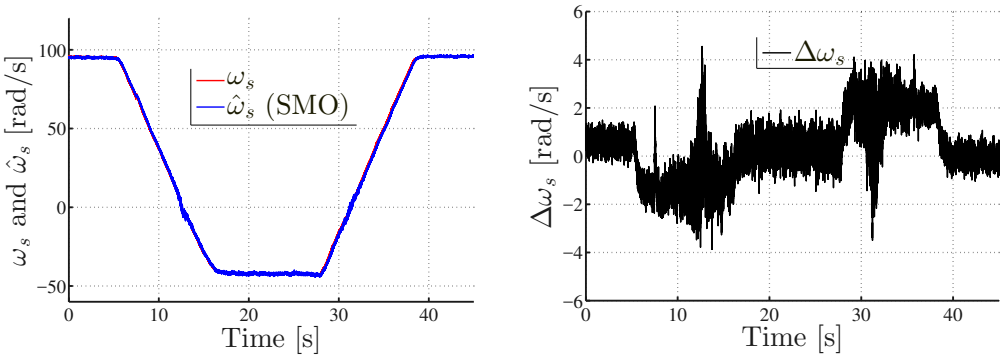

Figure 6.40: Experimental performance of the PLL-based SMO estimator under inaccurate machine parameters ($1.3L_s$ and $1.3R_s$): (a) the actual and estimated slip speeds; (b) the slip speed errors.

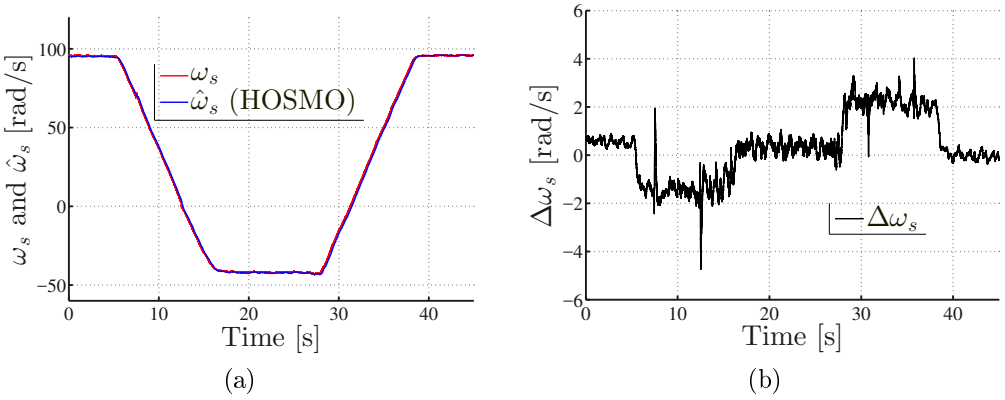

Figure 6.41: Experimental performance of the PLL-based HOSMO estimator under inaccurate machine parameters ($1.3L_s$ and $1.3R_s$): (a) the actual and estimated slip speeds; (b) the slip speed errors.

Stellenbosch University https://scholar.sun.ac.za

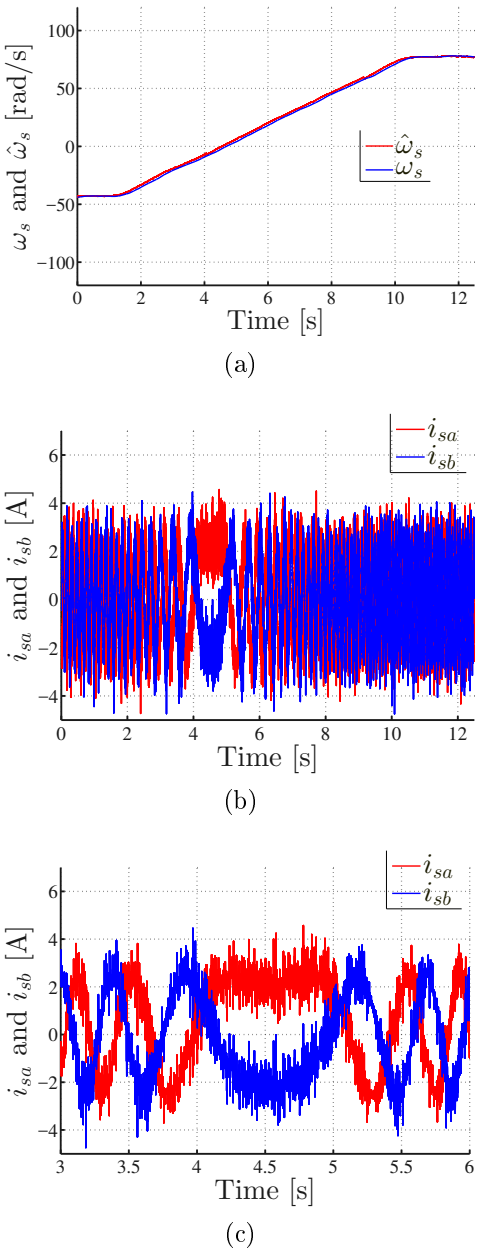

Figure 6.42: Experimental performance of the sensor-less control strategy for rotor-tied DFIG: (a) the actual and estimated slip speeds; (b) the three-phase stator current, and (c) the zoomed three-phase stator current.

resistance and inductance). In comparison with the performance shown in Figure 6.40, the inaccuracy in machine parameters does not affect neither the signal quality of the estimated slip speed nor the maximum slip speed error. Hence, the performance of the PLL-based HOSMO estimator with inaccurate machine parameter is better than that of the PLL-based SMO estimator.

Stellenbosch University https://scholar.sun.ac.za

6.7.5 Performance under varying rotor angular speed

In Figure 6.42, the performance of the proposed sensor-less vector control strategy under steady change in speed from super-synchronous to sub-synchronous speed is shown. The estimated and the actual slip speeds, the phase A and phase B stator currents and the zoomed phase A and phase B stator currents are presented in Figure 6.42(a), Figure 6.42(b) and Figure 6.42(c), respectively. From the figure, it can be seen the estimated slip speed converge to the actual speed slip. From Figure 6.42(b) and Figure 6.42(c), one can notice a clear change of sequence of the three-phase stator current during the transition from sub- to super-synchronous operation modes.

6.8 Comparative study of the proposed slip speed/angle estimators

In this section, a comparative study on the proposed slip speed estimators whose experimental performance are depicted from Section 6.4 to Section 6.7 is given. Although, the performance of each slip speed estimator is satisfactory, a comparative performance is conducted in order to determine the better performer with regards to : the chattering of the estimated slip speed, the slip speed error during change in stator current, the slip speed error during steady change in speed and the robustness to machine parameter variations.

The performance of the proposed slip speed estimators are summarised in Table 6.1. It can be seen that the slip speed estimator based on the association of the PLL estimator and the HOSMO displays less chattering in the estimated slip speed, while, the slip speed estimator based on the association of the PLL estimator and the STSMO displays very high chatter in the estimated slip speed. Low chattering can be seen from the estimated slip speed with the PLL-based ASMO while an average chattering can be observed form the estimated slip speed with the use of the PLL-based SMO.

Given that all proposed slip speed estimators uses the stator current as state variable, it is also important to look at the behaviour of the proposed slip speed estimators with the change in the stator current magnitude. From Table 6.1, it can be seen that the lowest slip speed error during change in stator

Table 6.1: Comparative performance of the proposed slip speed estimators

Slip speed estimators	chattering effect	Slip speed error during Change in current	Slip speed error during Change in speed	Parameter variations
PLL-based SMO	middle	$\lvert\Delta\omega_s^{\max}\rvert = 4$ rad/s	$\lvert\Delta\omega_s^{\max}\rvert = 2.5$ rad/s	low
PLL-based ASMO	low	$\lvert\Delta\omega_s^{\max}\rvert = 8$ rad/s	$\lvert\Delta\omega_s^{\max}\rvert = 2$ rad/s	middle
PLL-based STSMO	high	$\lvert\Delta\omega_s^{\max}\rvert = 2.5$ rad/s	$\lvert\Delta\omega_s^{\max}\rvert = 1$ rad/s	low
PLL-based HSMO	very low	$\lvert\Delta\omega_s^{\max}\rvert = 1.5$ rad/s	$\lvert\Delta\omega_s^{\max}\rvert = 2.5$ rad/s	low

Stellenbosch University https://scholar.sun.ac.za

current magnitude is accomplished with the PLL-based HOSMO estimator. This can be explained with the fact that the HOSMO takes into consideration the dynamics of the back-EMF space vector. The maximum slip speed error is 2.5 rad/s with the PLL-based STSMO estimator, while when the PLL-based SMO estimator is used , the maximum slip speed error is 4 rad/s. The least performer for the change in current is the PLL-based ASMO estimator with a maximum slip speed error of 8 rad/s.

From Table 6.1, the PLL-based STSMO estimator is the best performer with the change in rotor angular speed and it a slip speed error of 1 rad/s. The second best performer is the PLL-based ASMO estimator which has a slip speed error of 2 rad/s. Both the PLL-based SMO and PLL-based HOSMO estimators have slip speed errors of 2.5 rad/s.

The PLL-based SMO estimator, PLL-based HOSMO estimator and the PLL-based STSMO estimator are almost immune to parameter variations while the PLL-based ASMO estimator, demonstrated an increase in chattering during machine parameter variations.

6.9 Summary

In this Chapter, the experimental results of the proposed slip speed estimators for sensor-less control of RDFIG systems are presented. The experiments are performed on a 5.5-KW custom-design RDFIG test-bench. The proposed slip speed estimators demonstrate satisfactory performance under various operating conditions.

Stellenbosch University https://scholar.sun.ac.za

Chapter 7

Conclusions and recommendations on future works

7.1 Introduction

In this thesis, several slip speed estimators for sensor-less control of the RDFIG-based WECS are proposed and experimentally evaluated. The focus of the study is specifically on slip speed estimators. This Chapter states the conclusions of the study, and also presents the recommendations on future work.

7.2 Conclusions

The aim of this research study was to develop slip speed estimators for sensor-less control of the RDFIG systems in medium-speed applications. The slip speed estimators investigated, intend to solve the problem linked to the use of electromechanical sensors in the RDFIG control. The proposed slip speed estimators were proposed, investigates and validated in this thesis. The innovative slip speed estimators were based on the associations of sliding mode observers and the PLL estimators.

The PLL estimator are used in order to track the slip angle from the estimated back-EMF. The standard PLL uses a sine function in order to determine the error between the tracked angle and the estimated angle. Thus, when the actual angle is negative, a phase shift of of π is introduced. In rotor-tied configuration, the rotor angular speed is negative and that the slip in super-synchronous operating conductions is negative. The proposed PLL estimator eliminates the shift of π in super-synchronous operating conditions introduced by the sine function.

The SMOs are known for their robustness against parameter variations and disturbances. However, the noise introduce by the sliding mode function is their main disadvantage. The proposed SMOs use the stator current and

Stellenbosch University https://scholar.sun.ac.za

the back-EMF, as state variables. This has the advantage of starting the estimation even before the RDFIG is connected to the grid. This thesis covered four slip speed estimators for the sensor-less control of the RDFIG systems. They are;

- The PLL-based SMO estimator,
- The PLL-based ASMO estimator,
- The PLL-based STSMO estimator, and
- PLL-based HOSMO estimator.

The following conclusions can be made from this research project;

7.2.1 PLL-based SMO estimator

A PLL-based SMO estimator for sensor-less control of RDFIG systems was proposed. The parameters of the SMO are designed based on the Lyapunov stability criteria in order to guarantee the convergence of the observer within a finite time. The parameters of the PLL estimator are designed based on the anti-disturbance performance approach. Experimental results showed that the PLL-based SMO estimator had satisfactory steady state and transient performance in all operating conditions of the RDFIG. The performance of the PLL-based SMO estimator does not degrade with changes in machine parameters. Experimental results showed that the sensor-less control of RDFIG systems using the PLL-based SMO estimator was satisfactory during speed transitions. The implementation of the proposed is simple and has a low computational cost and, thus, has great potential for industrial applications.

7.2.2 PLL-based ASMO estimator

A PLL-based ASMO estimator for sensor-less control of the RDFIG systems was proposed. The ASMO helps in reducing the chattering effect that is caused by the constant gains of the SMO. The Lyapunov stability criteria is used in order to guarantee the convergence of the ASMO at a finite. Also, the design of the ASMO gains are discussed in order to reduce the chattering effect. The recorded experimental results under steady state and transient operating conditions were satisfactory. In addition, it was shown that the adaptive gains is adjusted on-line based on the disturbance in the system. This is very excellent in reducing the chattering effect.

7.2.3 PLL-based STSMO estimator

A robust PLL-based STSMO estimator for sensor-less control of the RDFIG systems was proposed and analysed. The parameters of the proposed PLL-

Stellenbosch University https://scholar.sun.ac.za

based STSMO estimator were designed such that the Lyapunov stability criteria is satisfied. This guarantees the convergence of the estimator in a finite time and a high estimation performance is achieved. The recorded experimental results validates the performance of the PLL-based STSMO estimator with remarkable experimental performances in steady and transient operating conditions such as; change in speed, change in stator current magnitude and change in the active power output.

7.2.4 PLL-based HOSMO estimator

A PLL-based HOSMO estimator has been investigated and analysed for sensor-less control of RDFIG systems has been presented and analysed in grid-connected mode. In the HOSMO The experimental performance of the proposed sensor-less control strategy has also been compared to that of an existing sensor-less control strategy based on PLL-based SMO estimator under similar scenarios. The experimental results show that compared to the other slip speed estimators proposed in this thesis, PLL-based HOSMO estimator has much lower chattering in the estimated signal, improved dynamic capabilities during change in stator current and it is satisfactory in terms of speed variations of the system.

7.3 Recommendations for future works

Recommendations for future works can broken down as follows;

- Perform the stability analysis of the slip speed estimator based on the association of the PLL and any proposed SMOs using a rigorous approach such as the singular perturbation approach. Such rigorous proof is still inadequate in the literature.
- Perform a rigorous comparative study of all slip speed estimators using appropriate measures such as the integral time absolute error (ITAE) or the integral absolute error (IAE). This will allow to quantify the performance by an objective and precise measure.
- Investigate the performance of slip speed estimator based on artificial intelligence algorithms.
- The sensor-less control strategies proposed in this thesis have been tested under normal operating conditions of the grid. Investigation on the behaviour of the sensor-less control strategies under transient operating conditions such voltage sags, under low voltage right through and under short circuit is needed.
- Investigate the performance of the proposed sensor-less control strategies under the use of wind speed emulator.

Stellenbosch University https://scholar.sun.ac.za

References

[1] M. W. K. Mbukani and N. Gule, "Performance Analysis of a PLL-Based Sensor-Less Control of Rotor-Tied DFIG Systems," in *2018 IEEE 9th International Symposium on Sensorless Control for Electrical Drives, SLED 2018*. IEEE, 2018, pp. 48–53.

[2] R. Pena, J. Clare, and G. Asher, "Doubly fed induction generator using back-to-back PWM converters and its application to variable-speed wind-energy generation," *IEEE Proceedings-Electric Power Applications*, vol. 143, no. 3, pp. 231–241, 1996.

[3] S. Muller, M. Deicke, and R. D. Doncker, "Doubly fed induction generator systems for wind turbines," *Industry Applications Magazine*, vol. 8, no. 3, pp. 26–33, 2002.

[4] M. Tazil, V. Kumar, R. Bansal, S. Kong, Z. Dong, and W. Freitas, "Three-phase doubly fed induction generators: an overview," *IET Electric Power Applications*, vol. 4, no. 2, p. 75, 2010.

[5] R. Cardenas, R. Pena, S. Alepuz, and G. Asher, "Overview of Control Systems for the Operation of DFIGs in Wind Energy Applications," *IEEE Transactions on Industrial Electronics*, vol. 60, no. 7, pp. 2776–2798, 2013.

[6] D. D. Reigosa, F. Briz, C. Blanco, and J. M. Guerrero, "Sensorless Control of Doubly Fed Induction Generators Based on Stator High-Frequency Signal Injection," *IEEE Transactions Industry Applications*, vol. 50, no. 5, pp. 3382–3391, 2014.

[7] D. D. Reigosa, F. Briz, C. B. Charro, A. D. Gioia, P. García, and J. M. Guerrero, "Sensorless Control of Doubly Fed Induction Generators Based on Rotor High-Frequency Signal Injection," *IEEE Transactions on Industry Applications*, vol. 49, no. 6, pp. 2593–2601, 2013.

[8] K. Tshiloz and S. Djurović, "Wide range sensorless speed estimation in wound rotor induction machines by sliding window search of the stator current signal," in *8th IET International Coference on Power Electroics, Machines and Drives (PEMD 2016)*, vol. 10, no. 1, 2016, pp. 1–6.

Stellenbosch University https://scholar.sun.ac.za

[9] L. Morel, H. Godfroid, A. Mirzaian, and J. M. Kauffmann, "Double-fed Induction Machine: Converter Optimisation and Field Oriented Control without Position Sensor," *IEE Proceedings - Electric Power Applications*, vol. 145, no. 4, pp. 360–368, 1998.

[10] L. Harnefors and H.-p. Nee, "A General Algorithm for speed and Position Estimation of AC Motors," *IEEE Transactions on Industrial Electronics*, vol. 47, no. 1, pp. 77–83, 2000.

[11] M. Abdelrahem, C. Hackl, and R. Kennel, "Sensorless Control of Doubly-Fed Induction Generators in Variable-Speed Wind Turbine Systems," in *2015 International Conference on Clean Electrical Power (ICCEP)*, 2015, pp. 406–413.

[12] M. F. Iacchetti, "Adaptive tuning of the stator inductance in a rotor-current-based MRAS observer for sensorless doubly-fed induction machine drives," *IEEE Transactions on Industrial Electronics*, vol. 54, no. 2, pp. 4683–462, 2011.

[13] L. Y. Lu, C. C. Chu, and T. W. Yeh, "Model Reference Adaptive Back-EMF Estimations for Sensorless Control of Grid-Connected Doubly-Fed Induction Generators," in *2016 IEEE Industry Applications Society Annual Meeting*, 2016, pp. 1–8.

[14] Y. Zhang, Z. Yin, W. Li, X. Tong, and Y. Zhong, "Speed sensor-less model predictive control based on disturbance observer for induction motor drives," in *2019 IEEE International Symposium on Predictive Control of Electrical Drives and Power Electronics (PRECEDE)*, 2019.

[15] M. Benbouzid, B. Beltran, H. Mangel, and A. Mamoune, "A High-Order Sliding Mode Observer for Sensorless Control of DFIG-Based Wind Turbines," in *IECON 2012-38th Annual Conference on IEEE Industrial Electronics Society*, 2012, pp. 4288–4292.

[16] C. Wei, Z. Zhang, J. Zeng, and W. Qiao, "Stator Current-Based Sliding Mode Observer for Sensorless Vector Control of Doubly-Fed Induction Generators," in *2015 IEEE Energy Conversion Congress and Exposition (ECCE)*, 2015, pp. 4165–4171.

[17] C. Wei, W. Qiao, and Y. Zhao, "Sliding-Mode Observer-Based Sensorless Direct Power Control of DFIGs for Wind Power Applications," in *2015 IEEE Power & Energy Society General Meeting*, 2015, pp. 1–5.

[18] X. Zheng, R. Song, and H. Li, "Full-order terminal sliding mode stator flux observer for DFIG," in *2016 IEEE 11th Conference on Industrial Electronics and Applications (ICIEA)*, 2016, pp. 299–303.

Stellenbosch University https://scholar.sun.ac.za

[19] Z. Yan and V. Utkin, "Sliding mode observers for electric machines-an overview," in *IEEE 2002 28th Annual Conference of the Industrial Electronics Society IECON 02*, 2002, pp. 1842–1847.

[20] B. Shen, V. Low, B. Teck, and O. Fellow, "Slip frequency phase lock loop (PLL) for decoupled P-Q control of doubly-fed induction generator (DFIG)," in *30th annual Conference of IEEE Industrial Electroics Society,2004 (IECON)*, 2004, pp. 80–85.

[21] B. Shen and B. T. Ooi, "Parameter-Insensitive Sensorless Decoupled P-Q Controller for Doubly-Fed Induction Machine," in *2007 IEEE Power Electronics Specialists Conference*, no. 1, 2007, pp. 2102–2107.

[22] M. A. Rani Asha, C. Nagamani, and G. S. Ilango, "An Improved Rotor PLL (R-PLL) for Enhanced Operation of Doubly Fed Induction Machine," *IEEE Transactions on Sustainable Energy*, vol. 8, no. 1, pp. 117–125, 2017.

[23] C. Olivieri and M. Tursini, "A novel PLL scheme for a sensorless PMSM drive overcoming common speed reversal problems," in *SPEEDAM 2012 - 21st International Symposium on Power Electronics, Electrical Drives, Automation and Motion*. IEEE, 2012, pp. 1051–1056.

[24] P. Tao, F. Wang, X. Mei, and J. Lin, "PLL with piecewise judgement function for SMO based sensor-less Control of PMSM," in *5th International Conference on Conference on Enterprise Systems (ES)*, 2017, pp. 190–194.

[25] Y.-M. You, T. A. Lipo, and B.-I. Kwon, "A novel grid-connected to rotor type doubly fed induction generator for wind turbine systems," in *8th International Conference on Power Electronics - ECCE Asia*, 2011, pp. 646–653.

[26] M. Y. You, T. A. Lipo, and B. I. Kwon, "Design and analysis of a novel grid-connected to rotor type fed induction machine," *IEEE Transactions on Magnetics*, vol. 48, no. 2, pp. 919–922, 2012.

[27] N. David and D. Aliprantis, C., "DFIG with grid-connected rotor for wind energy conversion system," in *International Eectrical Machines and Drives Conference (IEMDC)*, 2013, pp. 125–130.

[28] ——, "Improved Efficiency of DFIG Wind Energy Conversion Systems by Operating in the Rotor-Tied Configuration," in *2014 International Conference on Electrical Machines (ICEM)*, 2014, pp. 189–195.

[29] O. I. Olubamiwa and N. Gule, "The optimal design and autonomous testing of a rotor-tied DFIG," in *2017 IEEE AFRICON*, 2017, pp. 1378–1383.

Stellenbosch University https://scholar.sun.ac.za

[30] ——, "Performance investigation of DFIG topologies with different design parameters," in *2017 IEEE AFRICON*, 2017, pp. 1242–1247.

[31] N. David and Z. Wang, "Rotor-Tied Configuration of DFIG Wind Turbines for Improving Reactive Power Support Capability," in *2018 IEEE Power & Energy Society General Meeting*, 2018.

[32] M. W. K. Mbukani and N. Gule, "Experimental Implementation of the Stator-Side Control of a Grid-Connected Rotor-Tied DFIG-Based WECS," in *SPEEDAM 2018 - Proceedings: International Symposium on Power Electronics, Electrical Drives, Automation and Motion*. IEEE, 2018, pp. 895–900.

[33] R. Cardenas and R. Pena, "Sensorless vector control of induction machines for variable-speed wind energy applications," *IEEE Transactions on Energy Conversion*, vol. 19, no. 1, pp. 196–205, 2004.

[34] W. Qiao, X. Yang, and X. Gong, "Wind speed and rotor position sensorless control for direct-drive PMG wind turbines," *IEEE Transactions on Industry Applications*, vol. 48, no. 1, pp. 3–11, 2012.

[35] W. Qiao, "Intelligent mechanical sensorless MPPT control for wind energy systems," in *IEEE Power Energy Society General Meeting*, 2012, pp. 1–8.

[36] Y. Zhao, C. Wei, Z. Zhang, and W. Qiao, "A Review on Position / Speed Sensorless Control for Permanent Sychronous Machine-Based Wind Energy Conversion Systems," *IEEE Transactons of Emerging and Selected Topics in Power Electronics*, vol. 1, no. 4, pp. 203–216, 2013.

[37] M. W. K. Mbukani and N. Gule, "PLL-based sliding mode observer estimators for sensor-less control of rotor-tied DFIG systems," *IEEE Transactions on Industry Applications*, vol. PP, no. PP, pp. 1–1, 2019.

[38] ——, "Evaluation of a super-twisting sliding mode observer-based Estimator for power control of rotor-tied DFIG systems," *IET Electric Power Applications*, vol. PP, no. PP, pp. 1–1, 2019.

[39] ——, "Comparison of high-order and second-order sliding Mode-observer-based estimators for speed sensor-less control of rotor-tied DFIG systems," *IET Power Electronics*, vol. PP, no. PP, pp. 1–1, 2019.

[40] Y. Zhao, W. Chun, Z. Zhang, and W. Qiao, "A Review on Position/Speed Sensorless Control for Permanent Magnet Synchronous Machine-Based Wind Energy Conversion Systems," *IEEE Journal of Emerging and Selected Topics in Power Electronics*, vol. 1, no. 4, pp. 203–216, 2013.

Stellenbosch University https://scholar.sun.ac.za

[41] R. Datta and V. T. Ranganathan, "A Simple Position-Sensorless Algorithm for Rotor-Side Field-Oriented Control of Wound-Rotor Induction Machine," *IEEE Transactions Industrial Electronics*, vol. 48, no. 4, pp. 786–793, 2001.

[42] M. T. Abolhassani, P. Niazi, H. A. Toliyat, and P. Ejinti, "A Sensorless Integrated Doubly-Fed Electric Alternator / Active Filter (IDEA) for Variable Speed Wind Energy System," in *38th IAS Annual Meeting of Conference Record of Industry Applications Conference*, 2003, pp. 507–514.

[43] L. Xu and W. Cheng, "Torque and Reactive Power Control of a Doubly-Fed Induction Machine by Position Sensorless Scheme," *IEEE Transactions on Industry Applications*, vol. 31, no. 3, pp. 636–642, 1995.

[44] A. K. C. Nagamani, C. Nagamani, A. B. R. Chaudhury, and G. S. Ilango, "Implicit position and speed estimation algorithm without the flux computation for the rotor side control of doubly fed induction motor drive," *IET Electric Power Applications*, vol. 6, no. 4, pp. 243–252, 2012.

[45] A. Karthikeyan, C. Nagamani, and G. S. Ilango, "A versatile Rotor Position Computation Algorithm for the Power Control of a Grid-Connected Doubly Fed Induction Generator," *IEEE Transactions on Energy Conversion*, vol. 27, no. 3, pp. 697–706, 2012.

[46] M. D. Alegria, J. Andreu, J. L. Martin, and J. L. Villate, "Influence of a Sensorless Algorithm Position Estimation Error on the Control of a Doubly Fed Induction Machine," in *IECON 2007-33rd Annual Conference of the IEEE Industrial Electronics*, 2007, pp. 962–967.

[47] G. D. Marques and D. M. Sousa, "Sensorless Direct Slip Position Estimator of a DFIM Based on the Air Gap pq Vector – Sensitivity Study," *IEEE Transactions on Industrial Electronics*, vol. 60, no. 6, pp. 2442–2450, 2013.

[48] G. D. Marques, D. M. Sousa, and M. F. Iacchetti, "Air-Gap Power-Based Sensorless Control in a DFIG Connected to a DC Link," *IEEE Transactions on Energy Conversion*, vol. 30, no. 1, pp. 367–375, 2015.

[49] B. Singh and N. K. S. Naidu, "Direct Power Control of Single VSC-Based DFIG Without Rotor Position Sensor," *IEEE Transactions on Industry Applications*, vol. 50, no. 6, pp. 4152–4163, 2014.

[50] C. Edwards and S. K. Spurgeon, *Sliding Mode Control : Theory and Applications*, 1st ed. London: Taylor & Francis G, 1998.

[51] V. Utkin, J. Guldner, and J. Shi, *Sliding Mode Control in Electro-Mechanical Systems*. London: Taylor & Francis Group, 1999.

Stellenbosch University https://scholar.sun.ac.za

[52] G. Bartolini, L. Fridman, A. Pisano, and E. Usai, *Modern Sliding Mode Control Theory: New Perspectives and Applications*, 1st ed. Springer-Verlag Berlin Heidelberg, 2008.

[53] Z. Qiao, T. Shi, Y. Wang, Y. Yan, C. Xia, and X. He, "New Sliding-Mode Observer for Position Sensorless Control of Permanent-Magnet Synchronous Motor," *IEEE Transactions on Industrial Electronics*, vol. 60, no. 2, pp. 710–719, 2013.

[54] Y. Zhang and J. Liu, "An improved Q-PLL to overcome the speed reversal problems in sensorless PMSM drive," *2016 IEEE 8th International Power Electronics and Motion Control Conference, IPEMC-ECCE Asia 2016*, no. 1, pp. 1884–1888, 2016.

[55] F. Chen and C. Lin, "FPGA-based sensorless PMSM speed control using adaptive sliding mode observer," in *43rd Annual Conference of the IEEE Industrial Electronic Society IECON 2017*, 2017, pp. 4150–4154.

[56] J. Zhu and K. Khayati, "A new approach for adaptive sliding mode control: Integral/exponential gain law," *Transactions of the Institute of Measurement and Control*, vol. 38, no. 4, pp. 385–394, 2016.

[57] Jianbo Hu, "Parameters adaptive sliding mode control for a class of uncertain nonlinear systems," in *2008 IEEE International Conference on Automation and Logistics*, 2008, pp. 1734–1738. [Online]. Available: https://ieeexplore.ieee.org/document/4636436/

[58] X. Song, J. Fang, B. Han, and S. Zheng, "Adaptive Compensation Method for High-Speed Surface PMSM Sensorless Drives of EMF-Based Position Estimation Error," *IEEE Transactions on Power Electronics*, vol. 31, no. 2, pp. 1438–1449, 2016.

[59] A. Levant, "Robust Exact Differentiation via Sliding Mode Technique," *Automatica*, vol. 34, no. 3, pp. 379–384, 1998.

[60] H. Wang, X. Ge, and Y. C. Liu, "Second-Order Sliding-Mode MRAS Observer-Based Sensorless Vector Control of Linear Induction Motor Drives for Medium-Low Speed Maglev Applications," *IEEE Transactions on Industrial Electronics*, vol. 65, no. 12, pp. 9938–9952, 2018.

[61] A. Pisano, M. Tanelli, and A. Ferrara, "Combined switched/time-based adaptation in second order sliding mode control," in *Proceedings of the IEEE Conference on Decision and Control*. IEEE, 2013, pp. 4272–4277.

[62] Lihang Zhao, Jin Huang, He Liu, Bingnan Li, and Wubin Kong, "Second-Order Sliding-Mode Observer With Online Parameter Identification for Sensorless Induction Motor Drives," *IEEE Transactions on Industrial Electronics*, vol. 61, no. 10, pp. 5280–5289, 2014.

Stellenbosch University https://scholar.sun.ac.za

[63] D. Liang, J. Li, and R. Qu, "Sensorless Control of Permanent Magnet Synchronous Machine Based on Second-Order Sliding-Mode Observer With Online Resistance Estimation," *IEEE Transactions on Industry Applications*, vol. 53, no. 4, pp. 3672–3682, 2017.

[64] J. A. Moreno and M. Osorio, "A Lyapunov approach to second-order sliding mode controllers and observers," in *Proceedings of the IEEE Conference on Decision and Control*. IEEE, 2008, pp. 2856–2861.

[65] A. Levant, "Higher-order sliding modes, differentiation and output-feedback control," *International Journal of Control*, vol. 76, no. 9-10, pp. 924–941, 2003.

[66] S. Di Gennaro, J. Rivera, and B. Castillo-Toledo, "Super-twisting sensorless control of permanent magnet synchronous motors," in *Proceedings of the IEEE Conference on Decision and Control*. IEEE, 2010, pp. 4018–4023.

[67] A. Levant, "Principles of 2-sliding mode design," *Automatica*, vol. 43, no. 4, pp. 576–586, 2007.

[68] S. Wu, Z. Liu, and H. Su, "Adaptive sliding mode sensorless vector control of induction motor using sliding mode MRAS observer," in *Chinese Control Conference, CCC*, 2017, pp. 9124–9129.

[69] C. Schauder, "Adaptive Speed Identification for Vector Control of Induction Motors without Rotational Transducers," *IEEE Transactions on Industry Applications*, vol. 28, no. 5, pp. 1054–1061, 1992.

[70] J. Proboste, G. Asher, J. Clare, and R. Pen, "Rotor current based MRAS observer for doubly-fed induction machines," *Electronic Letters*, vol. 40, no. 12, pp. 769–770, 2004.

[71] R. Cárdenas, R. Peña, G. Asher, J. Clare, and J. Cartes, "MRAS Observer for Doubly Fed Induction Machines," *IEEE Transaction on Energy Conversion*, vol. 19, no. 2, pp. 467–468, 2004.

[72] R. Cárdenas, R. Peña, J. Proboste, G. Asher, and J. Clare, "MRAS Observer for Sensorless Control of Standalone Doubly Fed Induction Generators," *IEEE Transactions on Energy Conversion*, vol. 20, no. 4, pp. 710–718, 2005.

[73] R. Cardenas, R. Petia, J. Proboste, G. Asher, J. Clare, and P. Wheeler, "MRAS Observers for Sensorless Control of Doubly-Fed Induction Generators," in *2008 4th IET Conference on Power Electronics, MAchines and Drives*, 2008, pp. 568–572.

Stellenbosch University https://scholar.sun.ac.za

[74] R. Cárdenas, R. Peña, J. Clare, G. Asher, and J. Proboste, "MRAS Observers for Sensorless Control of Doubly-Fed Induction Generators," *IEEE Transactions on Power Electronics*, vol. 23, no. 3, pp. 1075–1084, 2008.

[75] Y. Guofeng, L. I. Yongdong, C. Jianyun, and J. Xinjian, "A Novel Position Sensor-less Control Scheme of Doubly Fed Induction Wind Generator Based on MRAS Method," in *2008 IEEE Power Electronics Specialists Conference*, 2008, pp. 2723–2727.

[76] R. Peña, R. Cárdenas, J. Proboste, G. Asher, and J. Clare, "Sensorless control of doubly-fed induction generators using a rotor-current-based MRAS observer," *IEEE Transactions on Industrial Electronics*, vol. 55, no. 1, pp. 330–339, 2008.

[77] J. Hu, W. Zhang, H. Wang, and Y. He, "Improved MRAS Observer and Sensorless Control of DFIG during Network Voltage Unbalance," in *2009 IEEE International Electric Machines and Drives Conference, IEMDC '09*, 2009, pp. 1486–1491.

[78] M. Pattnaik and D. Kastha, "Reactive Power based MRAS Observer for Speed Sensorless Control of Double Output Induction Generator," in *2010 5th International Conference on Industrial nad Information Systems*, 2010, pp. 556–561.

[79] G. D. Marques, F. V. Pires, S. Sousa, and D. M. Sousa, "A DFIG Sensorless Rotor-Position Detector Based on a Hysteresis Controller," *IEEE Transactions on Energy Conversion*, vol. 26, no. 1, pp. 9–17, 2011.

[80] M. S. Carmeli, F. Castelli-dezza, M. Iacchetti, and R. Perini, "Effects of Mismatched Parameters in MRAS Sensorless Doubly Fed Induction Machine Drives," *IEEE Transactions on Power Electronics*, vol. 24, no. 11, pp. 2842–2851, 2010.

[81] N. Amiri, S. M. Madani, and H. A. Zarchi, "Direct Decoupled Active and Reactive Power Control of Doubly Fed Induction Machine Without Rotor Position Sensors and with Robustness to Saturation and Parameter Variation," in *2011 IEEE International Electric Machines & Drives Conference (IEMDC)*, 2011, pp. 747–752.

[82] M. Pattnaik and D. Kastha, "Comparison of MRAS based Speed Estimation Methods for a Stand Alone Doubly Fed Induction Generator," in *2011 International Conference on Energy, Automation and Signal*, 2011, pp. 1–6.

[83] M. R. Esmaeeli, R. Kianinejad, and M. Razzaz, "Field Oriented Control of DFIG Based on Modified MRAS Observer," in *2012 Proceedings of 17th Conference on Electrical Power Distribution*, 2012, pp. 1–7.

Stellenbosch University https://scholar.sun.ac.za

[84] N. Amiri, S. M. Madani, T. A. Lipo, and H. A. Zachri, "An Improved Direct Decoupled Power Control of Doubly Fed Induction Machine Without Rotor Position Sensor and With Robustness to Parameter Variation," *IEEE Transactions on Energy Conversion*, vol. 27, no. 4, pp. 873–884, 2012.

[85] N. K. S. Naidu and B. Singh, "Sensorless control of single voltage source converter-based doubly fed induction generator for variable speed wind energy conversion system," *IET Power Electronics*, vol. 7, no. 12, pp. 2996–3006, 2014.

[86] A. Susperregui, J. Jugo, I. Lizarraga, and G. Tapia, "Automated control of doubly fed induction generator integrating sensorless parameter estimation and grid synchronisation," *IET Renewable Power Generation*, vol. 8, no. 1, pp. 76–89, 2014.

[87] B. Touaiti, H. B. Azza, and M. Jemli, "A MRAS Observer for Sensorless Control of Wind-driven Doubly Fed Induction Generator in Remote Areas," in *17th International Conference on Sciences and Techinques of Automatic control & Computing Engineering (STA)*, 2016, pp. 526–531.

[88] S. Yang and V. Ajjarapu, "A Speed-Adaptive Reduced-Order Observer for Sensorless Vector Control of Doubly Fed Induction Turbines, Generator-based Variable-speed Wind," *IEEE Transactions on Energy Conversion*, vol. 25, no. 3, pp. 891–900, 2010.

[89] K. Scicluna, C. Spiteri-staines, and M. Apap, "Analysis of Harmonics on a MRAS system used for Sensorless Control of a DFIG," in *2013 15th European Conference on Power Electronics and Applications (EPE)*, 2013, pp. 1–12.

[90] G. Iwanski, M. Szypulski, T. Luszczyk, and P. Pura, "Cross and dot product based MRAS Observer of the rotor position of doubly-fed induction machine," in *2014 Ninth International Conference on Ecological Vehicules and Renewable Energies (EVER)*, 2014, pp. 1–5.

[91] M. Szypulski and G. Iwanski, "Sensorless State Control of Stand-Alone Doubly Fed Induction Generator Supplying Nonlinear and Unbalanced Loads," *IEEE Transactions on Energy Conversion*, vol. 31, no. 4, pp. 1530–1538, 2016.

[92] U. Shipurkar, D. T. Strous, H. Polinder, J. A. Ferreira, and A. Veltman, "Achieving Sensorless Control for the Brushless Doubly-Fed Induction Machine," *IEEE Transactions on Energy Conversion*, vol. PP, no. 99, pp. 1–1, 2017.

Stellenbosch University https://scholar.sun.ac.za

[93] G. D. Marques and D. M. Sousa, "Air-Gap-Power-Vector-Based Sensorless Method for DFIG Control Without Flux Estimator," *IEEE Transactions Industrial Electronics*, vol. 58, no. 10, pp. 4717–4726, 2011.

[94] M. F. Iacchetti, G. D. Marques, R. Perini, and D. M. Sousa, "Stator Inductance Self-Tuning in an Air-Gap-Power-Vector-Based Observer for the Sensorless Control of Doubly Fed Induction Machines," *IEEE Transactions on Industrial Electronics*, vol. 61, no. 1, pp. 139–148, 2014.

[95] G. D. Marques and D. M. Sousa, "New Sensorless Rotor Position Estimator of a DFIG Based on Torque Calculations - Stability Study," *IEEE Transactions on Energy Conversion*, vol. 27, no. 1, pp. 196–203, 2012.

[96] M. Pattnaik and D. Kastha, "Adaptive speed observer for a stand-alone doubly fed induction generator feeding nonlinear and unbalanced loads," *IEEE Transactions on Energy Conversion*, vol. 27, no. 4, pp. 1018–1026, 2012.

[97] G. D. Marques, J. Santana, and M. F. Iacchetti, "A New Direct Slip-Position Estimator MRAS Self-Sensing Control Method for Application on the DFIG Connected to a DC Network through a Diode Rectifier on the Stator Circuits," in *2014 14th European Conference on Power Electronics and Applications*, 2014, pp. 1–9.

[98] G. D. Marques and M. F. Iacchetti, "Inner Control Method and Frequency Regulation of a DFIG Connected to a DC Link," *IEEE Transactions on Energy Conversion*, vol. 29, no. 2, pp. 435–444, 2014.

[99] A. B. Ataji, Y. Miura, T. Ise, and T. Hiroki, "A Rotor-Current-Based Slip Angle Estimator for Grid-Connected Doubly Fed Induction Generator Requiring the Stator Inductance Only," *IEEE Transactions on Power Electronics*, vol. 32, no. 6, pp. 4827–4838, 2017.

[100] G. Zhang, J. Yang, M. Su, W. Tang, and F. Blaabjerg, "Stator-Current-Based MRAS Observer for the Sensorless Control of the Brushless Doubly-Fed Induction Machine," in *2017 IEEE Applied Power Electronics Conference and Exposition (APEC)*, 2017, pp. 3150–3155.

[101] S. Tohidi, "Analysis and simplified modelling of brushless doubly-fed induction machine in synchronous mode of operation," *IET Electric Power Applications*, vol. 10, no. 2, pp. 110–116, 2016.

[102] E. Maldonado, M. Olivares, and S. Mar, "Sensorless Control of a Doubly Fed Induction Machine Based on an Extended Kalman Filter," in *Proceedings of 2011 14th European Conference on Power Electronics and Appplications*, 2011, pp. 1–10.

Stellenbosch University https://scholar.sun.ac.za

[103] M. Abdelrahem, C. Hackl, and R. Kennel, "Sensorless Control of Doubly-Fed Induction Generators in Variable-Speed Wind Turbine Systems," in *2015 International Conference on Clean Electrical Power (ICCEP)*, 2015, pp. 406–413.

[104] I. Perez Ricardo, J. Cesar Silva, E. Juan Yuz, and R. Gonzalo Carrasco, "Experimental Sensorless Vector Control Performance of a DFIG Based on an Extended Kalman Filter," in *IECON 2012-38th Annual Conference on IEEE Industrial Electronics Society*, no. 1, 2012, pp. 1786–1792.

[105] B. Mwinyiwiwa, Y. Zhang, B. Shen, and B. T. Ooi, "Rotor Position Phase-Locked Loop for Decoupled P - Q Control of DFIG for Wind Power Generation," *IEEE Transactions on Energy Conversion*, vol. 24, no. 3, pp. 758–765, 2009.

[106] B. Shen, B. Mwinyiwiwa, Y. Zhang, and B. T. Ooi, "Sensorless maximum power point tracking of wind by DFIG using rotor position phase lock loop (PLL)," *IEEE Transactions on Power Electronics*, vol. 24, no. 4, pp. 942–951, 2009.

[107] S. Bayhan and H. Abu-Rub, "Performance Comparison of two Sensorless Control Methods for Standalone Doubly-Fed Induction Generator," in *2014 16th International Power Electronics and Motion Control Conference and Exposition*, 2014, pp. 996–1000.

[108] I. Boldea, M. C. Paicu, and G.-d. Andreescu, "Active Flux Concept for Motion-Sensorless Unified AC Drives," *IEEE Transactions on Power Electronics*, vol. 23, no. 5, pp. 2612–2618, 2008.

[109] I. Boldea and S. Agarlita, "The active flux concept for motion-sensorless unified AC drives: a review," in *International Aegean Conference on Electrical Machines and Power Electronics and Electromotion, Joint Conference*, 2011, pp. 1–16.

[110] M. Jafarifar, R. Kianinezhad, S. Seifossadat, and S. Mortazavi, "Sliding mode and disturbance observer: Two viable schemes for sensor-less control of induction machines," in *2009 4th IEEE Conference on Industrial Electronics and Applications*, 2009, pp. 2329–2334.

[111] D. D. Reigosa, F. Briz, C. B. Charro, A. D. Gioia, and J. M. Guerrero, "Sensorless Control of Doubly Fed Induction Generators Based on Rotor High-Frequency Signal Injection," in *2012 IEEE Energy Conversion Congress and Exposition (ECCE)*, 2012, pp. 2268–2275.

[112] D. D. Reigosa, F. Briz, C. B. Charro, A. D. Gioia, P. Garcia, and J. M. Guerrero, "Sensorless Control of Doubly Fed Induction Generators Based on Rotor High-Frequency Signal Injection," *IEEE Transactions on Industry Applications*, vol. 49, no. 6, pp. 2593–2601, 2013.

Stellenbosch University https://scholar.sun.ac.za

[113] L. Xu, E. Inoa, Y. Liu, and B. Guan, "A New High-Frequency Injection Method for Sensorless Control of Doubly Fed Induction Machines," *IEEE Transactions on Industry Applications*, vol. 48, no. 5, pp. 1556–1564, 2012.

[114] K. Tshiloz, D. Vilchis-rodriguez, S. Djukanovic, N. Sarma, and S. Djurović, "Sensorless speed estimation in wound rotor induction machines by spectral search of the stator phase power signal," *IET Electric Power Applications*, vol. 10, no. 6, pp. 581–592, 2016.

[115] F. Castelli-dezza, M. F. Iacchetti, and R. Perini, "An Observer for Sensorless DFIM Drives Based on the Natural Fifth Harmonic of the Line Voltage , Without Stator Current Measurement," *IEEE Transactions on Industrial Electronics*, vol. 60, no. 10, pp. 4301–4309, 2013.

[116] S. Bayhan, S. Demirbas, and H. Abu-rub, "Fuzzy-PI-based sensorless frequency and voltage controller for doubly fed induction generator connected to a DC microgrid," *IET Renewable Power Generation*, vol. 10, no. 8, pp. 1069–1077, 2016.

[117] S. Bayhan, H. Abu-rub, and O. Ellabban, "Sensorless model predictive control scheme of wind-driven doubly fed induction generator in dc microgrid," *IET Renewable Power Generation*, vol. 10, no. 4, pp. 514–521, 2016.

[118] M. Mbukani and N. Gule, "Investigation of the stator voltage-oriented control of the rotor side converter in DFIG systems," in *Southern African Universities Power Engineering Conference (SAUPEC)*, 2017, pp. 108–113.

[119] A. Tapia, G. Tapia, J. Ostolaza, and J. Saenz, "Modeling and control of a wind turbine driven doubly fed induction generator," *IEEE Transactions on Energy Conversion*, vol. 18, no. 2, pp. 194–204, 2003.

[120] M. K. Das, S. P. Chowdhury, M. Ieee, S. Chowdhury, and P. A. Domijan, "Dynamic Modelling and Performance Analysis of a DFIG Wind Energy Conversion System," pp. 1–5, 2008.

[121] F. Liu, Z. Liu, S. Mei, W. Wei, and Y. Yao, "ESO-Based Inertia Emulation and Rotor Speed Recovery Control for DFIGs," vol. 32, no. 3, pp. 1209–1219, 2017.

[122] J. Slootweg, S. de Haan, H. Polinder, and W. Kling, "General model for representing variable speed wind turbines in power system dynamics simulations," *IEEE Transactions on Power Systems*, vol. 18, no. 1, pp. 144–151, 2003.

Stellenbosch University https://scholar.sun.ac.za

[123] V. Blasko and V. Kaura, "new mathematical model and control of a three-phase AC-DC voltage source converter," *IEEE Transaction on Power Electronics*, vol. 12, no. 1, pp. 116–123, 1997.

[124] M. Liserre, F. Blaabjerg, and S. Hansen, "Design and control of an LCL-filter-based three-phase active rectifier," *IEEE Transactions on Industry Applications*, vol. 41, no. 5, pp. 1281–1291, 2005.

[125] M. Mbukani and N. Gule, "Analysis and control of a grid-connected three-phase PWM voltage-source converter based LCL filter," in *Southern African Universities Power Engineering Conference (SAUPEC)*, 2017, pp. 853–858.

[126] V. Kaura and V. Blasko, "Operation of a phase locked loop system under distorted utility conditions," *IEEE Transactions on Industry Applications*, vol. 33, no. 1, pp. 58–63, 1997.

[127] G. Wang, Z. Li, G. Zhang, Y. Yu, and D. Xu, "Quadrature PLL-based high-order sliding-mode observer for IPMSM sensorless control with online MTPA control strategy," *IEEE Transactions on Energy Conversion*, vol. 28, no. 1, pp. 214–224, 2013.

[128] H. C. Skudelny and G. V. Stanke, "Analysis and Realization of a Pulsewidth Modulator Based on Voltage Space Vectors," *IEEE Transactions on Industry Applications*, vol. 24, no. 1, pp. 142–150, 1988.

Stellenbosch University https://scholar.sun.ac.za

Appendices

Stellenbosch University https://scholar.sun.ac.za

Appendix A

Data and Experimental setup

A.1 Experimental setup

In this section further details on the test-bench is presented. In addition, the modelling of the power converters is also presented. Further, the implementation of the space vector pulse width modulation (SVPWM) is presented.

A.1.1 System overview

The (RDFIG) test-bench consists of the 5.5-kW custom-designed RDFIG. A diagrammatic overview of the test-bench is illustrated in Figure A.1. The basis of the test-bench is the National Instruments (NI) PXIe-8115 embedded real-time controller. Two FPGA expansion modules allow the real-time controller to input and output signals. The host computer is used to development the virtual instruments VIs in LabVIEW that will be executed on the PXIe controller.

A.1.2 IO interface modules

The voltages that can be measured by the NI FPGA modules ranges from -10 V to +10 V. However, the voltage level of signals to be measured by the system may either be too high (in the case of the grid voltage measurement) or too small to be accurately measurement (such as the strain gauge measurement). Thus, interface modules were developed to condition the input signals for data acquisition. Each module performs a specific task and is housed within a generic project box.

A.1.3 FPGA Breakout Box

Each NI 7841R FPGA module installed within the NI PXIe-1071 chassis has three separate connectors. These connectors provide connections to the IO pins of the FPGA. Breakout boxes are required to gain easier access to these FPGA

Stellenbosch University https://scholar.sun.ac.za

IO pins. Only one box per FPGA module is used. Each FPGA module provides access to eight analogue inputs, eight analogue outputs, digital IO, power, and ground. In order to provide quick and easy connection/disconnection of the modules to/from the breakout box, a circuit board with RJ45 sockets was designed to the breakout box. Wires connect the terminal blocks on the RJ45 expansion board to the terminal blocks of the NI FPGA breakout box.

A.2 Data of the RDFIG

The experiments were made on a RDFIG system that is located in the Electrical machine laboratory at Stellenbosch University. The data of the RDFIG is depicted in Table A.1 and Table A.2.

Table A.1: Nominal values of the RDFIG

Rated power P_n	5.5 kW
Rated rotor voltage (Δ) V_s	346.3 V_{LL}
Rated stator voltage (Δ) V_r	380 V_{LL}
Rated stator current I_s	5.65 A
Rated stator current I_r	6.3 A
Rated frequency f_n	50 Hz
Inertia J	0.0003215 Kgm^2

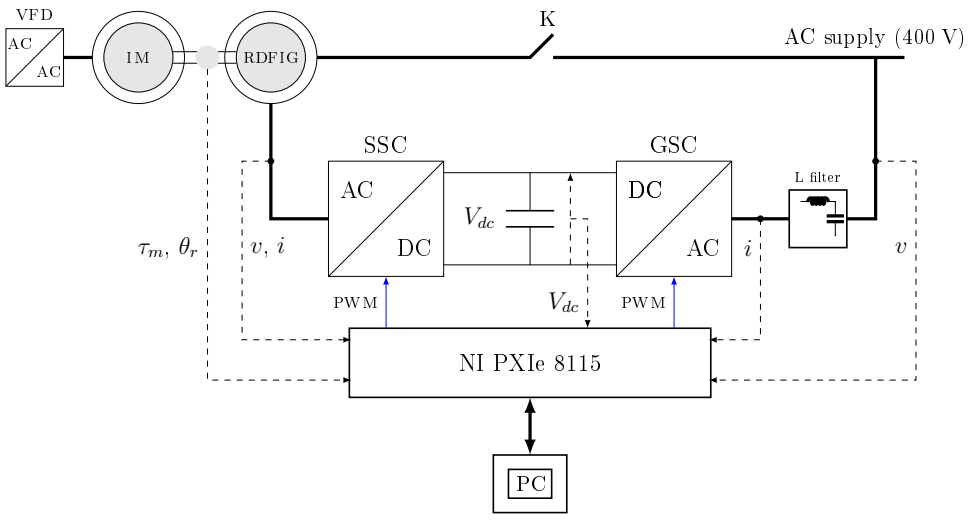

Figure A.1: Laboratory setup.

Stellenbosch University https://scholar.sun.ac.za

Table A.2: Nominal values of the RDFIG

Rated power P_n	5.5 kW
Stator resistance R_s	2.1 Ω
Rotor resistance R_r	1.85 Ω
Rated stator current L_{sl}	0.0188 H
Rated rotor current L_{rl}	0.0188 H
Magnetising inductance L_m	0.257 H

A.3 Commercially-modified SEW power converter

The data of the commercially-modified SEW power converter are presented in Table A.3 and Table A.4.

Table A.3: Nominal inputs of the SEW power converter

Rated voltage (Δ) (U_s)	3×380 V...3×500 V
Rated frequency f_n	50...60 Hz
Rated current I	11.3 A (400V AC)

Table A.4: Nominal outputs of the SEW power converter

Rated voltage (Δ) (U_s)	3×380 V...3×500
Rated frequency f_n	0...180 Hz
Rated current I	12.5 A (400 V AC)
Rated apparent power S	8.7 kVA

A.4 Data of the L filter

The parameters of the L filter are presented in Table A.5. A illustration of the L filter is shown in Figure A.2.

Table A.5: Nominal outputs of the SEW power converter

Rated voltage (Δ) (U_s)	3×380 V...3×500
Rated frequency f_n	0...180 Hz
Rated current I	12.5 A (400 V AC)
Rated apparent power S	8.7 kVA

Stellenbosch University https://scholar.sun.ac.za

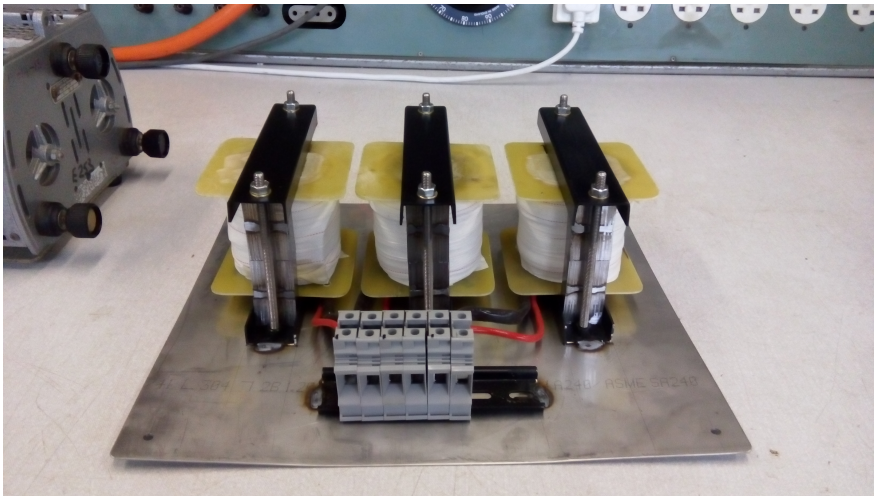

Figure A.2: Built Filter

A.5 Back-to-back power converter model

It is assumed that the back-to-back converters of the RDFIG system consists of two three-phase two-level voltage-source converters (VSCs). A VSC circuit is shown in Figure A.3. The SSC and GSC accounts for six power switches each. Hence, for each phase or leg, there are two power switches. From a switching point of view, it is important that the switching of power switches that belong to the same phase or leg should be complementary to avoid short-circuiting the DC-link. Hence, when the lower power switch is closed (ON or 1), the upper power switch should be open (OFF or 0).

From Figure A.3, the instantaneous three-phase leg voltage are given by

$$\begin{bmatrix} v_{ca} \\ v_{cb} \\ v_{cc} \end{bmatrix} = \begin{bmatrix} v_{na} \\ v_{nb} \\ v_{nc} \end{bmatrix} + \begin{bmatrix} v_{nN} \\ v_{nN} \\ v_{nN} \end{bmatrix} \tag{A.1}$$

where v_{ca}, v_{cb} and v_{cc} are the instantaneous phase A leg voltage, the instantaneous phase B leg voltage and the instantaneous phase C leg voltage, re-

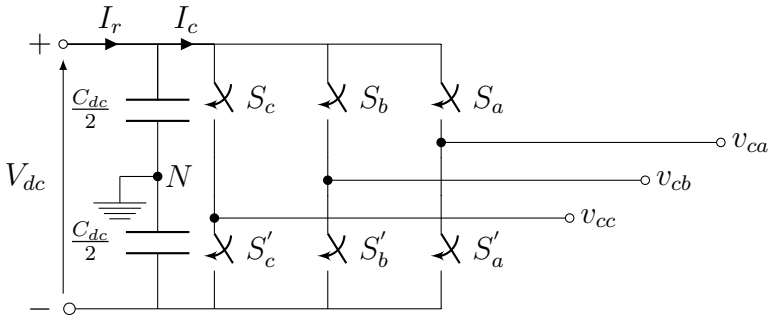

Figure A.3: Power circuit of a VSC

Stellenbosch University https://scholar.sun.ac.za

spectively; v_{na}, v_{nb} and v_{nc} are the instantaneous phase A to neutral voltage, the instantaneous phase B to neutral voltage and the instantaneous phase C to neutral voltage, respectively; and v_{nN} is the instantaneous common mode voltage.

Assume that the VSC is connected to a symmetrical three-phase resistive load yields

$$v_{na} + v_{nb} + v_{nc} = 0. \tag{A.2}$$

The sum of the expressions of v_{ca} and v_{cb} and v_{cc} depicted in (A.1) yields that the voltage between the negative point of the DC-link bus and the neutral is given by

$$v_{nN} = \frac{1}{3}(v_{ca} + v_{cb} + v_{cc}). \tag{A.3}$$

Substituting (A.3) into (A.1), the instantaneous line-to-neutral voltage are given by

$$\begin{bmatrix} v_{na} \\ v_{nb} \\ v_{nc} \end{bmatrix} = \begin{bmatrix} \frac{2}{3} & -\frac{1}{3} & -\frac{1}{3} \\ -\frac{1}{3} & \frac{2}{3} & -\frac{1}{3} \\ -\frac{1}{3} & -\frac{1}{3} & \frac{2}{3} \end{bmatrix} \begin{bmatrix} v_{ca} \\ v_{cb} \\ v_{cc} \end{bmatrix} \tag{A.4}$$

Based on the switching function, the three-phase leg voltages are given by

$$\begin{bmatrix} v_{ca} \\ v_{cb} \\ v_{cc} \end{bmatrix} = \frac{V_{dc}}{2} \begin{bmatrix} 1 & 0 & 0 \\ 0 & 1 & 0 \\ 0 & 0 & 1 \end{bmatrix} \begin{bmatrix} S_a \\ S_b \\ S_c \end{bmatrix}, \tag{A.5}$$

where S_a, S_b, S_c are the switching function of the upper power switches of the phase A, phase B and phase C legs, respectively. The switching functions have two state. There are the ON state with $S_a = 1$ and OFF state, with $S_a = 0$.

Substituting (A.5) into (A.4), and based on the switching state, the instantaneous three-phase converter voltage are presented in Table A.6. It can also be seen that the two-level three-phase voltage source converter accounts for height switching state. In Table A.6, K denotes the switching state of the power switches. Further, the maximum amplitude value of the three-phase line-to-neutral voltage is $\frac{2V_{dc}}{3}$.

Table A.6: Switching states

Switching states	S_a	S_b	S_c	v_{na}	v_{nb}	v_{nc}	v_{ab}	v_{bc}	v_{ca}
K_0	0	0	0	0	0	0	0	0	0
K_1	1	0	0	$\frac{2V_{dc}}{3}$	$\frac{-V_{dc}}{3}$	$\frac{-V_{dc}}{3}$	V_{dc}	0	$-V_{dc}$
K_2	1	1	0	$\frac{V_{dc}}{3}$	$\frac{V_{dc}}{3}$	$\frac{-2V_{dc}}{3}$	0	V_{dc}	$-V_{dc}$
K_3	0	1	0	$\frac{-V_{dc}}{3}$	$\frac{2V_{dc}}{3}$	$\frac{-V_{dc}}{3}$	$-V_{dc}$	$-V_{dc}$	0
K_4	0	1	1	$\frac{-2V_{dc}}{3}$	$\frac{V_{dc}}{3}$	$\frac{V_{dc}}{3}$	$-V_{dc}$	0	V_{dc}
K_5	0	0	1	$\frac{-V_{dc}}{3}$	$\frac{-V_{dc}}{3}$	$\frac{2V_{dc}}{3}$	0	$-V_{dc}$	V_{dc}
K_6	1	0	1	$\frac{V_{dc}}{3}$	$\frac{-2V_{dc}}{3}$	$\frac{V_{dc}}{3}$	V_{dc}	$-V_{dc}$	0
K_7	1	1	1	0	0	0	0	0	0

Stellenbosch University https://scholar.sun.ac.za

A.5.1 Space vector representation of the switching states

The converter voltage space vector is given by

$$\vec{v}_c = \frac{2}{3}\left(v_{na}e^{j0} + v_{nb}(t)e^{\left(j\frac{2\pi}{3}\right)} + v_{nc}(t)e^{\left(j\frac{4\pi}{3}\right)}\right) = v_{c\alpha} + jv_{c\beta}. \tag{A.6}$$

From (A.6), the α-axis and β-axis converter voltages are given by

$$v_{c\alpha} = \frac{2}{3}\left(v_{na} + v_{nb}\cos\left(\frac{2\pi}{3}\right) + v_{nc}\cos\left(\frac{2\pi}{3}\right)\right) \tag{A.7}$$

and

$$v_{c\beta} = \frac{2}{3}\left(v_{nb}\sin\left(\frac{2\pi}{3}\right) - v_{nc}\sin\left(\frac{2\pi}{3}\right)\right). \tag{A.8}$$

Based on (A.6), the predefined values of the converter voltage with regards to the switching states are presented in Table A.7. It can be seen that converter voltage space vector follows a certain pattern with regards to the switching states. For the switching states different to all ON or all OFF, the converter voltage space vector has the same magnitude rotating at a rate of sixty degree. This pattern is very useful for the implementation of the space vector width pulse width modulation (SV-PWM). The SV-PWM function is discussed in Appendix A.6.

Table A.7: predefined converter voltage space vectors based on the switching states

Space vector	Switching state	Space vector value
$\vec{v}_0$	[000]	$\vec{v}_0 = 0$
$\vec{v}_1$	[100]	$\vec{v}_1 = \frac{2}{3}V_{dc}e^{j0}$
$\vec{v}_2$	[110]	$\vec{v}_2 = \frac{2}{3}V_{dc}e^{j\frac{\pi}{3}}$
$\vec{v}_3$	[010]	$\vec{v}_3 = \frac{2}{3}V_{dc}e^{j\frac{2\pi}{3}}$
$\vec{v}_4$	[011]	$\vec{v}_4 = \frac{2}{3}V_{dc}e^{j\frac{3\pi}{3}}$
$\vec{v}_5$	[001]	$\vec{v}_5 = \frac{2}{3}V_{dc}e^{j\frac{4\pi}{3}}$
$\vec{v}_6$	[101]	$\vec{v}_6 = \frac{2}{3}V_{dc}e^{j\frac{5\pi}{3}}$
$\vec{v}_7$	[111]	$\vec{v}_7 = \frac{2}{3}V_{dc}e^{j0}$

A.6 Continuous space vector modulation implementation

It was shown in Appendix A.5, that the three-phase two-level VSC offers eight switching states. There are six active switching states and two non-active

Stellenbosch University https://scholar.sun.ac.za

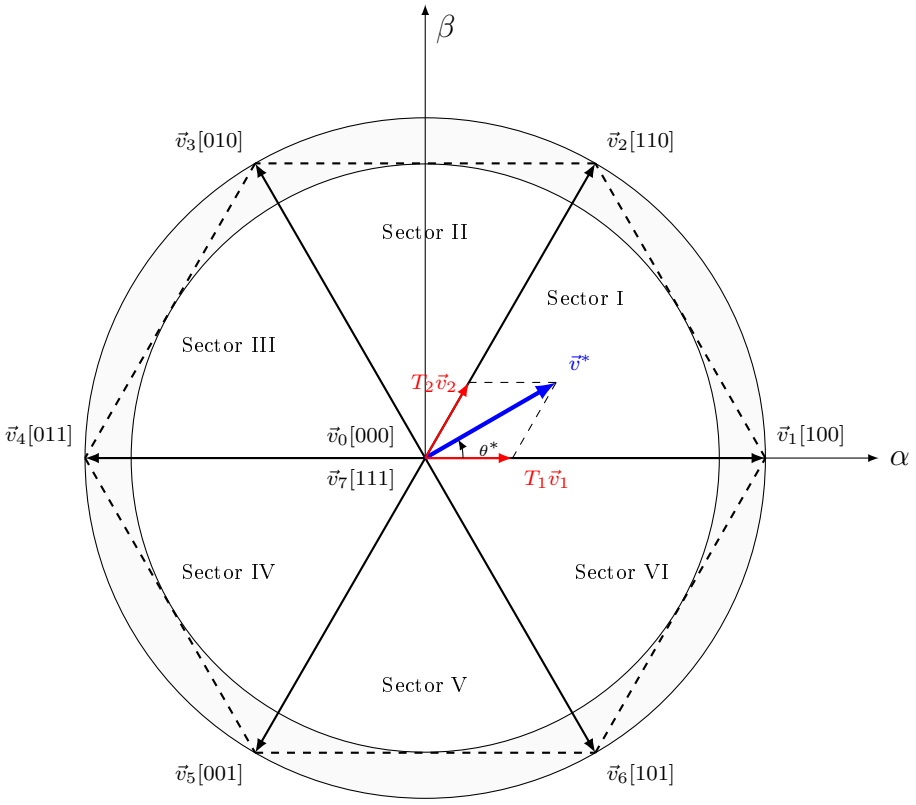

Figure A.4: Space vector schemes for SVPWM.

switching states. The values of the converter voltage space vector with regards to the active switching states form an hexagon, as shown in Figure A.4. The hexagon accounts for six sectors. Each sector in the hexagon accounts for sixty degrees. The linear region is located in the circle inside the hexagon, as shown in Figure A.4.

The space vector pulse width modulation (SV-PWM) function aims at mapping at each instant the reference stator/converter voltage space vector onto the hexagonal plan in order to produce the related switching sequence, as presented in Figure A.4. It is important to note that the non-active voltage space vectors are located at the origin. In Figure A.4, $\vec{v}_0$, $\vec{v}_1$, $\vec{v}_2$, $\vec{v}_3$, $\vec{v}_4$, $\vec{v}_5$, $\vec{v}_6$ and $\vec{v}_7$ are the adjacent space vectors that relate to the switching states, as depicted in Table A.8. Depending on the sector in which the reference stator/converter voltage space vector is in at each sampling time, it is approximated by the combination of the adjacent space vectors (active and non-active space vectors).

In Figure A.4, the radius of the circle inside the hexagon is given by

$$|\vec{v}^*| = \frac{2}{3} V_{dc} \cos\left(\frac{\pi}{3}\right), \tag{A.9}$$

where $|\vec{v}^*|$ is the maximum magnitude of the reference voltage space vector

Stellenbosch University https://scholar.sun.ac.za

Table A.8: Swiching segments according to each sector.

Sectors	Switching segments						
I	$\vec{v}_0$,[000]	$\vec{v}_1$,[100]	$\vec{v}_2$,[110]	$\vec{v}_7$,[111]	$\vec{v}_2$,[110]	$\vec{v}_1$,[100]	$\vec{v}_0$,[000]
II	$\vec{v}_0$,[000]	$\vec{v}_3$,[010]	$\vec{v}_2$,[110]	$\vec{v}_7$,[111]	$\vec{v}_2$,[110]	$\vec{v}_3$,[010]	$\vec{v}_0$,[000]
III	$\vec{v}_0$,[000]	$\vec{v}_3$,[010]	$\vec{v}_4$,[011]	$\vec{v}_7$,[111]	$\vec{v}_4$,[011]	$\vec{v}_3$,[010]	$\vec{v}_0$,[000]
IV	$\vec{v}_0$,[000]	$\vec{v}_5$,[001]	$\vec{v}_4$,[011]	$\vec{v}_7$,[111]	$\vec{v}_4$,[011]	$\vec{v}_5$,[001]	$\vec{v}_0$,[000]
V	$\vec{v}_0$,[000]	$\vec{v}_5$,[001]	$\vec{v}_6$,[101]	$\vec{v}_7$,[111]	$\vec{v}_6$,[101]	$\vec{v}_5$,[001]	$\vec{v}_0$,[000]
VI	$\vec{v}_0$,[000]	$\vec{v}_1$,[100]	$\vec{v}_6$,[101]	$\vec{v}_7$,[111]	$\vec{v}_6$,[101]	$\vec{v}_1$,[100]	$\vec{v}_0$,[000]

beyond which the reference space vector cannot be properly approximated. Hence, it is important to limit the reference stator/converter voltage space vector (which is the output of the inner current control loops) in order to avoid operating in the over-modulation region. The SV-PWM function in the over-modulation region is not discussed in this thesis. The modulation index is used in order to define the region in which the reference stator/converter voltage space vector is located. The modulation index is the ratio of the maximum magnitude of the reference voltage space vector over the the fundamental of the voltage square wave. The modulation index is given by

$$m = \frac{\frac{2}{3}V_{dc}\cos(\frac{\pi}{6})}{\frac{2V_{dc}}{\pi}} = 0.904, \tag{A.10}$$

where m is the modulation index.

The binary sequence in Figure A.4 represents the switching patterns of the three-phase two-level VSC.

Assume that $\vec{v}^*$ is constant during the switching period (T_{sw}). When the reference stator/converter voltage space vector ($\vec{v}^*$) is situated within the sector I, it can be approximated using the adjacent space vectors that form the sector I with a specific duration. Hence, the reference stator/converter voltage space vector is approximated by the sum of $\vec{v}_1$ applied for a time period of T_1, $\vec{v}_2$ applied for a time period of the T_1 and both $\vec{v}_7 = 0$ and $\vec{v}_0 = 0$ applied for the time period T_0. Hence, during the switching period, the reference voltage space vector is then given by

$$T_1\vec{v}_1 + T_2\vec{v}_2 = T_{sw}\vec{v}^* \tag{A.11}$$

with

$$T_{sw} = T_1 + T_2 + T_0. \tag{A.12}$$

Rewriting (A.11) in terms of real and imaginary components yields,

$$T_1|\vec{v}_1| + d_2|\vec{v}_2|\cos(\frac{\pi}{3}) = T_{sw}|\vec{v}^*|\cos(\theta^*) \tag{A.13}$$

and

$$T_2|\vec{v}_2|\sin(\frac{\pi}{3}) = T_{sw}|\vec{v}^*|\sin(\theta^*). \tag{A.14}$$

Stellenbosch University https://scholar.sun.ac.za

By solving (A.13) and (A.14) as a system of equations with the time periods as unknown variables yields,

$$T_1 = T_{sw}\frac{|\vec{v}^*|}{|\vec{v}_1|}\frac{\sin(\theta^* - \frac{\pi}{3})}{\sin(\frac{\pi}{3})} \tag{A.15}$$

and

$$T_2 = T_{sw}\frac{|\vec{v}^*|}{|\vec{v}_2|}\frac{\sin(\theta^*)}{\sin(\frac{\pi}{3})}. \tag{A.16}$$

A similar approach is followed in order to calculate the time period when the reference stator/converter voltage is in the Sectors II to VI. The time periods at any sector can be generalised by

$$\begin{bmatrix} T_k \\ T_{k+1} \end{bmatrix} = \frac{\sqrt{3}T_{sw}}{2V_{dc}} \begin{bmatrix} \sin\frac{k\pi}{3} & -\cos\frac{k\pi}{3} \\ -\sin\frac{(k-1)\pi}{3} & \cos\frac{(k-1)\pi}{3} \end{bmatrix} \begin{bmatrix} v_\alpha \\ v_\beta \end{bmatrix}, \tag{A.17}$$

where k=1,2,...,6. The time period for the application of non-active vectors is given by

$$T_0 = T_{sw} - (T_k - T_{k+1}). \tag{A.18}$$

The symmetrical sequence of the SV-PWM signals allows for the reduction of the harmonics, as discussed in [128]. In this thesis the The symmetrical sequence of the SV-PWM signals is adopted. The symmetrical sequence of the SV-PWM allows for only one leg to change state at a time. The symmetrical

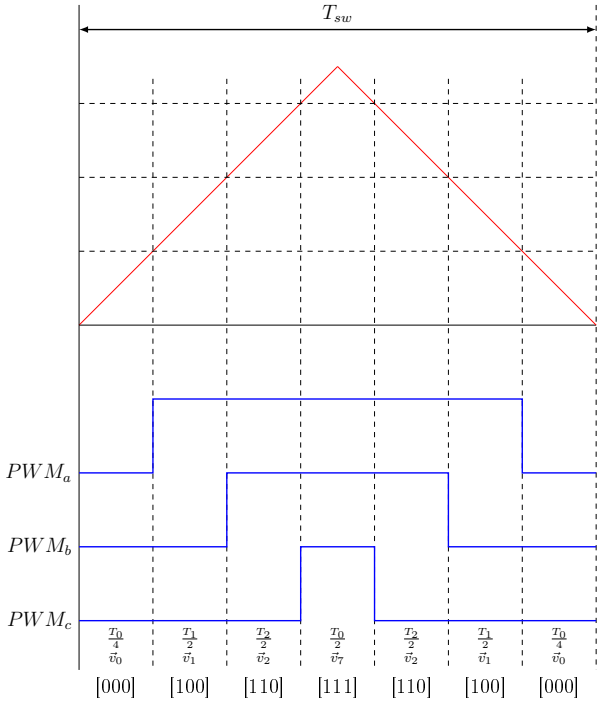

Figure A.5: Symmetrical SVPWM waveforms.

Stellenbosch University https://scholar.sun.ac.za

sequence consists of starting with a non-active vector, then switching one bit amongst the voltage space vectors with regard to the sector in which the reference voltage space vector is located in. A similar approach can be used for other sectors. The symmetrical SVPWM scheme for sector I is displayed in Figure A.5.